論文 / 著書情報
Article / Book Information

題目(和文)	
Title(English)	A Study of MHD Electrical Power Generation Using Xenon-Seeded Noble Gas Plasma
著者(和文)	ORK KIMSOR
Author(English)	Kimsor Ork
出典(和文)	学位:博士(工学), 学位授与機関:東京工業大学, 報告番号:甲第12760号, 授与年月日:2024年3月26日, 学位の種別:課程博士, 審査員:奥野 喜裕,岡村 哲至,平井 秀一郎,末包 哲也,笹部 崇
Citation(English)	Degree:Doctor (Engineering), Conferring organization: Tokyo Institute of Technology, Report number:甲第12760号, Conferred date:2024/3/26, Degree Type:Course doctor, Examiner:,,,,
学位種別(和文)	博士論文
Type(English)	Doctoral Thesis

A Study of MHD Electrical Power Generation Using Xenon-Seeded Noble Gas Plasma

A Dissertation

Submitted to the School of Engineering
of Tokyo Institute of Technology
in Partial Fulfillment of the Requirements
for the Degree of

Doctor of Engineering

By

ORK KIMSOR

Supervisor: **Professor Yoshihiro Okuno**

Energy Science and Engineering
Department of Mechanical Engineering
School of Engineering
Tokyo Institute of Technology
December 2023

This dissertation is dedicated to my mother, ***LEAN SAILENG*** *(1959~2020),*
who passed away while I was studying Master's degree in Japan,
a period during which the COVID-19 infection spread worldwide.

សូមឧទ្ទិសនិក្ខេបបទថ្នាក់បណ្ឌិតមួយនេះជូនដល់ម្តាយរបស់ខ្ញុំ ***លាន សៃឡេង*** *(១៩៥៩~២០២០)*
ដែលបានទទួលមរណភាពក្នុងអំឡុងពេលដែលខ្ញុំកំពុងសិក្សាថ្នាក់អនុបណ្ឌិតនៅប្រទេសជប៉ុន
ចំពេលដែលមេរោគកូវីដ១៩កំពុងតែរីករាលដាលយ៉ាងខ្លាំងនៅទូទាំងពិភពលោក។

Contents

Nomenclature

Roman

$A,\ A_{in}$	= cross-sectional area, cross-sectional area at generator inlet [m^2]
$\vec{B}$	= magnetic flux density vector [T]
B_z	= magnetic flux density in z-direction [T]
C_f	= local skin friction coefficient [–]
c_e	= mean thermal velocity of electron [m/s]
c_p	= specific heat at constant pressure [J/(kg·K)]
c_v	= specific heat at constant volume [J/(kg·K)]
dt	= time step [s]
$\vec{E}$	= electric field vector [V/m]
E_r, E_θ, E_z	= electric field strength in r-, θ-, z-direction [V/m]
E_s	= total energy density [J/m^3]
$E.E.R.$	= enthalpy extraction ratio [%]
e	= elementary charge [C], $e = 1.602176634$ C
f_r	= recovery factor [–]
g_i, g_i^+	= Atom ground level degeneracy, ion ground level degeneracy [–]
$\vec{H}$	= magnetic field vector [A/m]
$\hbar$	= Planck constant [J·s]
h_z	= height of the generator channel [m]
I_{out}	= output current [A]
$\vec{j}$	= current density vector [A/m^2]
j_r	= radial (r-direction) current density (Hall current) [A/m^2]
j_θ	= azimuthal (θ-direction) current density (Faraday current) [A/m^2]
j_z	= current density in z-direction [A/m^2]
K_h	= loading parameter [–]
k_B	= Boltzmann constant [J/K]
k_{cu}	= cumulative ionization coefficient [m^3/s]
k_{dex}	= de-excitation coefficient [m^3/s]
k_{ex}	= excitation coefficient [m^3/s]
k_f	= direct ionization coefficient [m^3/s]
k_{pen}	= Penning ionization coefficient [m^3/s]
k_r	= three-body recombination coefficient [m^6/s]
k_{rcu}	= reverse reaction coefficient of cumulative ionization [m^3/s]

M, M_{in} = Mach number, Mach number at generator inlet [–]
m = particle weight [kg]
$m_w, m_{w,\mathrm{M}}, m_{w,\mathrm{S}}$ = molar mass, molar mass of mother gas, molar mass of seed [kg/mol]
n = particle number density [1/m^3]
n_i = number density of particle i [1/m^3]
n_i^+ = ion number density [1/m^3]
n_n = neutral particle number density [1/m^3]
P_e = electrical power output density [W/m^3]
$\vec{P}_{LOSS}$ = pressure loss due to the wall friction [Pa/m]
P_{out} = output power [W]
Pr = Prandtl number [–]
$P.P.$ = pre-ionization power [W]
$P.P.R.$ = pre-ionization power ratio [%]
p, p_e = static gas pressure, electron pressure [Pa]
$p_0, p_{0,in}, p_{0,out}$ = total (stagnation) gas pressure, total gas pressure at generator inlet, total gas pressure at generator outlet [Pa]
Q_{en}, Q_{ei}, Q_{eh} = average momentum transfer cross section of an electron with a neutral atom, an electron with an ion, and an electron with a heavy particle [m^2]
$Q_{in}, Q_{in-e}, Q_{in-h}$ = (total) thermal input, thermal input of electron, thermal input of heavy particle [W]
Q_{LOSS} = heat loss through the wall [W/m^3]
$\vec{q}$ = heat flux vector [W/m^2]
$\vec{q}_g, \vec{q}_e$ = heat flux vector of gas, heat flux vector of electron [W/m^2]
R_c = universal gas constant [J/(K·mol)]
Re_h = Reynold number [–]
R_L = external load resistance [Ω]
R_m = magnetic Reynold number [–]
R_s = gas constant [J/(K·kg)]
$R.P.R.$ = RF input power ratio [%]
r = radius [m]
S = Sutherland constant [K]
S_p = interaction parameter [–]
S_t = Stanton number [–]
T_g, T_e = static gas temperature, electron temperature [K]
$T_0, T_{0,in}, T_{0,out}$ = total gas temperature, total gas temperature at inlet, total gas temperature at outlet [K]

T_{e-in} = electron temperature at generator inlet [K]
T_s = reference (standard) temperature [K]
T_{aw}, T_w = adiabatic wall temperature, wall temperature [K]
t = time [s]
U_e = electron energy density [J/m^3]
$\vec{u}$ = gas velocity vector [m/s]
u_x, u_y = gas velocity in x- and y-direction [m/s]
u_r, u_θ, u_z = gas velocity in r-, θ-, and z-direction [m/s]
V_{out} = output voltage [V]

Greek

α, α_{in} = ionization degree, ionization degree at generator inlet [–]
β = Hall parameter [rad]
β_{crit} = critical Hall parameter [rad]
γ = specific heat ratio [–]
δ = Kronecker delta [–]
ϵ_0 = permittivity of free space [–]
ϵ_i = ionization or excitation energy of particle *i* [eV]
η_e = electrical efficiency [%]
κ_g, κ_e = thermal conductivity of gas, thermal conductivity of electron [W/(m·K)]
μ = shear viscosity [Pa·s]
μ_m, μ_t = molecular viscosity, eddy viscosity [Pa·s]
μ_0 = permeability of vacuum [N/A^2]
ν_e = collision frequency of electron [Hz]
$\nu_{eh}, \nu_{en}, \nu_{ei}$ = collision frequency of electron with heavy particle *h*, with neutral atom, and with ion [Hz]
ρ = mass density [kg/m^3]
ρ_g, ρ_e = mass density of gas, mass density of electron [kg/m^3]
ρ = electrical conductivity [S/m]
$\boldsymbol{\tau}$ = stress tensor [N/m^2]
ϕ = electric potential [V]
ω = vorticity [s^{-1}]

Subscript

aw	= adiabatic wall
e	= electron
g	= heavy particle
h	= heavy particle species
in	= at generator inlet
out	= at generator outlet
r, θ, z	= r, θ, and z components of vector
x, y	= x, y component of vector
w	= at the wall

Chapter 1 Introduction

1.1 Background

Fossil fuels such as oil, coal, and natural gas have been used widely as the world's main energy sources today. The world energy consumption continues to increase due to population increase and economic growth, and it is predicted that oil and nature gas will run out if we continue to use these fossil fuels at the current rate. The Energy Information Administration (EIA) of the United States has reported that the global primary energy consumption in 2050 will increase to about 50% compared with that in 2018 [1]. However, the use of fossil fuels, which account for most of our energy supply, has increased Carbon Dioxide (CO_2) in the atmosphere, causing the global atmospheric to rise due to the so-called greenhouse effect, which deteriorates the global environment. In order to prevent global warming, in recent years each country around the world has begun to reduce the use of energy that relies on fossil fuels, and shift to utilize renewable energies such as hydropower, wind power, solar/thermal energy, and geothermal energy. However, because the output of these renewable energies fluctuates greatly over time during power generation, it is difficult to incorporate them into current power systems on a large scale.

From the above background, to solve global environmental and energy problems, development of technology for effectively utilizing fossil fuels is indeed important in addition to spreading and expanding the use of renewable energy. In order to effectively utilize fossil fuels, it is essential to construct a highly efficient energy conversion system. The magnetohydrodynamic (MHD) electrical power generation described in the present study is expected to be a highly efficient energy conversion technology.

1.2 Researches on MHD electrical power generation

1.2.1 Basic concept of MHD power generation

Magnetohydrodynamic (MHD) electrical power generation directly converts the enthalpy of a high-temperature conductive working gas (e.g., plasma) into electrical energy in accordance with Faraday's law of induction. Conceptually, the motion of conductive working fluid through a magnetic field gives rise to an electromotive force and a flow of current in accordance with Faraday's law of induction, and this current is collected via the electrodes (also see Fig. 1.1). Unlike conventional rotating generators, an MHD power generator can operate without mechanical moving parts, i.e., they do not possess a turbine. Consequently, an MHD

power generator has the potential to utilize working gases with higher temperatures (above 2000 K) than can be used in gas turbine systems, which in turn allows power plants to achieve a high thermal efficiency [2]. This would lead to reduced consumption of fossil fuels and remarkedly reduced thermal pollution. Moreover, the generator itself has a quick response for output control, owing to its reduced mechanical inertia. The idea of MHD power generation existed for many decades, but the principles on which it is based were first introduced by Michael Faraday in 19th century. The first practical MHD power generation experiment was carried out by Bela Karlovitz in the 1940s [3], and in the decades since, especially in the 1960s and 1970s, MHD power generation has been extensively developed as a topping cycle to existing power plants, in an attempt to improve the efficiency of utilizing of fossil fuels such as coal and oil [4], [5]. MHD power generation systems generally fall into one of two types depending on whether they use a combustion or a noble gas as the working gas: an open-cycle MHD (OC-MHD) power generation system and a closed-cycle MHD (CC-MHD) power generation system [2], [6], [7].

In an OC-MHD system, a product from the combustion of fossil fuels at a temperature of approximately 3000 K is used as the working gas. The working gas emitted from MHD generator is eventually released into the atmosphere after passing through the air pre-heater or boiler of a steam turbine. **In a CC-MHD system**, on the other hand, a noble gas is used as the working gas. The noble working gas is heated via a heat exchanger to about 2000–2400 K and is continuously circulated through other system components such as an MHD generator, a recuperator or heat recovery steam generator, and a compressor, constituting a closed-cycle MHD power generation system. Over several decades, many countries and organizations have been involved in researching both types of MHD power generation systems. Recently, research and development of MHD power generators has expanded beyond ground-based applications to include space-based ones as well. In the United States, research and development of MHD generators are being undertaken for the application of a combined cycle in fossil fuel power plants to improve the total plants efficiency [8], whereas in Europe, research and development has focused on the use of MHD generators as high-power energy systems for deep space exploration [9]. For the application in a spacecraft, a radioisotope [9], nuclear fission energy [10], or solar thermal energy [11] can be utilized as a heat source to provide energy to the heat exchanger to heat the working gas. As an application for the deep-space exploration, for instance mission to the Mars, the radioisotope and nuclear fission heat sources are maybe favorable, whereas the solar thermal energy can be difficult to use because the solar energy reduces specifically as inversely proportional to square of the distance from the sun. The working gas exhausted from the MHD generator passes through a heat recuperator (heat exchanger) and then is cooled by a spacecraft thermal radiator.

1.2.2 MHD power generation using working gas seeded with alkali metal

The output power density of an MHD generator is proportional to the electrical conductivity σ of the working gas, the square of the flow velocity u, and the square of the magnetic flux density B, namely $P_{out} \propto \sigma u^2 B^2$. Among these key parameters, enhancement of electrical conductivity is a major concern, whereas magnetic flux density of up to 8 T and the flow velocity on order of 1000 m/s can be achieved. To enhance the electrical conductivity, conventionally a small amount of an easily ionizable seed material, for instance alkali metal (Cs, K) or salt of alkali metal (e.g., K_2CO_3) is usually added to the working gas. This is referred to as an **alkali metal seeded plasma**. In the OC-MHD generator, potassium carbonate (K_2CO_3) is typically selected as the seed material for adding to the combustion gas. The presence of K_2CO_3 in the combustion gas at approximately 3000 K produces a thermal equilibrium plasma, where the electron temperature is similar to the gas (heavy particles) temperature ($T_e \approx T_g$), with electrical conductivity of several or tens S/m. In the CC-MHD generator, cesium (Cs) or potassium (K) is usually selected as the seed material for injecting into the heated noble gas (helium (He) or argon (Ar)). A non-thermal plasma is produced in which the electrons are heated over the heavy particles ($T_e > T_g$) by a so-called self-induced Joule heating due to the electromotive force in the MHD generator. Thus, the electron temperature increases to around 5000 K, which can provide high electrical conductivity on the order of hundreds S/m, an order of magnitude higher than that in combustion plasma. Using a cesium-seeded helium working gas, a high performance of CC-MHD power generator with an enthalpy extraction ratio (the ratio of the power output to the thermal input of the generator) of 31% and an isotropic efficiency (adiabatic efficiency) of 63%, has been demonstrated experimentally in a shock-tube facility [12]. It has been shown that the total efficiency of the CC-MHD power generation system could reach above 60% if the MHD generator has an enthalpy extraction ratio of about 30% and an isentropic efficiency of about 80% or more [2], [13].

The use of alkali metals is indeed essential for providing plasma with adequate electrical conductivity. For the CC-MHD system, however, the alkali metal seed material must be removed from the working gas before it enters the compressor, and reused continuously in the CC-MHD system. Moreover, the seed mole fraction in the working gas needs to be controlled precisely in time and space within the MHD generator channel. These requirements make the system complicated. To avoid complexity arising from seed handling, several methods have been proposed that do not involve the use of an alkali metal.

1.2.3 MHD power generation using working gas without seeding alkali metal

As stated above, to avoid some problems arising from alkali meta seed handling, several methods that do not use alkali metals have been proposed.

Noble gases at an extremely high temperature may have an adequate electrical conductivity for power generation owing to thermal equilibrium ionization [14]–[16]. This is referred to as a **high-temperature noble gas plasma**. In the high-temperature noble gas plasma, the pure noble gas is heated to an extremely high temperature, for instance above 6000 K for Xe or 8000 K for Ar, until the noble gas itself ionizes, becoming a thermal equilibrium plasma. In this method, a maximum enthalpy extraction ratio of about 16% [15] has been demonstrated in a shock-tube facility using a dish-shaped Hall type generator, and an enthalpy extraction ratio of about 13% [16] using a Linear-shaped Faraday type generator. However, such a high-temperature gas is not suitable for continuous operation. Thus, the working gas needs to be pre-ionized at the generator inlet to achieve a high electrical conductivity without seeding alkali metal, provided that the working gas temperature is in the range suitable for continuous operation with an ordinary heat source (2200–2400 K) [17]–[19]. This is referred to as a **seed-free pre-ionized noble gas plasma**.

The concept of the seed-free pre-ionized noble gas plasma is based on the fact that the three-body recombination of noble gas ions is relatively slow at electron temperatures above 5000 K. Therefore, if the noble gas plasma with adequate electrical conductivity is forcibly produced at the generator inlet and if the electron temperature of the plasma is kept at around 5000 K in the generator channel, then the pre-ionized noble gas plasma with adequate electrical conductivity will be maintained before the working gas exits the generator channel. Experiments testing this method have demonstrated an enthalpy extraction ratio of about 2.6% using pure Ar working gas pre-ionized by a radio frequency (RF) electromagnetic field in a shock-tube facility, although a small-scale disk MHD generator (see Fig. 1.1) was used [18]. It has been suggested that for further improvement of generator performance, the uniform plasma in the generator channel should be realized and the explanation of the experimental results by numerical simulation is required. A numerical study has shown that the generator performance of a seed-free pre-ionized noble gas plasma is comparable to that of alkali metal seeded plasma if an appropriate ionization level is provided at the generator inlet [17], [19]. In another study, the power generation performance using pure Xe, Ar, and He as the working gases has been carried out through r-z two-dimensional numerical simulation. The literature has shown the highest performance can be achieved when using Ar. In case of Xe, the low flow velocity due to the large atomic weight, and/or in case of He, the low Hall parameter due to the large collision cross section of He with electron is the main reason that causes the performance lower than that of Ar. Moreover, as shown in Table 1.1 it is possible to achieve higher generator performance with Ne which has the smaller

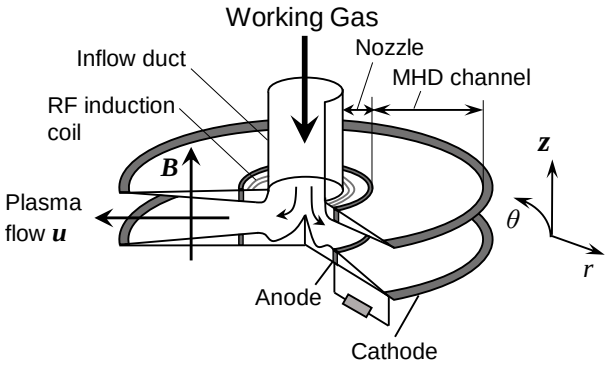

Fig. 1.1 A disk-shaped MHD generator with an RF induction coil for pre-ionization. The working gas is pre-ionized at the generator inlet and flows in the radial (*r*-) direction between two disk walls where a magnetic field is applied perpendicular to the plasma flow (*z*-direction). The output power originating from the Hall electromotive force induced in the radial direction is extracted via a load connected between the ring-shaped anode and cathode.

atomic weight and electron collisional cross section compared with Ar. However, it may be required more power to ionize Ne because of its comparatively high ionization potential.

Another method is the utilization of xenon (Xe), which has the lowest ionization potential among the noble gases (Table 1.1), as a seed material instead of an alkali metal [20]. This is referred to as **xenon-seeded noble gas plasma**. In this method, the pre-ionization process at the generator inlet is required because the self-induced Joule heating cannot ionize Xe to have adequate electrical conductivity like what the alkali metal seeded plasma does, due to the higher ionization potential of Xe compared with alkali metals. In the past, the MHD generator performance using Xe-seeded He (He/Xe) working gas has been studied numerically. However, studies of Xe seeding to other noble gases, the effects of Xe seed fraction (mole% of Xe in the mixture), the uniformity and ionization instability of this kind of plasma have not been conducted widely. Note that, differ to alkali metal seeded plasma, Xe-seeded noble gas plasma is not solidified even it cools to the room temperature; consequently, the complications in handling seed material such as Xe seed recovery, recycle or seed fraction controlling can be avoided.

Table 1.1 Physical properties of each noble gas

Gas species		Xe	Ar	Ne	He
Atomic weight	[g/mole]	131.29	39.95	20.18	4.00
Ionization potential	[eV]	12.1	15.8	21.6	24.6
Electron-neutral particle collision cross section at T_e = 7000 K	[m^2]	9.9×10^{-20}	3.4×10^{-20}	2.3×10^{-20}	9.2×10^{-20}

1.3 Motivation and objectives

The utilization of Xe as a seed material instead of alkali metal can be a promising way for the development of commercial MHD power generation in the future from the viewpoint of system simplification without the need for seed material handling. The addition of Xe to other noble gases may reduce the pre-ionization power. Moreover, Xe is not solidified in the power generation system even the working gas cools to the room temperature. Consequently, it is not required the devices for seed material recovery and recycle, and the system can be expected to be significantly simplified. Therefore, it is worth to study the feasibility and features of Xe-seeded noble gas plasma MHD power generation.

In the present thesis, the feasibility, power generator performance, challenges, and future prospects of a Xe-seeded noble gas plasma MHD generator that utilizes a noble gas Xe as a seed material instead of alkali metal (Cs, K) are clarified through power generation experiment and numerical simulation. To accomplish this aim, the following studies are conducted.

(1) Clarify the plasma behavior in Xe-seeded noble gas plasma in MHD generator by r-θ two-dimensional numerical simulation.

(2) Examine the effect of Xe seed on the generator performance by r-z two-dimensional numerical simulation. The r-θ two-dimensional numerical simulation is carried out and compared with r-z simulation in order to evaluate the generator performance more precisely including the effects of the boundary layer and plasma uniformity.

(3) Carry out the power generation experiment with Xe-seeded noble gas plasma. Then, the numerical simulations based on the experimental conditions and experimental generator are carried out and compared with the experimental results.

1.4 Outline

The dissertation is organized into five chapters. Each chapter is as follows.

In **chapter 1**, the basic concepts of MHD electrical power generation, the research activities on MHD power generation so far are introduced. Then, the motivation and objectives of the dissertation are described.

In **chapter 2**, the plasma behavior and power generation characteristics in Xe-seeded noble gas plasma in MHD generator are examined by r-θ two-dimensional numerical simulation without taking an MHD interaction (an interaction between a conducting fluid and a magnetic field) into account. First, Xe-seeded noble gas plasma is compared with the conventional alkali metal seeded plasma under the same generator and the same operating conditions in order to clarify the differences of plasma uniformity and power generation characteristics in both working gases. Then, the effect that Xe seeding has on plasma behavior and power generations characteristics are examined under different Xe seed fractions.

In **chapter 3**, the effect of Xe seed on the generator performance is examined by taking the MHD interaction into account using r-z two-dimensional numerical simulation. The r-θ two-dimensional numerical simulation is carried out using Ne/Xe working gas and compared with the results from r-z simulation in order to evaluate the generator performance more precisely including the effects of the boundary layer and plasma uniformity.

In **chapter 4**, the power generation experiment with Xe-seeded noble gas plasma is carried out, including the experiment with pure Ar plasma for comparison. Then, the numerical simulations based on the experimental conditions and experimental generator are carried out and compared with the experimental results.

Finally, in **chapter 5**, main conclusions of the present study are summarized and future works are described.

Chapter 2 Plasma Behavior in Xenon-Seeded Noble Gas Plasma MHD Power Generator

2.1 Introduction and objectives

It is known that the performance of an MHD generator is closely related to the plasma behavior inside the generator. For a disk-shaped MHD generator to achieve high performance, the plasma in the generator channel must be uniform and stable in addition to having adequate electrical conductivity. Thus, the study of plasma behavior in the generator is of importance. A numerical study of plasma structure in alkali metal (cesium, for instance)-seeded plasmas has shown that the plasma becomes uniform throughout the generator at an appropriate load resistance, resulting in high performance [21], [22]. In a seed-free pre-ionized inert gas plasma, the relationship between plasma structure and power generation performance has been studied using pure Ar as the working gas through r-θ 2-D simulation, and essentially the same tendency as in the alkali metal-seeded plasma was confirmed [23]. Therefore, it is necessary to examine the plasma behavior in Xe-seeded noble gas plasma MHD power generator.

Based on the above background, in this chapter, the plasma behavior and power generation characteristics in a disk MHD generator with Xe-seeded noble gas plasma are examined by r-θ 2-D numerical simulation. In this chapter, first the Xe-seeded Ar plasma and Cs-seeded Ar plasma are compared under the same generator and the same operating conditions in order to clarify the differences of plasma uniformity and power generation characteristics in Xe-seeded noble gas plasma and in the conventional alkali metal seeded plasma generators. Then, the effects of Xe seed on plasma behavior and power generation characteristics are examined. To clarify the plasma characteristics inherently, an isentropic gas flow and a non-MHD interaction (the MHD effects are not impacting the fluid flow properties) are assumed.

2.2 Governing equations and numerical procedures

2.2.1 Governing equations

Since an isentropic gas flow and a non-MHD interaction are assumed in this study, each property of the working gas (heavy particle) is set to be constant throughout the generator channel, including the total gas pressure p_0, the total gas temperature T_0, the Mach number M, the static gas pressure p, the static temperature T, and the radial gas velocity u_r. The circumferential gas velocity u_θ is assumed to be zero. The governing equations used in the present numerical simulation are as follows.

a) Continuity equations for charged particles (Rate equations)

Ne/Xe: The species in Ne/Xe plasma model consist of neutral (ground state) atoms, metastable atoms, ions of the mother gas (Ne: ionization potential 21.6 eV, excitation energy 16.6 eV), neutral (ground state) atoms, ions of the seed material (Xe: ionization potential 12.1 eV), and electrons. The rate equations for Ne ions, metastable Ne atoms and Xe ions are shown in Eqs. (2.1)–(2.3). In this simulation, as shown in Table 2.1, we considered the direct ionization, three-body recombination, excitation, de-excitation, cumulative ionization and its reverse reaction processes for the mother gas (Ne), and direct ionization, three-body recombination reaction processes for the seed material (Xe). Furthermore, the Penning ionization reaction process that occurs between metastable Ne atom and neutral Xe atom is also included.

A/Xe and Ar/Cs: For Ar/Xe and Ar/Cs plasmas, in which the Penning ionization reaction process hardly occurs, only neutral atoms, ions of the mother gas Ar (Ar: ionization potential 15.6 eV, excitation energy 11.5 eV), neutral atoms, ions of the seed material Xe or Cs (Cs: ionization potential 3.89 eV), and electrons are considered, i.e., only electron collisional ionization and three-body recombination processes are considered. For Ar/Xe, the Eqs. (2.3) and (2.4) are adopted without taking the Penning ionization into account, that is k_{pen} in Eq. (2.3) is set to be zero ($k_{pen} = 0$). For Ar/Cs, the Eqs. (2.4) and (2.5) are adopted.

$$\frac{\partial n_{\mathrm{Ne}}^{+}}{\partial t} + \nabla \cdot (n_{\mathrm{Ne}}^{+}\vec{u}) = \dot{n}_{\mathrm{Ne}}^{+} = k_f n_{\mathrm{Ne}} n_e + k_{cu} n_{\mathrm{Ne^m}} n_e - k_r n_{\mathrm{Ne}}^{+} n_e^2 - k_{rcu} n_{\mathrm{Ne}}^{+} n_e^2 \tag{2.1}$$

$$\begin{aligned}\frac{\partial n_{\mathrm{Ne^m}}}{\partial t} + \nabla \cdot (n_{\mathrm{Ne^m}}\vec{u}) = \dot{n}_{\mathrm{Ne^m}} &= k_{ex} n_{\mathrm{Ne}} n_e + k_{rcu} n_{\mathrm{Ne}}^{+} n_e^2 \\ &- k_{dex} n_{\mathrm{Ne^m}} n_e - k_{cu} n_{\mathrm{Ne^m}} n_e - k_{pen} n_{\mathrm{Ne^m}} n_{\mathrm{Xe}}\end{aligned} \tag{2.2}$$

$$\frac{\partial n_{\mathrm{Xe}}^{+}}{\partial t} + \nabla \cdot (n_{\mathrm{Xe}}^{+}\vec{u}) = \dot{n}_{\mathrm{Xe}}^{+} = k_f n_{\mathrm{Xe}} n_e + k_{pen} n_{\mathrm{Ne^m}} n_{\mathrm{Xe}} - k_r n_{\mathrm{Xe}}^{+} n_e^2 \tag{2.3}$$

$$\frac{\partial n_{\mathrm{Ar}}^{+}}{\partial t}+\nabla\cdot(n_{\mathrm{Ar}}^{+}\vec{u})=\dot{n}_{\mathrm{Ar}}^{+}=k_f n_{\mathrm{Ar}} n_e-k_r n_{\mathrm{Ar}}^{+} n_e^2 \tag{2.4}$$

$$\frac{\partial n_{\mathrm{Cs}}^{+}}{\partial t}+\nabla\cdot(n_{\mathrm{Cs}}^{+}\vec{u})=\dot{n}_{\mathrm{Cs}}^{+}=k_f n_{\mathrm{Cs}} n_e-k_r n_{\mathrm{Cs}}^{+} n_e^2 \tag{2.5}$$

$$n_e=n_{\mathrm{Ne}}^{+}+n_{\mathrm{Xe}}^{+}, or=n_{\mathrm{Ar}}^{+}+n_{\mathrm{Xe}}^{+}, or=n_{\mathrm{Ar}}^{+}+n_{\mathrm{Cs}}^{+} \tag{2.6}$$

Here, k_f is the direct ionization coefficient, k_r the three-body recombination coefficient, k_{ex} the excitation coefficient, k_{dex} the de-excitation coefficient, k_{cu} and k_{rcu} the cumulative ionization coefficient and its reverse reaction coefficient, and k_{pen} the Penning ionization coefficient. n_{Ar} and n_{Ar}^{+} are the neutral atom and ion number density of Ar, n_{Cs} and n_{Cs}^{+} are the neutral atom and ion number density of Cs, n_{Ne}, $n_{\mathrm{Ne^m}}$, and n_{Ne}^{+} are the neutral atom, metastable atom, and ion number densities of Ne, n_{Xe} and n_{Xe}^{+} are the neutral atom and ion number densities of Xe, and n_e is the electron number density. t and $\vec{u}$ denote the time and vector velocity.

In the present study, as shown in Fig. 2.1, at low electron temperature region the three-body recombination coefficient (k_{rL}) by Hinnov [24] is adopted, and at high electron temperature region the three-body recombination coefficient (k_{rH}) by Generalov [25], Owano [26], and McIntyre [27] are adopted for Xe, Ar, and Ne, respectively. The former and the later are connected smoothly by Eq. (2.7).

$$k_r(i)=\frac{k_{rL}\times k_{rH}(i)}{k_{rL}+k_{rH}(i)}, (i=\mathrm{Xe},\mathrm{Ar},\mathrm{Ne}) \tag{2.7}$$

$$k_{rL}=1.09\times10^{-20}T_e^{-\frac{9}{2}} \tag{2.8}$$

$$k_{rH}(\mathrm{Xe})=\frac{1}{3}\times1.21\times10^{-35}\times\frac{1}{T_e^2}\exp\left(\frac{55300}{T_e}\right) \tag{2.9}$$

$$k_{rH}(\mathrm{Ar})=3.3\times10^{-44}\left(\frac{135300}{T_e}+2\right)\exp\left(\frac{47800}{T_e}\right) \tag{2.10}$$

$$k_{rH}(\mathrm{Ne})=2.96\times10^{-45}\left(\frac{192700}{T_e}+2\right)\exp\left(\frac{58040}{T_e}\right) \tag{2.11}$$

The three-body recombination by Hinnov [24] is adopted for Cs [Eq. (2.8)].

Since it can be assumed that detailed balancing occurs at local thermodynamic equilibrium [7], the ionization rate coefficient k_f is written using the three-body recombination coefficient k_r as shown in Eq. (2.12).

$$k_f(i)=k_r(i)\cdot2\frac{g_i^{+}}{g_i}\left(\frac{2\pi m_e k_B T_e}{\hbar^2}\right)^{\frac{3}{2}}\exp\left(-\frac{\epsilon_i}{k_B T_e}\right) \tag{2.12}$$

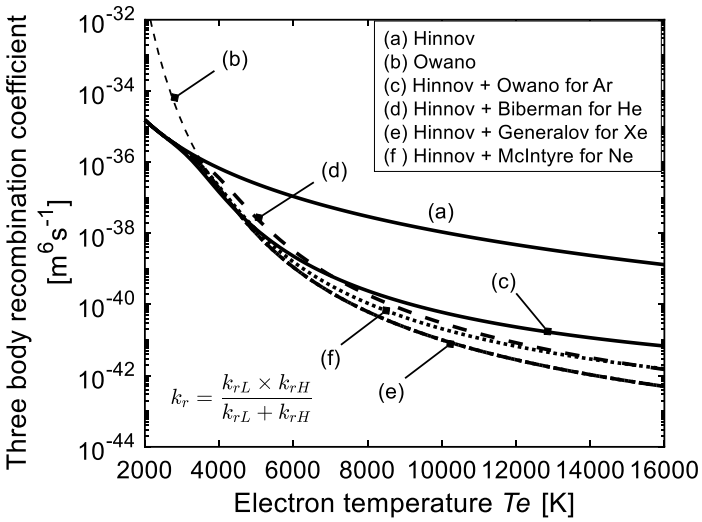

Fig. 2.1 Three-body recombination coefficients as a function of electron temperature. The three-body recombination coefficient for He by Biberman [28] is also included.

Table 2.1 Plasma reaction model

Types	Reactions	Rate coefficients[a]	Ref.
Direct ionization	$\mathrm{Ar} + \mathrm{e}^- \xrightarrow{k_f} \mathrm{Ar}^+ + 2\mathrm{e}^-$	Eq. (2.12)	–
Three-body recombination	$\mathrm{Ar}^+ + 2\mathrm{e}^- \xrightarrow{k_r} \mathrm{Ar} + \mathrm{e}^-$	Eq. (2.7)	–
Direct ionization	$\mathrm{Xe} + \mathrm{e}^- \xrightarrow{k_f} \mathrm{Xe}^+ + 2\mathrm{e}^-$	Eq. (2.12)	–
Three-body recombination	$\mathrm{Xe}^+ + 2\mathrm{e}^- \xrightarrow{k_r} \mathrm{Xe} + \mathrm{e}^-$	Eq. (2.7)	–
Direct ionization	$\mathrm{Cs} + \mathrm{e}^- \xrightarrow{k_f} \mathrm{Cs}^+ + 2\mathrm{e}^-$	$-\ [m^3/s]$	[24], [7][b]
Three-body recombination	$\mathrm{Cs}^+ + 2\mathrm{e}^- \xrightarrow{k_r} \mathrm{Cs} + \mathrm{e}^-$	$1.09 \times 10^{-20} T_e^{-\frac{9}{2}}\ [m^6/s]$	[24]
Direct ionization	$\mathrm{Ne} + \mathrm{e}^- \xrightarrow{k_f} \mathrm{Ne}^+ + 2\mathrm{e}^-$	Eq. (2.12)	–
Three-body recombination	$\mathrm{Ne}^+ + 2\mathrm{e}^- \xrightarrow{k_r} \mathrm{Ne} + \mathrm{e}^-$	Eq. (2.7)	–
Excitation	$\mathrm{Ne} + \mathrm{e}^- \xrightarrow{k_{ex}} \mathrm{Ne^m} + \mathrm{e}^-$	$6.825 \times 10^{-22} T_e^{1.69} \cdot \exp\left(-\frac{192630}{T_e}\right)\ [m^3/s]$	[29]
De-excitation	$\mathrm{Ne^m} + \mathrm{e}^- \xrightarrow{k_{dex}} \mathrm{Ne} + \mathrm{e}^-$	$2.0 \times 10^{-16} [m^3/s]$	[30]
Cumulative ionization	$\mathrm{Ne^m} + \mathrm{e}^- \xrightarrow{k_{cu}} \mathrm{Ne}^+ + 2\mathrm{e}^-$	$4.027 \times 10^{-17} T_e^{0.74} \cdot \exp\left(-\frac{58020}{T_e}\right)\ [m^3/s]$	[29]
Reverse of cumulative ionization	$\mathrm{Ne}^+ + 2\mathrm{e}^- \xrightarrow{k_{rcu}} \mathrm{Ne^m} + \mathrm{e}^-$	$-\ [m^3/s]$	[29],[7][b]
Penning ionization	$\mathrm{Ne^m} + \mathrm{Xe} \xrightarrow{k_{pen}} \mathrm{Ne} + \mathrm{Xe}^+ + e^-$	$7.5 \times 10^{-17}\ [m^3/s]$	[29]

[a]The electron temperature T_e is in Kelvin.
[b]Reaction-rate coefficient derived from detailed balance.

b) Generalized Ohm's law

$$\vec{j}+\frac{\beta}{|\vec{B}|}\vec{j}\times\vec{B}=\sigma\left(\vec{E}+\vec{u}\times\vec{B}+\frac{\nabla p_e}{en_e}\right) \tag{2.13}$$

Here, $\vec{j}$ is the current density, $\vec{B}$ the magnetic flux density, $\vec{E}$ the electric field, $\vec{u}$ the gas velocity, p_e the electron pressure, e the elementary charge, β the Hall parameter, and σ the electrical conductivity. The electrical conductivity σ and the Hall parameter β are defined by Eq. (2.14).

$$\sigma=\frac{e^2 n_e}{m_e\nu_e},\qquad \beta=\frac{e|\vec{B}|}{m_e\nu_e} \tag{2.14}$$
$$\nu_e=\sum_h \nu_{eh}=\sum_h c_e Q_{eh} n_h$$

Here, c_e is the mean thermal velocity of the electron [Eq. (2.15)], Q_{eh} the average momentum transfer cross section of an electron with a heavy particle h. The average momentum transfer cross section of an electron with an ion Q_{ei} [Eq. (2.16)] is taken from [6] and an electron with a neutral atom Q_{en} [for Xe, Ar, Ne, He, Eqs. (2.17)–(2.20)] is obtained by convolving the cross section listed in [31] over a Maxwellian distribution (Fig. 2.2). The average momentum transfer cross section of an electron a neutral atom Cs [Eq. (2.21)] is taken form [6].

$$c_e=\sqrt{\frac{8k_B T_e}{\pi m_e}} \tag{2.15}$$

$$Q_{ei}=6\pi\times\left(\frac{e^2}{12\pi\epsilon_0 k_B T_e}\right)^2 \ln\left\{12\pi\left(\frac{\epsilon_0 k_B}{e^2}\right)^{\frac{3}{2}}\sqrt{\frac{T_e^3}{n_e}}\right\} \tag{2.16}$$

$$Q_{en}(\mathrm{Xe})=\begin{cases} Te<5000\ K\text{: } 1.81\times10^{-33}T_e^4-2.68\times10^{-29}T_e^3+1.51\times10^{-25}T_e^2 \\ \qquad -3.76\times10^{-22}T_e+3.79\times10^{-19} \\ Te\geq 5000\ K\text{: } 4.29\times10^{-36}T_e^4-2.41\times10^{-31}T_e^3+3.96\times10^{-27}T_e^2 \\ \qquad -3.71\times10^{-24}T_e+4.09\times10^{-21} \end{cases} \tag{2.17}$$

$$Q_{en}(\mathrm{Ar})=-9.63\times10^{-33}T_e^3+2.53\times10^{-28}T_e^2+3.46\times10^{-24}T_e+4.96\times10^{-22} \tag{2.18}$$
$$Q_{en}(\mathrm{Ne})=4.79\times10^{-33}T_e^3-1.91\times10^{-28}T_e^2+2.66\times10^{-24}T_e+1.24\times10^{-20} \tag{2.19}$$
$$Q_{en}(\mathrm{He})=7.42\times10^{-33}T_e^3-3.12\times10^{-28}T_e^2+3.36\times10^{-24}T_e+8.16\times10^{-20} \tag{2.20}$$
$$Q_{en}(\mathrm{Cs})=\frac{4}{3}\times0.4\times10^{-17} \tag{2.21}$$

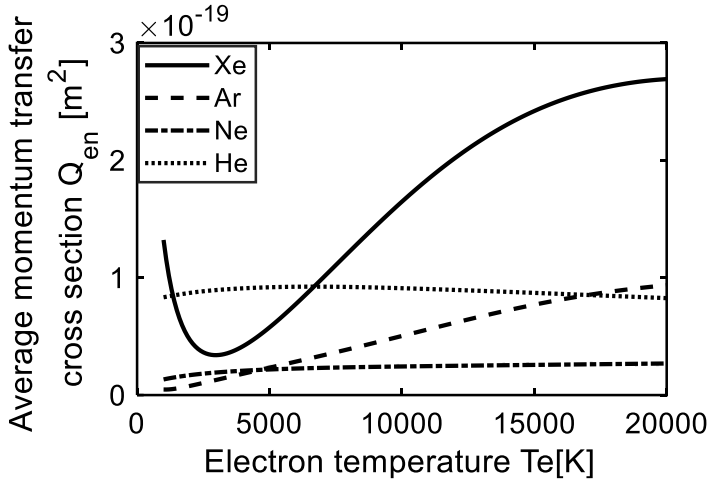

Fig. 2.2 The average momentum transfer cross section of an electron with a neutral atom of noble gas as a function of electron temperature.

c) Electron energy equation

$$\frac{\partial U_e}{\partial t} + \nabla \cdot [(U_e + p_e)\vec{u}] = \frac{|\vec{j}|^2}{\sigma} + \vec{u} \cdot \nabla p_e - \nabla \cdot \vec{q}_e - \frac{3}{2} k_B n_e (T_e - T_g) \sum_h \frac{2m_e}{m_h} \nu_{eh} \tag{2.22}$$

$$U_e = \frac{3}{2} n_e k_B T_e + \sum_i \epsilon_i n_i \tag{2.23}$$

Here, U_e is the electron energy density, $\vec{q}_e$ the electron heat flux, k_B the Boltzmann constant, T_g the gas temperature (heavy particle), m_e the electron mass, m_h the mass of the heavy particle h ($h = \mathrm{Ar}$, Ar^+, Xe, Xe^+ for Ar/Xe, $h = \mathrm{Ar}$, Ar^+, Cs, Cs^+ for Ar/Cs, and $h = \mathrm{Ne}$, Ne^+, Ne^{m}, Xe, Xe^+ for Ne/Xe), n_i the number density of particle i ($i = \mathrm{Ar}^+$, Xe^+ for Ar/Xe, $i = \mathrm{Ar}^+$, Cs^+ for Ar/Cs, and $i = \mathrm{Ne}^+$, Ne^{m}, Xe^+ for Ne/Xe), and ϵ_i the ionization or excitation energy of particle i.

d) Maxwell's equations

The electromagnetic field in the non-equilibrium plasma can be described by the Maxwell's equations, as follows.

$$\nabla \cdot \vec{D} = \rho_c \tag{2.24}$$

$$\nabla \times \vec{E} = -\frac{\partial \vec{B}}{\partial t} \tag{2.25}$$

$$\nabla \cdot \vec{B} = 0 \tag{2.26}$$

$$\nabla \times \vec{H} = \vec{j} + \frac{\partial \vec{D}}{\partial t} \tag{2.27}$$

In a typical plasma in the MHD generator where the Debye length, in the order of 10^{-7} m, is much shorter than the characteristic length of the plasma, the plasma can be regarded as electrically neutral. Moreover, the magnetic Reynolds number which is defined as $R_m = \mu\sigma L u$, where μ is the permeability, σ the electrical conductivity, L the characteristic length, and u the velocity, is in the order of 10^{-2}, very small compared with unity. The magnetic Reynolds number can also be interpretated as the ratio of the induced magnetic flux density due to the plasma flow motion to the stationary original magnetic flux density which is applied externally. Under the condition of $R_m \ll 1$, the magnetic flux density can be regarded as stationary. Under the assumptions of charge neutrality and low magnetic Reynolds number, the Maxwell equations are simplified as follows [6].

$$\nabla \times \vec{\mathrm{E}} = \vec{0}, \qquad \nabla \cdot \vec{j} = 0 \tag{2.28}$$

2.2.2 Numerical procedures

a) Scheme for hyperbolic equations

The hyperbolic equations (2.1)–(2.5) and (2.22) can be transformed into a system of equations as follows.

$$\frac{\partial U}{\partial t} + \frac{\partial E}{\partial x} + \frac{\partial F}{\partial y} = \frac{\partial E_v}{\partial x} + \frac{\partial F_v}{\partial y} + S \tag{2.29}$$

Here,

$$U = \begin{bmatrix} n_i \\ U_e \end{bmatrix}, E = \begin{bmatrix} n_i u_x \\ (U_e + p_e)u_x \end{bmatrix}, F = \begin{bmatrix} n_i u_y \\ (U_e + p_e)u_y \end{bmatrix}, E_v = \begin{bmatrix} 0 \\ -q_{ex} \end{bmatrix}, F_v = \begin{bmatrix} 0 \\ -q_{ey} \end{bmatrix}$$

$$S = \begin{bmatrix} \dot{n_i} - n_i u_r \dfrac{1}{h_z}\dfrac{\partial h_z}{\partial r} \\ \dfrac{|\vec{j}|^2}{\sigma} + \vec{u}\cdot\nabla p_e - \dfrac{3}{2}k_B n_e (T_e - T_g)\displaystyle\sum_h \frac{2m_e}{m_h}\nu_{eh} - [u_r(U_e + p_e) + q_{er}]\frac{1}{h_z}\frac{\partial h_z}{\partial r} \end{bmatrix}$$

where n_i is the number density of particle i ($i = \mathrm{Ar}^+$, Xe^+ for Ar/Xe, $i = \mathrm{Ar}^+$, Cs^+ for Ar/Cs, and $i = \mathrm{Ne}^+$, $\mathrm{Ne^m}$, Xe^+ for Ne/Xe), and q_{ex}, q_{ey} and q_{er} are the electron heat fluxes in x-, y- and r- direction, respectively.

The system of equations (2.29) can be transformed into the generalized coordinate system (ξ-η plane) as follows.

$$\frac{\partial \hat{U}}{\partial t} + \frac{\partial \hat{E}}{\partial \xi} + \frac{\partial \hat{F}}{\partial \eta} = \frac{\partial \hat{E}_v}{\partial \xi} + \frac{\partial \hat{F}_v}{\partial \eta} + \hat{S} \tag{2.30}$$

Here,

$$\begin{aligned} \hat{U} &= \frac{U}{J}, \qquad \hat{E} = y_\eta E - x_\eta F, \qquad \hat{F} = -y_\xi E + x_\xi F, \\ \hat{E}_v &= y_\eta E_v - x_\eta F_v, \qquad \hat{F}_v = -y_\xi E_v + x_\xi F_v, \qquad \hat{S} = \frac{S}{J} \end{aligned} \tag{2.31}$$

The second-order central difference method is used to evaluate metrics, and is expressed as follows.

$$\begin{aligned} \frac{\xi_y}{J} = x_\eta = \frac{x_{i,j+1} - x_{i,j-1}}{2}, \qquad -\frac{\xi_x}{J} = y_\eta = \frac{y_{i,j+1} - y_{i,j-1}}{2} \\ -\frac{\eta_y}{J} = x_\xi = \frac{x_{i+1,j} - x_{i-1,j}}{2}, \qquad \frac{\eta_x}{J} = y_\xi = \frac{y_{i+1,j} - y_{i-1,j}}{2} \end{aligned} \tag{2.32}$$

The advection terms in Eq. (2.30) are discretized using the Harten-Yee second-order upwind TVD scheme [32], and the heat flux terms are discretized using the second-order differential method. Then, the equations are solved using the Fractional Step Method with a time step dt that satisfies the CFL condition.

Boundary conditions

The inlet condition for each particle number density is determined from the value at an equilibrium state ($\dot{n}^+_{\mathrm{Ar}} = 0,\ \dot{n}^+_{\mathrm{Xe}} = 0$ for Ar/Xe, $\dot{n}^+_{\mathrm{Ar}} = 0,\ \dot{n}^+_{\mathrm{Cs}} = 0$ for Ar/Cs, and $\dot{n}^+_{\mathrm{Ne}} = 0, \dot{n}_{\mathrm{Ne^m}} = 0, \dot{n}^+_{\mathrm{Xe}} = 0$ for Ne/Xe,) for a given electron temperature or pre-ionization power ratio. The inlet condition for electron energy is given as $U_e = \frac{3}{2} n_e k_B T_e + \sum_i \epsilon_i n_i$ with the properties at the inlet. The outlet condition is determined by the free outflow boundary condition.

b) Scheme of elliptic partial differential equation

The elliptic partial differential equation shown in Eq. (2.33) is derived from Eqs. (2.13), (2.28), and the electric field $\vec{E} = -\nabla\phi$, where ϕ is the electric potential. The equation is discretized using the second-order central difference method and is solved using the BiCG-Safe method [33], [34].

$$\begin{aligned} &\frac{\partial}{\partial r}\left\{\frac{r h_z \sigma}{1+\beta^2}\left[\left(-\frac{\partial\phi}{\partial r} + \frac{1}{e n_e}\frac{\partial p_e}{\partial r}\right) - \beta\left(-\frac{1}{r}\frac{\partial\phi}{\partial r} - u_r B_z + \frac{1}{e n_e}\frac{\partial p_e}{r\partial\theta}\right)\right]\right\} \\ &+\frac{\partial}{\partial\theta}\left\{\frac{h_z \sigma}{1+\beta^2}\left[\beta\left(-\frac{\partial\phi}{\partial r} + \frac{1}{e n_e}\frac{\partial p_e}{\partial r}\right) + \left(-\frac{1}{r}\frac{\partial\phi}{\partial\theta} - u_r B_z + \frac{1}{e n_e}\frac{\partial p_e}{r\partial\theta}\right)\right]\right\} = 0 \end{aligned} \tag{2.33}$$

Here, h_z is the height of the generator channel.

Boundary conditions

The boundary condition for the electric potential in Eq. (2.33) is given as $\phi = 0$ on the anode and as $\phi = V_{out}$ on the cathode, where V_{out} is the output voltage. V_{out} should satisfy

the relation of $V_{out} = I_{out} \times R_L$, where R_L is the external load resistance, I_{out} is the output current which is expressed as

$$I_{out} = \int_A j_r dA \tag{2.34}$$

and the radial current density j_r is calculated from Eq. (2.13).

2.2.3 Numerical region

A cross-sectional view of the disk-shaped Hall-type MHD generator in the r-z plane is shown in Fig. 2.3. The numerical region is carried out in the r-θ plane from downstream edge of the anode (r = 90 mm) to the upstream edge of the cathode (r = 200 mm). To keep the Mach number constant in the whole generator channel under the isentropic gas flow, the cross-sectional area $A = 2\pi r h_z$ for the radial gas flow was set to be constant along the radius. There are 51 grids (50 cells) in the r-direction and 360 grids (360 cells) in the θ-direction. The mesh sizes in r- and θ-direction are $\Delta r =$ 2.2 mm and $\Delta\theta =$ π/180, respectively.

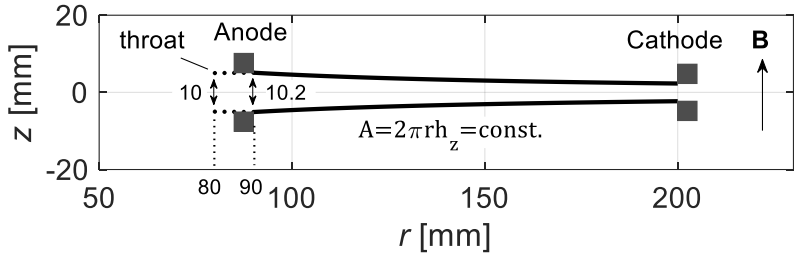

Fig. 2.3 Cross-sectional view of disk-shaped MHD generator in *r*-*z* plane. The gas flows in the *r*-direction.

2.3 Comparison of xenon-seeded noble gas plasma with alkali metal seeded plasma

In this section, the Xe-seeded Ar plasma and Cs-seeded Ar plasma are compared in order to clarify the differences of plasma uniformity and power generation characteristics in Xe-seeded noble gas plasma and in the conventional alkali metal seeded plasma generators. Note that in alkali metal seeded plasma, Ar is usually selected as the mother gas. Therefore, in this study, Ar is selected as the mother gas in order to conduct the comparative study between Xe-seeded plasma and alkali metal seeded plasma.

2.3.1 Numerical conditions

Table 2.2 shows the numerical conditions. The numerical simulations are conducted under a total pressure of 0.30 MPa, total temperature of 2500 K, Mach number of 1.49, and magnetic flux density of 4.0 T. The applied magnetic flux density is assumed to hold in the z-direction only and to be constant throughout the generator. Ar/Xe and Ar/Cs are selected as the working gas with seed fractions (mole fraction) set to 1.0×10^{-3} and 1.0×10^{-4}, respectively. Note that for Ar/Cs, the Cs seed fraction is set to its typical value. For Ar/Xe, on the other hand, setting too low seed fraction will fade out the role of Xe as a seed material owing the small difference in ionization potential of Ar and Xe, whereas setting too high seed fraction will reduce the flow velocity to be lower than that of Ar/Cs owing to the large atomic weight of Xe. The Saha ionization equilibrium[1] is assumed at the generator inlet, and the inlet electron temperature is set to 5000 K for Ar/Cs, thus the ionization degree of Cs will be almost unity (fully ionized seed) and the total ionization degree (=total ion number density / total atomic number density before ionization) will be 1.0×10^{-4}, whereas the ionization degree of Ar is around 3.54×10^{-9}. Accordingly, the inlet ionization degree of Ar/Xe is set to 1.0×10^{-4} with the corresponding inlet electron temperature of 6760 K.

Table 2.2 Numerical conditions

Working gas		Ar/Xe	Ar/Cs
Total pressure	[MPa]	0.30	
Total temperature	[K]	2500	
Mach number	[–]	1.49	
Magnetic flux density	[T]	4.0	
Seed fraction	[–]	1.0×10^{-3}	1.0×10^{-4}
Inlet ionization degree	[–]	1.0×10^{-4}	(1.0×10^{-4})
Inlet electron temperature	[K]	6760	5000
Load resistance	[Ω]	0.01 – 5.00	

2.3.2 Power generation characteristics

The output voltage-current characteristics under Ar/Xe and Ar/Cs working gases are shown in Fig. 2.4. The uniform plasma appears at the closed point. From the figure, it can be seen that there exits an optimum load resistance for providing maximum output power. At that time, the output powers in Ar/Xe (R_L = 2.0 Ω, P_{out} = 194 kW) and Ar/Cs (R_L = 2.0 Ω, P_{out} = 191 kW) are almost the same. At low load resistance, the output power in Ar/Xe is lower than that in Ar/Cs,

[1] For Ar/Cs or Ar/Xe, this assumption is the same as the assumption that at generator inlet the plasma is in an equilibrium state (subsection 2.2.2). At the equilibrium state, $\dot{n}_i^+ = k_f n_n n_e - k_r n_i^+ n_e^2 = 0$. Thus, $\frac{n_i^+ n_e}{n_n} = \frac{k_f}{k_r} = 2\frac{g_i^+}{g_i}\left(\frac{2\pi m_e k_B T_e}{h^2}\right)^{\frac{3}{2}} \exp\left(-\frac{\epsilon_i}{k_B T_e}\right)$ which is just the Saha equilibrium equation.

additionally the range of load resistance for achieving uniform plasma is also narrower compared with Ar/Cs. On the other hand, when the load resistance increases over the optimal value, the output voltage saturates (Ar/Xe) or drastically drops (Ar/Cs), meaning that the output power decreases.

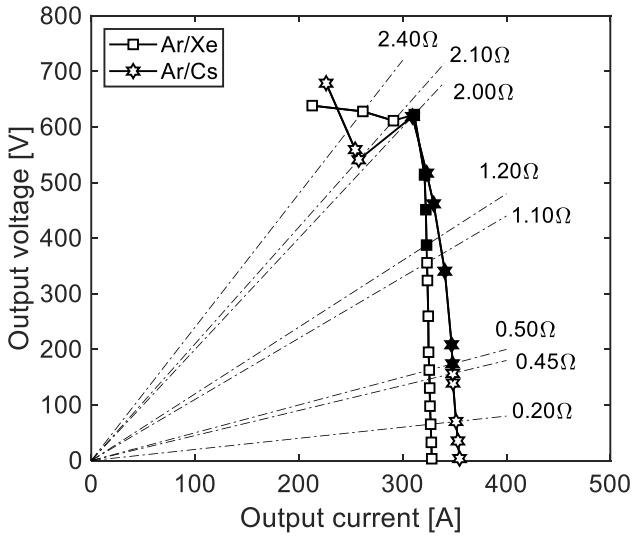

Fig. 2.4 Output voltage-current characteristics.

Fig. 2.5 shows the distributions of electron temperature, total ionization degree, electrical conductivity and Hall parameter at an optimum load resistance of 2.0 Ω. Each value is averaged in θ-direction. At optimum load resistance, the electron temperature in generator channel in both Ar/Xe and Ar/Cs is around 5000 – 7000 K [Fig. 2.5(a)]. In this electron temperature region, as will be described later, the seed (Cs) is fully ionized for Ar/Cs, whereas for Ar/Xe the ionization degree in the generator channel remains almost constant owing to the low three-body recombination coefficient of Xe and Ar, as a result the total ionization degree in Ar/Xe is almost the same as that in Ar/Cs [Fig. 2.5(b)]. On the other hand, the electrical conductivity [Fig. 2.5(c)] and Hall parameter [Fig. 2.5(d)] in Ar/Cs are lower than those in Ar/Xe. This is attributed to the higher electron collision frequency in Ar/Cs than that in Ar/Xe which is a result of large collision cross section of Cs with electron [see Fig. 2.2 and Eq. (2.21)]. Note that for Ar/Cs, the electron temperature at the generator inlet was set to 5000 K, a condition at which the Cs seed is almost fully ionized; however, this electron temperature does not always provide the maximum output power under the operating conditions set here. As shown in Fig. 2.5(a), the electron temperature inside the generator at the optimum load resistance of 2.0 Ω is approximately 7000 K, increases drastically just after the generator inlet. At that time, the total ionization degree (electron number density) keeps almost constant [Fig. 2.5(b)], but due to the increase in electron collision frequency

which results from the increase in electron temperature, both the electrical conductivity [Fig. 2.5(c)] and Hall parameter [Fig. 2.5(d)] decrease rapidly just after the generator inlet.

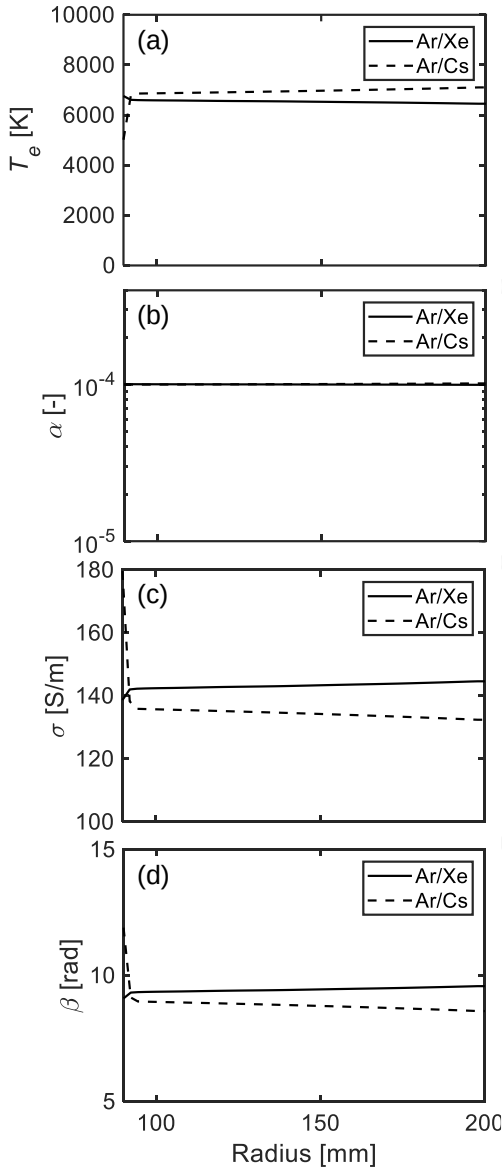

Fig. 2.5 Distributions of (a) electron temperature T_e, (b) total ionization degree α, (c) electrical conductivity σ and (d) Hall parameter β at an optimum load resistance of 2.0 Ω. Value is averaged in θ-direction.

By neglecting the electron pressure gradient, the electrical power output density is expressed as follows.

$$P_e = -\vec{j} \cdot \vec{E} = \frac{\beta^2}{1+\beta^2} K_h (1 - K_h) \sigma u_r^2 B_z^2 \tag{2.35}$$

Here, $K_h = -E_r/\beta u_r B_z$ is the loading parameter, and E_r is the electric field in the r-direction. The loading parameter and electrical power output density at an optimum load resistance of 2.0 Ω are shown in Fig. 2.6. Although the electrical conductivity in Ar/Xe is slightly higher than that in Ar/Cs [Fig. 2.5(c)], as shown in Fig. 2.6(a) the loading parameter in Ar/Xe is slightly slower than that in Ar/Cs [for $0 < K_h < 0.5$, K_h (1– K_h) decreases with decreasing K_h], as a result the power output densities in both working gases are almost the same [Fig. 2.6(b)].

As described above, it can be seen that under an identical inlet ionization degree, the total ionization degrees in the generator channel in Ar/Xe and Ar/Cs are almost the same at optimum load resistance, thus the same level of output power is achieved.

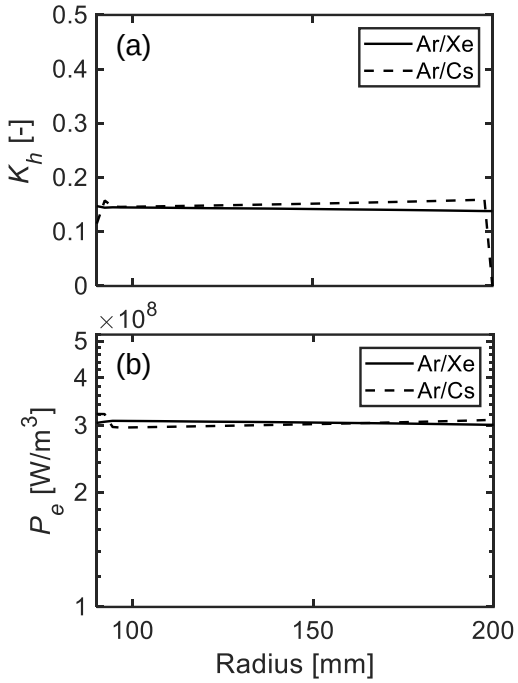

Fig. 2.6 Distributions of (a) loading parameter and (b) electrical power output density at an optimum load resistance. Value is averaged in θ-direction.

2.3.3 Plasma structure

Fig. 2.7 shows the plasma structures (electron temperature distributions) at representative load resistances in Ar/Xe and Ar/Cs. As shown in the figure, at optimum load resistance uniform plasma is realized. On the other hand, at low load resistance nonuniform plasma structure rotating clockwise in case of Ar/Xe and rotating counter clockwise in case of Ar/Cs occurs. At high load resistance, nonuniform spiral plasma structure rotating clockwise occurs in both Ar/Xe and Ar/Cs. For Ar/Xe, as shown in Fig. 2.8 when a higher inlet electron temperature of 7400 K is set, nonuniform spiral plasma structure rotating counter clockwise is obtained at low load resistance.

These nonuniform plasma structures result in the deterioration of generator performance. The nonuniform plasma structure at low load resistance effectively increases the internal resistance of the generator, and as shown in Fig. 2.4 the effective internal resistance (the slope of output voltage-current characteristics) in Ar/Xe becomes larger than that in Ar/Cs, as a result the output power of Ar/Xe becomes smaller than Ar/Cs. At high load resistance, for Ar/Cs in comparison with Ar/Xe, there exists large sparse spiral structures, a region at which the reverse-flow phenomena of current occurs, and between the sparse spiral there are regions at which the electron temperature is low, as a result the output voltage and current rapidly decrease (Fig. 2.4). On the other hand, the spiral structure of Ar/Xe is relatively dense and the electron temperature is relatively high throughout the region, as a result the output voltage remains in saturated state.

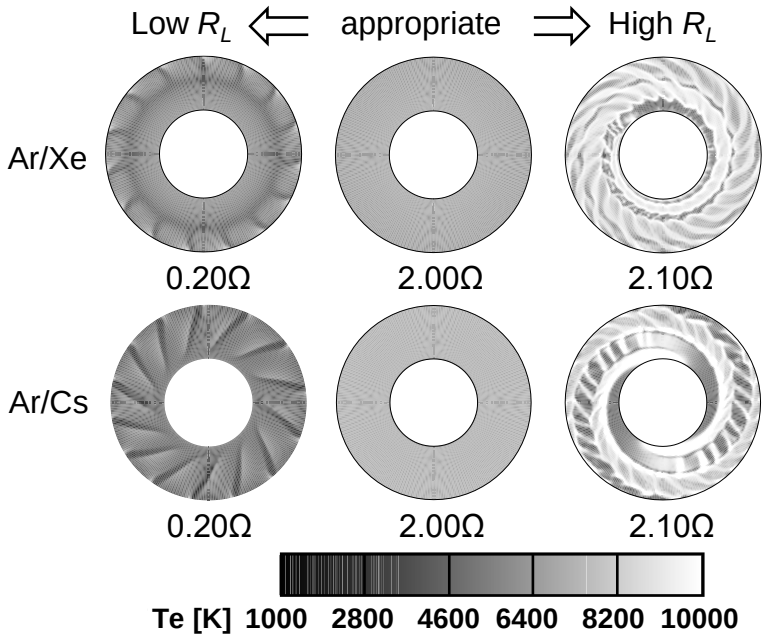

Fig. 2.7 Electron temperature distribution under each working gas.

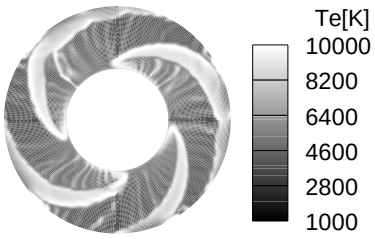

Fig. 2.8 Plasma structure (electron temperature distribution) at a higher inlet electron temperature of 7400 K, a load resistance of 0.01 Ω in Ar/Xe. The plasma becomes nonuniform with a spiral shape rotating counter clockwise.

2.3.4 Plasma stability and uniformity

It is well-known that in alkali metal-seeded plasma, ionization instability occurs when the seed is partially ionized, resulting in a nonuniform plasma structure in the generator [35], [36]. However, in Xe-seeded plasma, the ionization instability is not always caused by the partial ionization of the seed.

Fig. 2.9 shows the distributions of ionization degree of seed material (Xe and Cs) at low and optimum load resistances under each working gas. These ionization degrees are corresponding to the plasma structure (electron temperature distribution) at low and optimum load resistance of each working gas in Fig. 2.7. As seen in the figure, in Ar/Cs the seed is fully ionized (plasma is uniform) at optimum load resistance, whereas at low load resistance the ionization degree of the seed locally decreases and the plasma structure becomes nonuniform. In Ar/Xe, on the other hand, even under optimum load resistance at which a uniform plasma is achieved, the seed is not fully ionized (ionization degree of Xe is around 0.03). In other words, in the Xe-seeded noble gas plasma, a uniform plasma structure is maintained even under partial ionization of Xe seed which is different from Cs-seeded plasma.

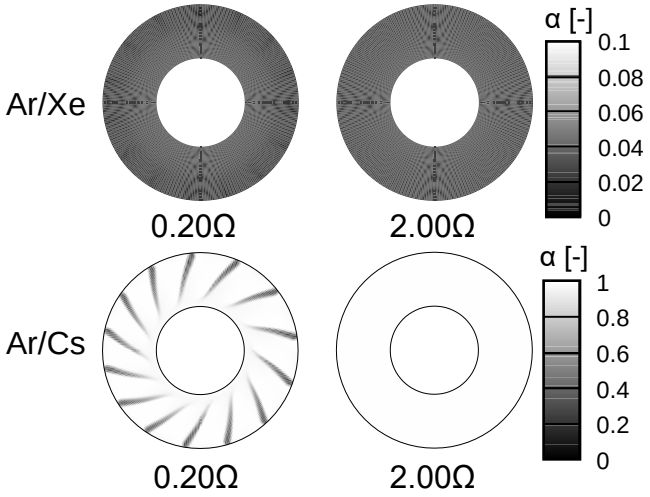

Fig. 2.9 Distributions of ionization degree of seed at low and optimum load resistances under each working gas.

The stability of plasma in the MHD generator has been studied using linear perturbation theory [6], [35]. In this theory, it is stated that plasma becomes stable when the critical Hall parameter β_{crit} exceeds the Hall parameter β [35]. The critical Hall parameter β_{crit} is derived as follows:

$$\beta_{crit} = \left(\frac{A_T^2 - \sigma_T^2}{n_T^2} \right)^{\frac{1}{2}} \tag{2.36}$$

$$A_T = \frac{T_e}{A}\frac{dA}{dT_e}, \qquad \sigma_T = \frac{T_e}{\sigma}\frac{d\sigma}{dT_e}, \qquad n_T = \frac{T_e}{n_e}\frac{dn_e}{dT_e} \tag{2.37}$$

where A is the electron energy loss due to collisions and is written as

$$A = \frac{3}{2}k_B n_e (T_e - T_g)\sum_h \frac{2m_e}{m_h}\nu_{eh} \tag{2.38}$$

where the electron number density of the plasma is assumed to be determined by the Saha equation.

Based on this theory, the critical Hall parameter and Hall parameter are calculated for the Ar/Xe and Ar/Cs plasma as a function of electron temperature under the conditions as shown in Table 2.2, the results of which are given in Fig. 2.10. As seen in the figure, for Ar/Cs, there exists a range of electron temperature (around 4300 – 5800 K) in which the critical Hall parameter exceeds the Hall parameter. For Ar/Xe, on the other hand, the critical Hall parameter is lower than the Hall parameter when the electron temperature is below 9300 K.

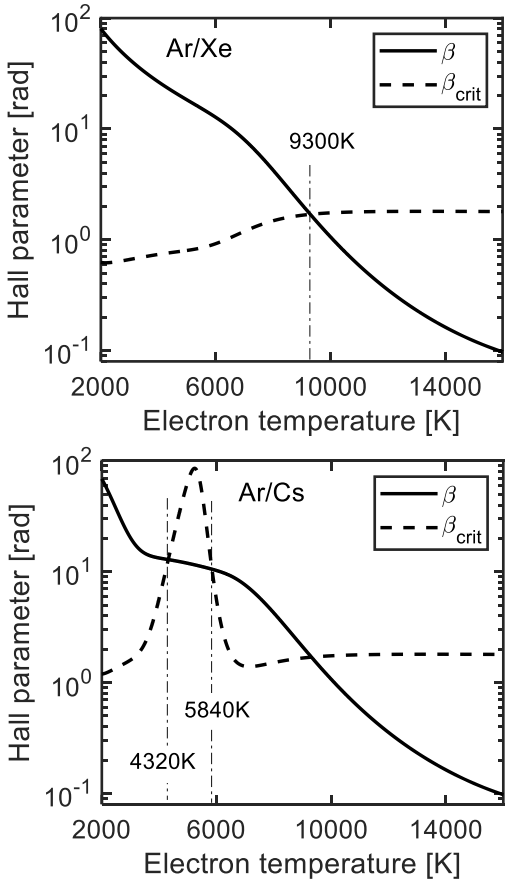

Fig. 2.10 Hall parameter β (solid line) and critical Hall parameter β_{crit} (dashed line) as a function of electron temperature under each working gas.

Fig. 2.11 shows the distribution of electron temperature T_e at different load resistances at $\theta = 0$ rad. For Ar/Cs, the electron temperature in the generator channel at the lower limit of load resistance 0.50 Ω at which the stable plasma is achieved is approximately 4300 – 5000 K [Fig. 2.11 (b)]. In this electron temperature region, the critical Hall parameter is higher than the Hall parameter, thus the plasma becomes stable (uniform). At the upper limit of load resistance 2.00 Ω where the stable plasma is achieved, the electron temperature in the generator channel is approximately 5000 – 7100 K. Although, this electron temperature slightly exceeds the predicted value from linear perturbation theory of 4300 – 5800 K, stable and uniform plasma is still maintained which is thought to be attributed to the slow response of Ar plasma due to the small three-body recombination coefficient of Ar (at $T_e \geq$ 5000 K, over an order of magnitude smaller than Cs, see Fig. 2.1). As a side note, under the assumption that the three-body recombination coefficient of Ar is the same as that of Cs, the electron temperature in the generator channel at the upper limit of load resistance 1.40 Ω at which the stable plasma is achieved is approximately 5000 – 5800 K (Fig. 2.12), almost the same as the range of electron temperature predicted by the linear perturbation theory. However, at load resistance lower or higher than the appropriate load resistances for achieving stable plasma, the critical Hall parameter becomes lower than the Hall parameter. At a low load resistance of 0.45 Ω the electron temperature decreases to 3000 K, and at a high load resistance of 2.10 Ω the electron temperature varies in the range of 4000 – 14000 K [Fig. 2.11 (b)], in any case the plasma becomes nonuniform.

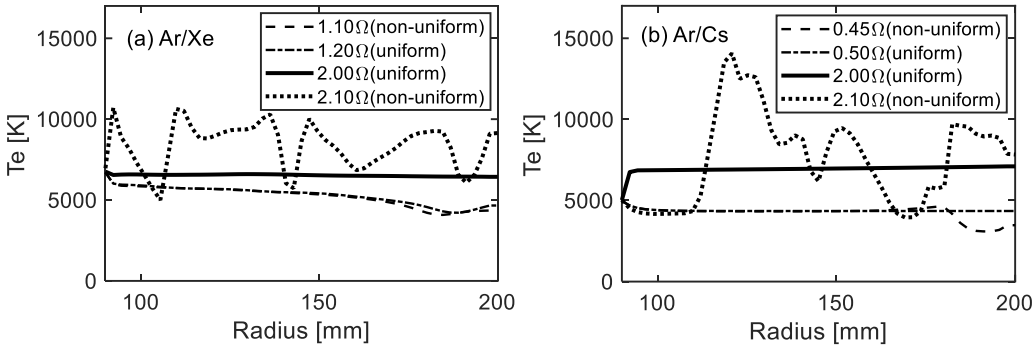

Fig. 2.11 Distribution of electron temperature T_e at different load resistances at $\theta = 0$ rad. As also appeared in Fig. 2.4, theses load resistances are selected at the upper limit of the low load resistance region (nonuniform plasma, 1.10 Ω for Ar/Xe and 0.45 Ω for Ar/Cs), the lower limit of the appropriate load resistance region (uniform plasma, 1.20 Ω for Ar/Xe and 0.50 Ω for Ar/Cs), the upper limit of the appropriate load resistance region (uniform plasma, 2.00 Ω for both Ar/Xe and Ar/Cs), and the lower limit of the high load resistance region (nonuniform plasma, 2.10 Ω for both Ar/Xe and Ar/Cs).

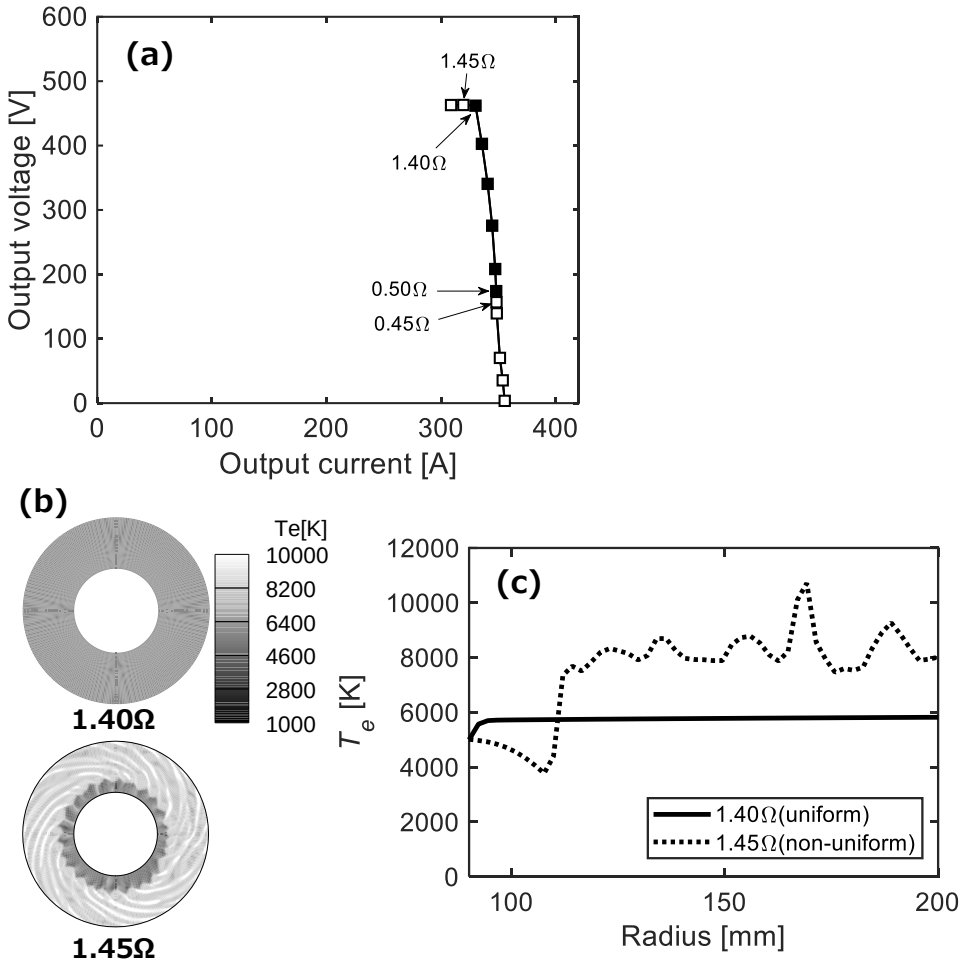

Fig. 2.12 (a) Output voltage-current characteristics, (b) plasma structure, and (c) radial distribution of electron temperature at $\theta = 0$ rad in Ar/Cs under the assumption that the tree-body recombination of Ar is the same as that of Cs.

On the other hand, for Ar/Xe, the electron temperature in the generator channel at an optimum load resistance of 2.00 Ω at which the uniform plasma is achieved is approximately 6400 – 6800 K [Fig. 2.7 and Fig. 2.11(a)]. At this electron temperature region, the plasm would become unstable as predicted by the linear perturbation theory. This indicates that stability of Xe-seeded noble gas plasma probably cannot be explained by the linear perturbation theory.

Here, the characteristic time of electron number density is compared with the residence time of the working gas. It should be noted that the characteristic time of the electron number density in the noble gas plasma can be longer than that in the alkali metal-seeded plasma because of the noble gas's lower three-body recombination coefficient compared with alkali metal [6], [24]–[26]. The characteristic time of the electron number density can be expressed roughly as

$$\tau \equiv \frac{n_e}{|\dot{n}_e|} \tag{2.39}$$

where $n_e = n_{\mathrm{Ar}}^+ + n_{\mathrm{Xe}}^+$ and $\dot{n}_e = \dot{n}_{\mathrm{Ar}}^+ + \dot{n}_{\mathrm{Xe}}^+$.

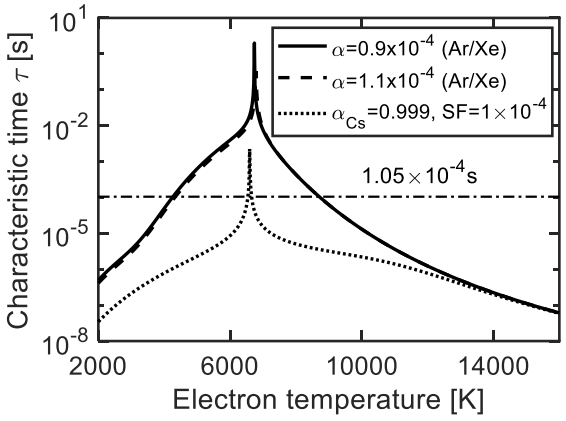

Fig. 2.13 Characteristic time of electron number density under Ar/Xe (solid and dashed lines) and Ar/Cs (dotted line). The horizontal dashed-dotted line depicts the residence time of the working gas.

Fig. 2.13 shows the characteristic time of electron number density against the electron temperature under Ar/Xe. The characteristic time for Ar/Cs is also included for comparison. The characteristic times for Ar/Xe are calculated at a minimum and maximum ionization degrees in the generator channel under an optimum load resistance of 2.00 Ω. For Ar/Cs, the characteristic time is calculated at a seed fraction of 1.0×10^{-4}, ionization degree of Cs of 0.999. The dashed-dotted line in the figure depicts the residence time (= the generator channel length/the velocity u_r) of the working gas (~0.1 ms). As can be seen in the figure, the characteristic time in Ar/Cs is shorter than the residence time of the working gas in almost all the electron temperatures. In Ar/Xe, on the other hand, in the electron temperature region of approximately 4300 – 8600 K, the characteristic time becomes longer than the residence time. Under this condition, the variation of electron number density during the period when the working gas passes through the generator channel is small, and a uniform plasma can be maintained. It should be noted that the plasma in the generator might be inherently unstable (according to linear perturbation theory), but under a long characteristic time, before the nonuniform plasma that is originated from that instability appears, the working gas has already exited the generator channel. In other word, the nonuniform plasma does not appear before the working gas exits the generator channel. As shown in Fig. 2.11(a), at the lower limit 1.20 Ω and upper limit 2.00 Ω of load resistances where the uniform plasmas are achieved, the electron temperatures in the generator channel are approximately 4300 – 6800 K and 6400 – 6800 K, respectively. In this electron temperature region, the characteristic

time is longer than the residence time, thus the uniform plasma in maintained. On the other hand, at lower load resistance of 1.10 Ω the electron temperature decreases, and at higher load resistance of 2.10 Ω the electron temperature increases (above 10000 K). In any case the characteristic time becomes shorter than the residence time, as a result the nonuniform plasma structure originating from the development of ionization instability in Xe-seeded noble gas plasma appears.

Based on the above discussion, for Ar/Xe to keep the electron temperature above 4300 K inside the generator channel, it requires higher load resistance compared with Ar/Cs due to the higher ionization potential of Xe than Cs; consequently, as shown in Fig. 2.4 the range of load resistance for achieving uniform plasma becomes narrower than that in Ar/Cs. It has been confirmed that the range of electron temperature for maintaining uniform plasma as stated above does not change significantly under a typical operating condition (such as Mach number and inlet ionization degree) of MHD generator.

2.4 Effect of xenon seed on plasma behavior and power generation characteristics

In this section, the effect that Xe seeding has on plasma behavior and power generation characteristics is examined.

2.4.1 Numerical conditions

The numerical conditions are shown in Table 2.3. The working gas is Ne/Xe with seed fractions (*S.F.*, mole% of Xe in the mixture) of 0.0% (pure Ne), 0.1%, 1.0%, 5.0%, 10.0%, 50.0%, and 100.0% (pure Xe). The numerical simulations are conducted under a total pressure of 0.30 MPa, total temperature of 2500 K, Mach number of 1.49, and magnetic flux density of 4.0 T. The applied magnetic flux density is assumed to hold in the z-direction only and to be constant throughout the generator. Here, the pre-ionization power (*P.P.*) is defined as the net power used for plasma production (in the physical meaning, it is the electron thermal input), and the pre-ionization power ratio (*P.P.R.*) is defined as the ratio of the pre-ionization power (*P.P.*) to the thermal input (Q_{in}) of heavy particles and electrons. Each equation is expressed as follows.

$$Q_{in} = \left[\rho_g \left(c_\nu T_g + \frac{1}{2}|\vec{u}|^2\right) + p_g\right] u_r A_{in} + P.P. \tag{2.40}$$

$$P.P. = \left(\frac{3}{2} n_e k_B T_e + \sum_i \epsilon_i n_i + p_e\right) u_r A_{in} \tag{2.41}$$

$$P.P.R. = \frac{P.P.}{Q_{in}} \tag{2.42}$$

Here, A_{in} is the cross-sectional area at the generator inlet. It should be noted here that *P.P.* is not the radio frequency (RF) input power which is the actual power flowing into the RF induction coil for ionization.

Table 2.3 Numerical conditions

Working gas		Ne/Xe
Seed fraction	[%]	0.0, 0.1, 1.0, 5.0, 10.0, 100.0
Total pressure	[MPa]	0.30
Total temperature	[K]	2500
Mach number	[–]	1.49
Magnetic flux density	[T]	4.0
Load resistance	[Ω]	0.01 – 2.0

2.4.2 Power generation characteristics

Table 2.4 shows the working conditions examined here, such as the thermal input (Q_{in}), the inlet electron temperature, and the inlet electron number density at each seed fraction. It should be noted here that the inlet electron temperature and the number density are chosen so as to obtain a pre-ionization ratio *P.P.R.* of 1.00%, regardless of the seed fraction. Fig. 2.14 shows the output voltage-current characteristics under various seed fractions (*S.F.*). For any seed fraction, the current decreases slightly and the voltage increases greatly as the load resistance increases (i.e., the output power increases). In general, as the load resistance increases, the electron temperature also increases due to the increase in Joule heating, resulting in an increase in electrical conductivity and output power. However, when the load resistance is excessively high, the output current largely drops, and in some cases, the output voltage saturates or drops abruptly (i.e., the output power decreases). Namely, there is optimal load resistance for providing maximum output power.

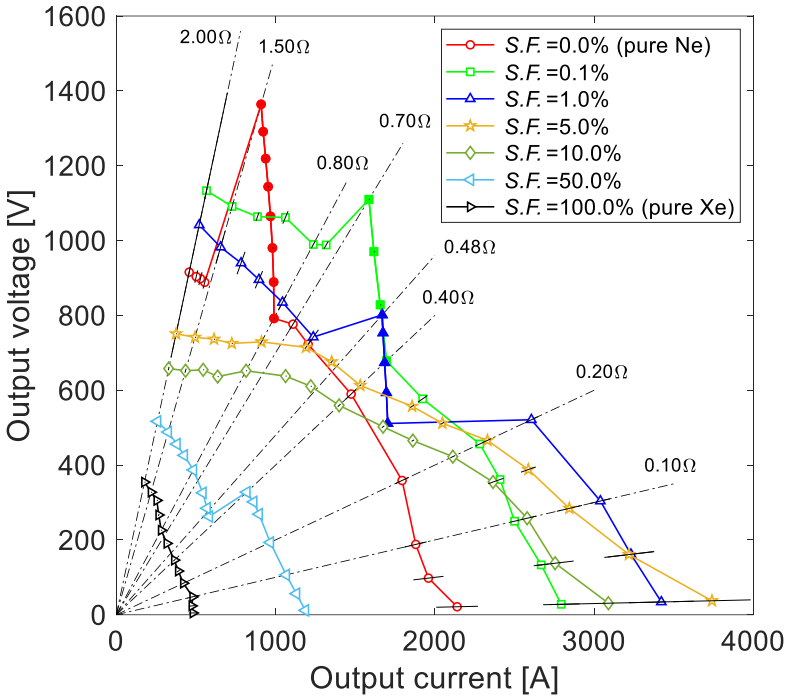

Fig. 2.14 Output voltage-current characteristics under various seed fractions (*S.F.*). The uniform plasma appears at the closed point.

Table 2.4 Working conditions and power output at optimal load resistance

Seed fraction [%]	0.0 (pure Ne)	0.10	1.00	5.00	10.0	50.0	100.0 (pure Xe)
Thermal input [MW]	2.81	2.80	2.73	2.48	2.25	1.45	1.10
Inlet electron temperature [K]	9650	8480	7370	6830	6620	6190	6015
Inlet electron number density [m^{-3}]	8.74×10^{20}	1.48×10^{21}	1.50×10^{21}	1.52×10^{21}	1.52×10^{21}	1.54×10^{21}	1.54×10^{21}
Optimal Load resistance [Ω]	1.50	0.70	0.48	0.20	0.20	0.40	1.20
Maximum power output [MW]	1.24	1.76	1.34	1.09	0.89	0.27	0.078

The power generator performance at optimal load resistance for each seed fraction is also shown in Table 2.4. As seen in the table, at the same pre-ionization power ratio, the power output improves by adding small amounts of Xe. However, adding excessive amounts of Xe degrades

the power output. Therefore, there is an optimal seed fraction (around 0.10–1.00%) that produces high power output. At low seed fractions, the existence of Xe enhances the electrical conductivity due to its low ionization potential regardless of the same pre-ionization power ratio, resulting in higher power output. The spatial average electrical conductivities at optimum load resistance are around 320 S/m for seed fraction 0% (pure Ne), 470 S/m for seed fraction 0.1%, and 460 S/m for seed fraction 1.0%. These values can be of the same order as the electrical conductivity of cesium-seeded argon (Ar/Cs) plasma, and several ten times higher than that in the combustion gas plasma MHD power generation [6]. On the other hand, at excessively high seed fractions, the Hall parameter decreases with increasing seed fraction due to the large collision cross section of Xe atoms with electrons, and the flow velocity also decreases due to the large atomic weight of Xe. Thus, the power output decreases, which is also strongly related to the plasma behavior in the generator as will be clarified next.

2.4.3 Plasma behavior

Fig. 2.15 shows the electron temperature distribution under various seed fractions at representative load resistances. From the left-hand side, we have low, appropriate, and high load resistances. Here, the load resistance that gives high output power is regarded as the appropriate load resistance. As shown in the figure, at the appropriate load resistance, the plasma structure is uniform for low seed fractions. However, the plasma becomes nonuniform with the spiral structure for excessively high seed fractions (over 5.0%). This nonuniform spiral plasma structure is similar to the plasma at low load resistance. This suggests that adding excessive amounts of Xe can reduce the uniformity of the plasma structure in the generator. At low load resistance (low output power), the electron temperature is comparatively low in the generator due to there being inadequate Joule heating, and the nonuniform spiral plasma structure rotates counterclockwise (except for pure Xe which rotates clockwise). At high load resistance (low output power), the nonuniform spiral plasma structure rotating clockwise occurs for all seed fractions. In the spiral structure, the electron temperature increases significantly due to there being excessively high Joule heating. It should be noted here that the rotation manner of nonuniform plasma structure mentioned above is attributed to the flow downward with the gas (heavy particle).

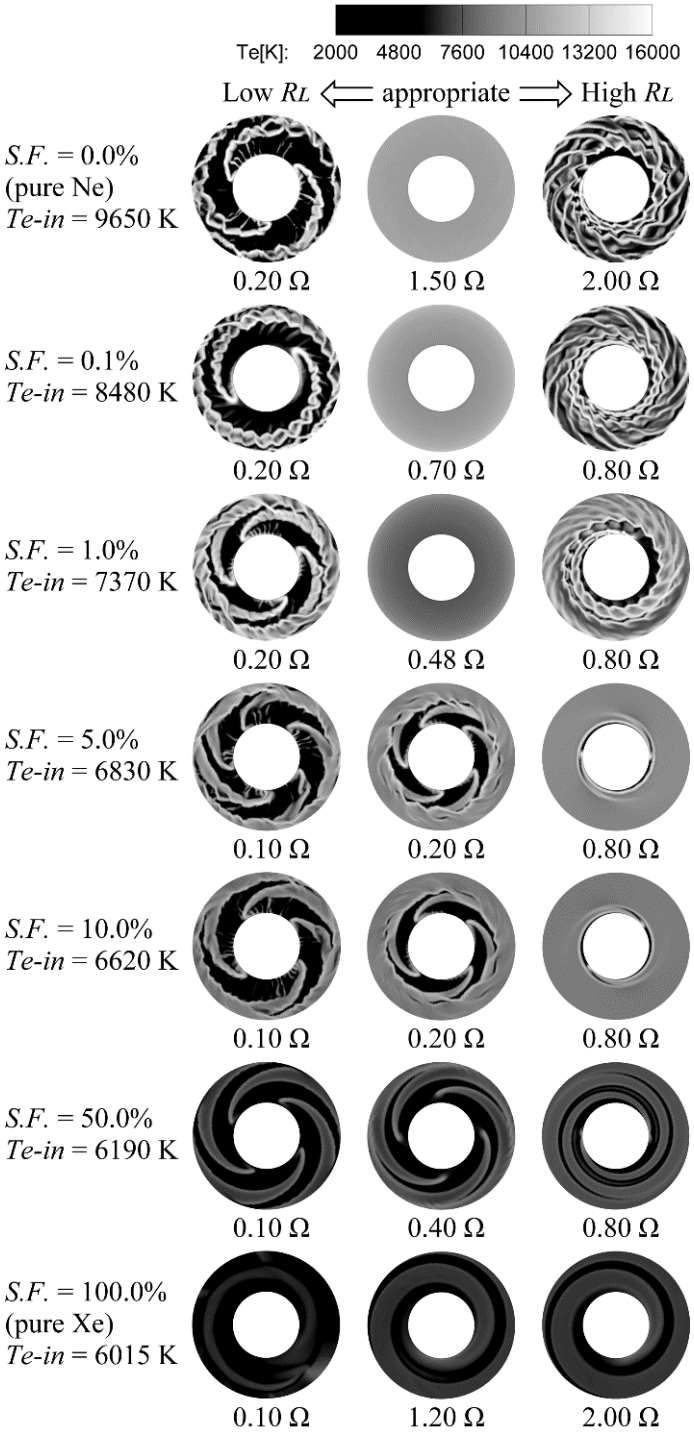

Fig. 2.15 Electron temperature distribution under various seed fractions (*S.F.*) at representative load resistances.

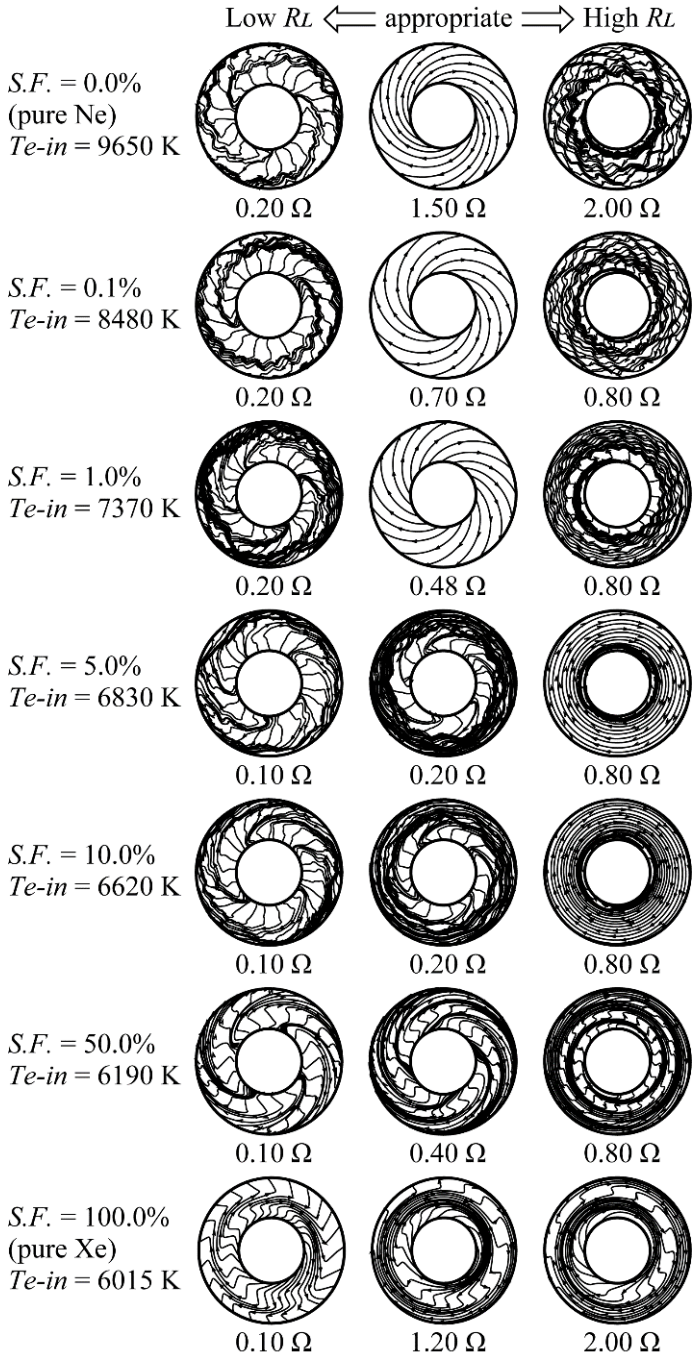

Fig. 2.16 Current streamline under various seed fractions (*S.F.*) at representative load resistances.

Fig. 2.16 shows the current streamline under various seed fractions at representative load resistances. The current streamline was taken at the same instant as the electron temperature distribution in Fig. 2.15. By neglecting the electron pressure gradient in Eq. (2.13), the current density can be written as

$$j_r = \frac{\sigma}{1+\beta^2}\left\{-\frac{\partial\phi}{\partial r} + \beta\left(\frac{1}{r}\frac{\partial\phi}{\partial\theta} + u_r B\right)\right\} \tag{2.42}$$

$$j_\theta = \frac{\sigma}{1+\beta^2}\left\{-\beta\frac{\partial\phi}{\partial r} - \left(\frac{1}{r}\frac{\partial\phi}{\partial\theta} + u_r B\right)\right\} \tag{2.43}$$

where j_r is the Hall current density (radial current density) and j_θ is the Faraday current density (circumferential current density). At an appropriate load resistance with a low seed fraction, j_r is positive and j_θ is negative throughout the generator due to the large enough Hall electromotive force $\beta u_r B$ and the positive value of $\partial\phi/\partial r$. The streamline spacing becomes uniform in the entirety of the generator, which identifies that the plasma is uniform. At an excessive seed fraction (over 5.0%), the current streamline becomes clustered, meaning that the streamline spacing is narrow in the high electron temperature region, indicating that the plasma structure is not uniform. For any seed fraction, at low load resistance j_r is positive almost in the entirety of the generator, whereas j_θ changes from positive in the low electron temperature region to negative in the high electron temperature region, and a nonuniform spiral plasma structure occurs. The plasma structure is similar to that in the case of an appropriate load resistance of an excessive seed fraction. At high load resistance, the streamline is clustered in the spiral structure where the electron temperature is extremely high. The high electron temperature causes the Hall parameter to decrease, the Hall electromotive force to become smaller than $\partial\phi/\partial r$, and j_r to become negative, as seen in Eq. (2.42). Since both j_r and j_θ are negative within the spiral structure, the current flows backward upstream. It should be noted that for a low load resistance, j_r in the spiral region is positive because of the high Hall parameter resulting from the low electron temperature in that region, which is the opposite of what occurs in the case of high load resistance. The current streamline matches well with the electron temperature distribution.

The plasma behavior can depend on the magnetic flux density strongly. However, in the present work, since we only focused on the effect of Xe seed fraction on plasma behavior, the magnetic flux density is fixed.

2.4.4 Uniformity and ionization instability in Ne/Xe plasma

As discussed in the preceding section, in Xe-seeded noble gas plasma, the ionization instability is not always caused by the partial ionization of the seed. As can be seen in Fig. 2.15, the plasma structure is uniform at a seed fraction of 0.1% and load resistance of 0.70 Ω. Then, as shown in Fig. 2.17, the ionization degree of Xe is on the order of 10^{-1} (the ionization degree of

Ne: $10^{-6} - 10^{-5}$). This indicates that the plasma structure remains uniform in the Ne/Xe plasma, even when the seed is partially ionized, which is contrary to what occurs in the alkali metal-seeded plasma.

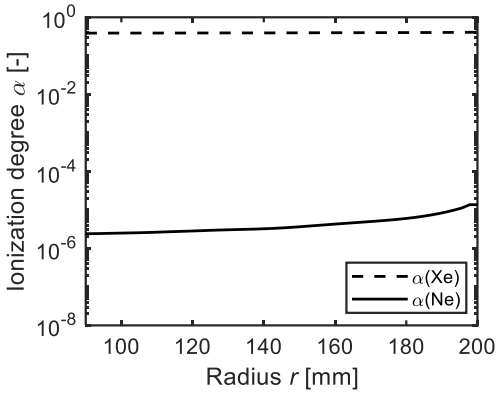

Fig. 2.17 Ionization degree of Xe seed (dashed line) and mother gas Ne (solid line) under uniform plasma structure (*S.F.* = 0.1%, R_L = 0.70 Ω).

As also stated in subsection 2.3.4, so far, the plasma stability in MHD generator has been studied using linear perturbation theory, and it is stated that plasma becomes stable when the critical Hall parameter β_{crit} exceeds the Hall parameter β [35]. The Hall parameter and critical Hall parameter are calculated for the Ne/Xe plasma as a function of the electron temperature under various seed fractions, the results of which are given in Fig. 2.18. The result of Ar/Cs plasma is also included for comparison. The critical Hall parameter in Ne/Xe is smaller than the Hall parameter when the electron temperature $T_e \leq 12500$ K for seed fractions of 0.0% (pure Ne) and 0.1%, $T_e \leq 10500$ K for 1.0%, $T_e \leq 9000$ K for 5.0%, $T_e \leq 8500$ K for 10.0%, $T_e \leq 7500$ K for 50.0%, and $T_e \leq 7000$ K for 100% (pure Xe). However, as shown in Fig. 2.15, at the appropriate load resistance at which the plasma is uniform, the electron temperature in the generator roughly varies in the range of 5000–12000 K for seed fractions of 0.0% (pure Ne), 0.1%, and 1.0%. According to liner perturbation theory, the plasma would not be uniform in those conditions. Therefore, linear perturbation theory may not hold for the plasma in the Ne/Xe gas mixture. For Ar/Cs plasma, on the other hand, there is a specific range of electron temperature (around 4000–6000 K) at which the critical Hall parameter is larger than the Hall parameter, and the plasma is stable.

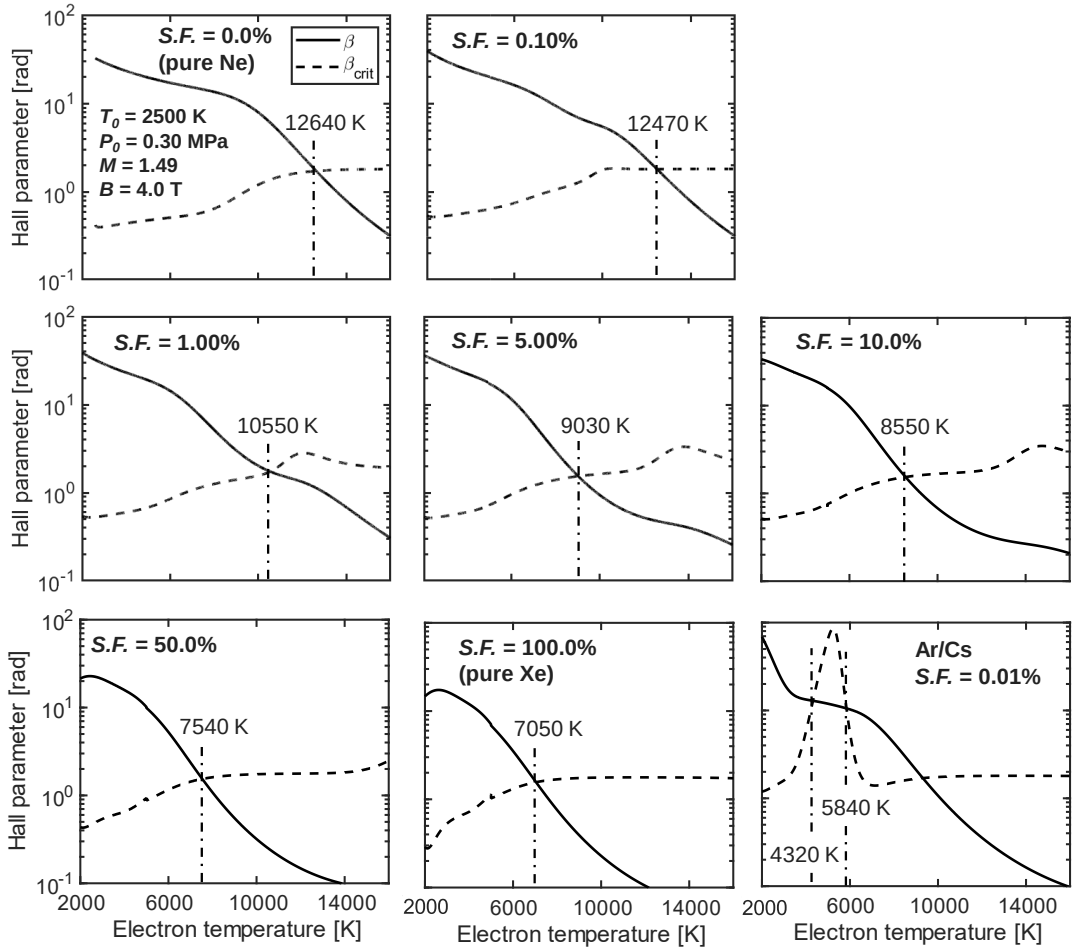

Fig. 2 18 Hall parameter (solid line) and critical Hall parameter (dashed line) as a function of the electron temperature under various seed fractions in Ne/Xe plasma and under Ar/Cs plasma.

Here, the characteristic time of the variation in the electron number density [Eq. (2.39)] is compared with the residence time of the working gas. Fig. 2.19 shows the characteristic time of the electron number density as a function of the electron temperature under Ne/Xe at various seed fractions. The characteristic time is calculated at two different values of ionization degree, the minimal and maximal values in the generator at the optimal load resistance of each seed fraction. The dashed-dotted line in the figure depicts the residence time of the working gas (= the generator channel length/the velocity u_r). It can be seen from these figures that the characteristic time is longer than the residence time when the electron temperature is maintained in the ranges of approximately 4000–14000 K for seed fractions 0.0% (pure Ne) and 0.1%, 5000–11000 K for 1.0%, 5000–9000 K for 5.0%, 5000–8000 K for 10.0%, and 5000–7000 K for 50.0% and 100% (pure Xe). The range of the electron temperature becomes narrower as the seed fraction increases. This can be attributed to the low ionization potential of Xe and its large atomic weight. Since the ionization potential of Xe is low, the net production rate of electron $\dot{n}_e$ increases easily, and

since the atomic weight is large, the velocity of the working gas decreases with increasing seed fraction, resulting in a long residence time.

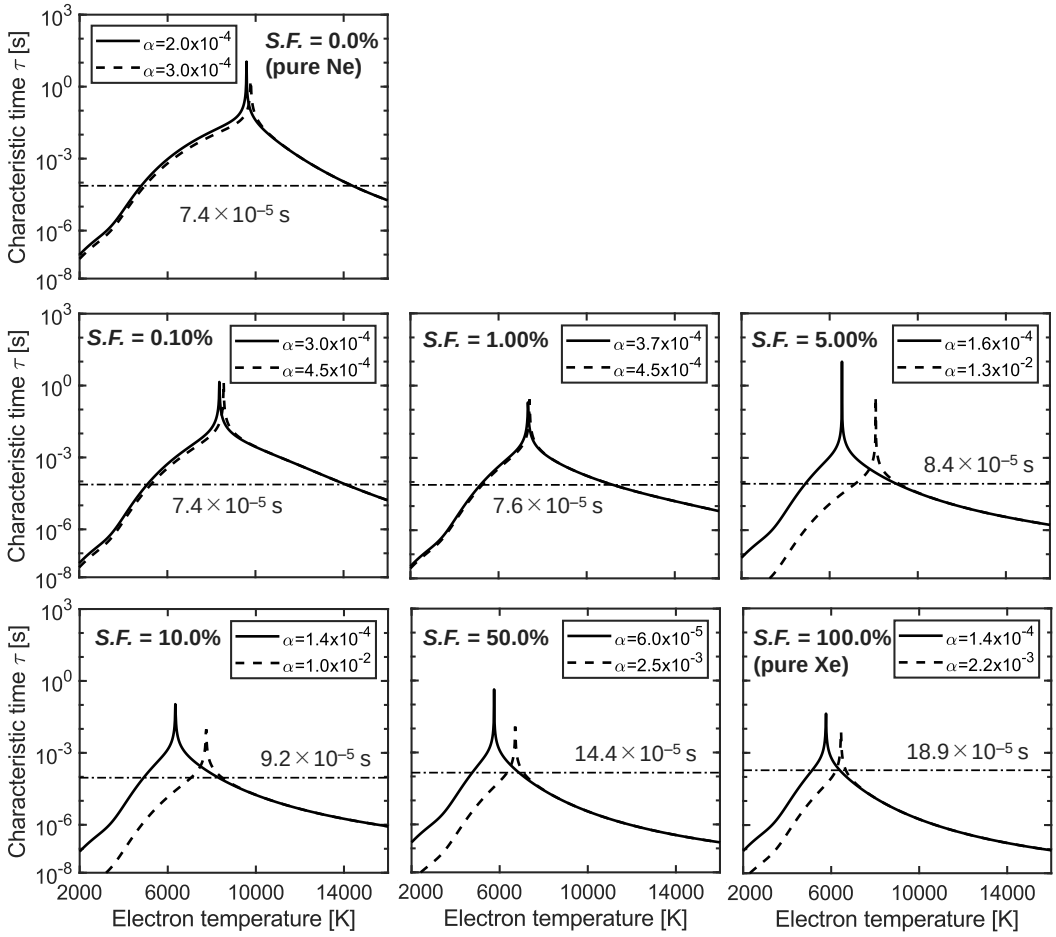

Fig. 2.19 Characteristic time of the electron number density as a function of the electron temperature under various seed fractions. The characteristic time is calculated at two different values of ionization degree, the minimal and maximal values in the generator at the optimal load resistance of each seed fraction. The dash dotted line depicts the residence time of the working gas. In the region at which the characteristic time is longer than the residence time, the uniform plasma is maintained.

The fact that the characteristic time is longer than the residence time means that the variation of the electron number density is small during the period when the working gas passes through the generator channel. To maintain uniform plasma, the variation of the electron number density in response to the electron temperature must be kept small. Originally, the plasma in the generator channel might be unstable as predicted by linear perturbation theory. However, under a long characteristic time, the unstable behavior does not appear before the working gas exits the channel.

Consequently, the uniform plasma is maintained. Moreover, as shown in Fig. 2.15, the electron temperature decreases at low load resistance and increases at high load resistance. In any case, the electron temperature in the generator is locally out of the above range, causing the characteristic time to become shorter than the residence time. Under this condition, a nonuniform plasma structure appears originating from the development of ionization instability.

2.5 Summary of chapter 2

In this chapter, the plasma behavior and power generation characteristics in a Xe-seeded noble gas plasma MHD generator were examined by r-θ 2-D numerical simulation under the assumptions of isentropic gas flow and a non-MHD interaction in order to focus on the inherent characteristics of the plasma. The following conclusions can be drawn.

(1) For both Xe-seeded noble gas plasma (Ar/Xe) and alkali metal seeded plasma (Ar/Cs), at the optimum load resistance, uniform plasma is produced and maintained in the generator channel, and the power outputs are the same under an identical inlet ionization degree.

(2) In alkali metal seeded plasma, plasma is stable and uniform when the critical Hall parameter exceeds the Hall parameter generally based on the linear perturbation theory, whereas in Xe-seeded noble gas plasma, uniform plasma is maintained when the characteristic time of electron number density is longer than the residence time of the working gas even under the electron temperature condition at which the unstable plasma is suggested from the linear perturbation theory.

(3) Adding a small amount of Xe to Ne improves power output due to the resulting enhancement of electrical conductivity, even if the pre-ionization power ratio is the same. However, adding an excessive amount (over 5.0%) deteriorates the power output. At an appropriate load resistance, uniform plasma structure occurs for low seed fractions. However, the plasma structure becomes nonuniform for excessively high seed fractions (over 5.0%). This result suggests that adding an excessive amount of Xe reduces the uniformity of the plasma structure in the generator and causes a deterioration in generator performance.

(4) The range of electron temperatures for maintaining uniform plasma, where the characteristic time of the electron number density is longer than the residence time of the working gas, becomes narrower as the seed fraction increases. This is attributed to the low ionization potential of Xe and its large atomic weight.

In this chapter, the power generation characteristics in Xe-seeded noble gas plasma was examined without taking the MHD interaction into account, whereas in the actual MHD plasma

phenomena the MHD interaction occurs, and each property of the fluid is easily affected by the Lorentz force. The power generator performance in Xe-seeded plasma will be discussed in details in chapter 3 by taking the MHD interaction into account.

Chapter 3 Effect of Xenon Seed on Performance of Noble Gas Plasma MHD Power Generator

3.1 Introduction and objectives

In the preceding chapter, the power generation characteristics in a disk-shaped MHD generator with Xe-seeded noble gas plasma was examined under the assumptions of in isentropic flow and a non-MHD interaction. In actual MHD plasma phenomena, however, the MHD interaction, an interaction between a conducting fluid and a magnetic field, occurs, and each property of the fluid is easily affected by the Lorentz force.

In this chapter, the performance of a disk-shaped MHD generator with Xe-seeded Ar (Ar/Xe), Xe-seeded Ne (Ne/Xe), and Xe-seeded He (Ne/Xe) working gases is examined by taking the MHD interaction into account using r-z two-dimensional numerical simulation. The seed fraction (mole percent of Xe in the mixture) is varied from 0.0% (pure mother gas) to 100.0% (pure Xe) to assess the effect that Xe seeding has on the generator performance. It should be noted that although r-z simulation can evaluate the performance including the effects of the boundary layer near the walls, it cannot include the nonuniformity of plasma. Thus, in addition to r-z numerical simulation, r-θ numerical simulation is carried out and compared with the results obtained from r-z simulation in order to evaluate the generator performance more precisely including the effects of the boundary layer and plasma uniformity.

3.2 Governing equations and numerical procedures

3.2.1 Governing equations

In the present numerical study, the non-equilibrium plasma fluid flow is described by the two-temperature model MHD equations (equations for all-particle system and charged particles system), Maxwell equation and equation of state [6]. The following equations are adopted from [6]. The "pressure loss due to the wall friction $\vec{P}_{LOSS}$" term in momentum equation and "heat loss through the wall Q_{LOSS}" term in energy equation are adopted only for r-θ numerical simulation.

a) Equations for All-particle (MHD Plasma Flows)

i) Continuity equation

$$\frac{\partial \rho}{\partial t} + \nabla \cdot (\rho \vec{u}) = 0 \tag{3.1}$$

ii) Momentum equation

$$\frac{\partial \rho \vec{u}}{\partial t} + \nabla \cdot (\rho \vec{u}\vec{u}) = -\nabla p + \nabla \cdot \boldsymbol{\tau} + \vec{j} \times \vec{B} - \vec{P}_{LOSS} \tag{3.2}$$

iii) Energy equation

$$\begin{aligned} \frac{\partial E_s}{\partial t} + \nabla \cdot [(E_s + p)\vec{u}] = \vec{j} \cdot \vec{E} + \nabla \cdot (\boldsymbol{\tau} \cdot \vec{u}) - \nabla \cdot \vec{q}_g \\ + \vec{u} \cdot \nabla p_e - \nabla \cdot \vec{q}_e - \vec{u} \cdot \vec{P}_{LOSS} - Q_{LOSS} \end{aligned} \tag{3.3}$$

iv) Total mass density

$$\rho = \rho_g + \rho_e = \sum_h m_h n_h + m_e n_e \tag{3.4}$$

v) Equation of state

$$p = p_g + p_e = \sum_h n_h k_B T_g + n_e k_B T_e \tag{3.5}$$

vi) Total energy density

$$E_s = \rho_g \left(c_v T_g + \frac{1}{2} |\vec{u}|^2 \right) + U_e \tag{3.6}$$

Here, $\vec{B}$ is the magnetic flux density, c_v the specific heat at constant volume, $\vec{E}$ the electric field, E_s the total energy density, $\vec{j}$ the current density, k_B the Boltzmann constant, m the mass of particle, n the particle number density, $\vec{P}_{LOSS}$ the pressure loss due to the wall friction, p the pressure, Q_{LOSS} the heat loss through the wall, $\vec{q}$ the heat flux, T the temperature, $\vec{u}$ the velocity, U_e the electron energy density [see Eq. (3.39)], ρ the mass density, $\boldsymbol{\tau}$ the stress tensor, the subscripts: g is the heavy particle, e the electron and h the heavy particle species (ion, metastable atom, neutral atom of mother gas, ion and neutral atom of seed material).

The stress tensor [Eq. (3.7)] is calculated using Newton's las of viscosity.

$$\boldsymbol{\tau} = \mu \left(\frac{\partial u_i}{\partial x_j} + \frac{\partial u_j}{\partial x_i} \right) - \frac{2}{3} \mu (\nabla \cdot \vec{u}) \delta \tag{3.7}$$

Here, δ is the Kronecker delta ($\delta = 1$ for $i = j$ and $\delta = 0$ for $i \neq j$), μ the viscosity coefficient.

Viscosity coefficient

The viscosity coefficient μ [Pa·s] is the sum of the molecular viscosity μ_m [Pa·s] and the eddy viscosity μ_t [Pa·s]. Note that for r-θ simulation, only molecular viscosity μ_m is taken into account because we cannot evaluate the eddy viscosity μ_t.

$$\mu = \mu_m + \mu_t \tag{3.8}$$

- **Molecular viscosity**: the molecular viscosity μ_m is calculated using Sutherland's formular [37], [38].

$$\mu_m = \mu_0 \frac{T_s + S}{T_g + S} \left(\frac{T_g}{T_s}\right)^{\frac{3}{2}} \tag{3.9}$$

Here, S [K] is the Sutherland constant, μ_0 the reference viscosity coefficient at a reference temperature of $T_s =$ 298.15 [K]. The Sutherland constant and the reference viscosity coefficient for various noble gases are given in Table 3.1.

Table 3.1 Sutherland constant [38] and viscosity coefficient [39] of various noble gases at a reference temperature of 298.15 [K].

Gas species	Xe	Ar	Ne	He
S [K]	252	148	64.1	72.9
μ_0 [$\times 10^{-7}$ Pa·s][a]	230.8	226.1	317.5	198.5

[a] 1 μP (micro poise) = 10^{-7} Pa·s

- **Eddy viscosity**: the eddy viscosity μ_t is calculated using Baldwin-Lomax model, an algebraic turbulence model proposed by B. S. Baldwin and H. Lomax [40], [41]. In this model, the eddy viscosity is given as follows.

$$\mu_t = \begin{cases} \mu_{t\text{inner}} \; if \; y \leq y^* \\ \mu_{t\text{outer}} \; if \; y > y^* \end{cases} \tag{3.10}$$

Here, $\mu_{t\text{inner}}$ and $\mu_{t\text{outer}}$ denote the eddy viscosities in the inner and outer regions, respectively. y is the normal distance from the wall and y^* is the smallest value of at which values from the inner and outer formulars are equal (i.e., $\mu_{t\text{inner}} = \mu_{t\text{outer}}$).

The eddy viscosity in the inner region μ_{tinner} is given by the Prandtl-Van Driest formulation

$$\mu_{\mathrm{tinner}} = \rho \ell^2 |\omega| \tag{3.11}$$

where

$$\ell = ky\left[1 - \exp\left(-\frac{y^+}{A^+}\right)\right] \tag{3.12}$$

and

$$y^+ = \frac{\sqrt{\rho_w \tau_w} \cdot y}{\mu_w} \tag{3.13}$$

Here, $|\omega|$ is the magnitude of the vorticity, μ_w the viscosity at the wall, ρ_w the fluid density at the wall and the τ_w the shear stress at the wall (the wall shear stress).

The eddy viscosity in the outer region μ_{touter} is given by

$$\mu_{\mathrm{touter}} = KC_{cp}\rho F_{wake} F_{Klerb}(y) \tag{3.14}$$

where K is the Clauser constant, C_{cp} is an additional constant, and

$$F_{wake} = \min\left(y_{max}F_{max}, C_{wk}y_{max}\frac{u_{dif}^2}{F_{max}}\right) \tag{3.15}$$

The quantity F_{max} is the maximum value of

$$F(y) = y|\omega|\left[1 - \exp\left(-\frac{y^+}{A^+}\right)\right] \tag{3.16}$$

and the quantity y_{max} is the value of y at which F_{max} occurs.

u_{dif} is the difference between maximum and minimum total velocity. For boundary layers the minimum is always set to zero.

$$u_{dif} = \max(|u|) - \min(|u|) \tag{3.17}$$

The function $F_{Klerb}(y)$ is the Klebanoff intermittency factor given by

$$F_{Klerb}(y) = \left[1 + 5.5\left(\frac{C_{Kleb} \cdot y}{y_{max}}\right)^6\right]^{-1} \tag{3.18}$$

The constants appearing in the above equations are as follows.

$$A^+ = 26, \qquad C_{cp} = 1.6, \qquad C_{Kleb} = 0.3, \qquad k = 0.4, \qquad K = 0.0168$$

Pressure loss due to the wall friction and heat loss through the wall

The pressure loss due to the wall friction $\vec{P}_{LOSS}$ [2] and heat loss through the wall Q_{LOSS} [2] are defined as follows.

$$\vec{P}_{LOSS} = \frac{1}{2}\rho|\vec{u}|C_f \cdot \frac{4\pi r}{A}\vec{u} \tag{3.19}$$

$$Q_{LOSS} = S_t \rho|\vec{u}|c_p(T_{aw} - T_w) \tag{3.20}$$

where local skin friction coefficient C_f [42], [43], Stanton number S_t [44], and adiabatic wall temperature T_{aw} [42] are expressed by

$$C_f = \frac{0.040 \cdot Re_h^{-0.2}}{\left(1 + \frac{\gamma - 1}{2} \cdot M^2\right)^{0.467}} \tag{3.21}$$

$$S_t = \frac{1}{2} C_f Pr^{-\frac{2}{3}} \tag{3.22}$$

$$T_{aw} = \left(1 + f_r \frac{\gamma - 1}{2} \cdot M^2\right) \cdot T_g \tag{3.23}$$

Here, A is the cross-sectional area, c_p the specific heat at constant pressure, f_r the recovery factor ($= Pr^{1/3}$ [42]), M the Mach number, Pr the Prandtl number (around 0.7 for most gases), Re_h the Reynold number, r the radius, T_w the wall temperature, γ the specific heat ratio.

As stated above, the $\vec{P}_{LOSS}$ term in momentum equation and $\vec{u} \cdot \vec{P}_{LOSS}$ and Q_{LOSS} terms in energy equation are adopted only for r-θ numerical simulation because we cannot evaluate the viscous stress owing to velocity gradient and the wall heat flux owing to temperature gradient in z-direction. For r-z numerical simulation, the algebraic turbulence model proposed by Baldwin and Lomax as described above is adopted.

Heat fluxes of gas and electron

The heat fluxes of gas (heavy particle) $\vec{q}_g$ and electron $\vec{q}_e$ [Eq. (3.24)] are calculated using Fourier's law of heat conduction [6], [45].

$$\vec{q}_g = -\kappa_g \nabla T_g, \qquad \vec{q}_e = -\kappa_e \nabla T_e \tag{3.24}$$

where the heavy particle thermal conductivity κ_g [W/(m·K)] and electron thermal conductivity κ_g [W/(m·K)] [6] are given by

$$\kappa_g = \frac{\mu}{Pr}\frac{\gamma}{\gamma - 1} R_s \tag{3.25}$$

$$\kappa_e = \frac{2.4}{1 + \frac{\nu_{ei}}{\sqrt{2} \cdot \sum_h \nu_{eh}}} \times \frac{k_B^2 n_e T_e}{m_e \cdot \sum_h \nu_{eh}} \tag{3.26}$$

Here, R_s is the gas constant in J/(K·kg), and ν_{ei} and ν_{eh} the collision frequency of electron with ion and electron with heavy particle h, respectively.

b) Equations for charged particles

i) Continuity equation for charged particles (Rate equation)

The particle species in the present plasma model consist of neutral (ground state) atoms, metastable atoms, ions of the mother gas (Ar, Ne, He: ionization potentials are 15.8 eV, 21.6 eV, 24.6 eV respectively; excitation energies are 11.5 eV, 16.6 eV, 19.8 eV respectively), neutral (ground state) atoms, ions of the seed material (Xe: ionization potential 12.1 eV), and electrons. The rate equations for ions, metastable atoms of mother gas and ions of seed are shown in Eqs. (3.26) – (3.28). As shown in Table 3.2, we considered the direct ionization, three-body recombination, excitation, de-excitation, cumulative ionization and its reverse reaction processes for the mother gas, and direct ionization, three-body recombination reaction processes for the seed material. Additionally, for Ne/Xe and He/Xe we also included the Penning ionization reaction process that occurs between metastable atom and neutral Xe atom. For Ar/Xe, on the other hand, since the Penning ionization reaction process hardly occurs due to the excitation energy of metastable Ar atom (11.5 eV) is smaller than the ionization potential of Xe (12.1 eV), in Eqs. (3.27) and (3.28) we set $k_{pen} = 0$.

$$\frac{\partial n_{\mathrm{M}}^{+}}{\partial t} + \nabla \cdot (n_{\mathrm{M}}^{+}\vec{u}) = \dot{n}_{\mathrm{M}}^{+} = k_f n_{\mathrm{M}} n_e + k_{cu} n_{\mathrm{M^m}} n_e - k_r n_{\mathrm{M}}^{+} n_e^2 - k_{rcu} n_{\mathrm{M}}^{+} n_e^2 \tag{3.26}$$

$$\frac{\partial n_{\mathrm{M^m}}}{\partial t} + \nabla \cdot (n_{\mathrm{M^m}}\vec{u}) = \dot{n}_{\mathrm{M^m}} = k_{ex} n_{\mathrm{M}} n_e + k_{rcu} n_{\mathrm{M}}^{+} n_e^2 - k_{dex} n_{\mathrm{M^m}} n_e - k_{cu} n_{\mathrm{M^m}} n_e - k_{pen} n_{\mathrm{M^m}} n_{\mathrm{S}} \tag{3.27}$$

$$\frac{\partial n_{\mathrm{S}}^{+}}{\partial t} + \nabla \cdot (n_{\mathrm{S}}^{+}\vec{u}) = \dot{n}_{\mathrm{S}}^{+} = k_f n_{\mathrm{S}} n_e + k_{pen} n_{\mathrm{M^m}} n_{\mathrm{S}} - k_r n_{\mathrm{S}}^{+} n_e^2 \tag{3.28}$$

$$n_e = n_{\mathrm{M}}^{+} + n_{\mathrm{S}}^{+} \tag{3.29}$$

Here, k_f is the direct ionization coefficient, k_r the three-body recombination coefficient, k_{ex} the excitation coefficient, k_{dex} the de-excitation coefficient, k_{cu} and k_{rcu} the cumulative ionization coefficient and its reverse reaction coefficient, and k_{pen} the Penning ionization coefficient. n_{M}, $n_{\mathrm{M^m}}$, and n_{M}^{+} are the neutral atom, metastable atom, and ion number densities of mother gas, n_{S} and n_{S}^{+} are the neutral atom and ion number densities of seed, and n_e is the electron number density. The subscripts M and S denotes the mother gas (Ar, Ne, He) and seed material (Xe), respectively. Each reaction rate coefficient is shown in Table 3.2.

In the present study, at low electron temperature region the three-body recombination coefficient (k_{rL}) by Hinnov [24] is adopted, at high electron temperature region the three-body recombination coefficient (k_{rH}) by Generalov [46], Owano [26], McIntyre [27], and Biberman [28] are adopted for Xe, Ar, Ne, and He respectively. The former and the later are connected smoothly by Eq. (3.30).

$$k_r(s) = \frac{k_{rL} \times k_{rH}(s)}{k_{rL} + k_{rH}(s)}, (s = \mathrm{Xe}, \mathrm{Ar}, \mathrm{Ne}, \mathrm{He}) \tag{3.30}$$

$$k_{rL} = 1.09 \times 10^{-20} T_e^{-\frac{9}{2}} \tag{3.31}$$

$$k_{rH}(\mathrm{Xe}) = \frac{1}{3} \times 1.21 \times 10^{-35} \times \frac{1}{T_e^2} \exp\left(\frac{55300}{T_e}\right) \tag{3.32}$$

$$k_{rH}(\mathrm{Ar}) = 3.3 \times 10^{-44} \left(\frac{135300}{T_e} + 2\right) \exp\left(\frac{47800}{T_e}\right) \tag{3.33}$$

$$k_{rH}(\mathrm{Ne}) = 2.96 \times 10^{-45} \left(\frac{192700}{T_e} + 2\right) \exp\left(\frac{58040}{T_e}\right) \tag{3.34}$$

$$k_{rH}(\mathrm{He}) = 1.21 \times 10^{-35} \times \frac{1}{T_e^2} \exp\left(\frac{55300}{T_e}\right) \tag{3.35}$$

The ionization rate coefficient k_f is derived from the detailed balance [7].

$$k_f(s) = k_r(s) \cdot 2 \frac{g_i^+}{g_i} \left(\frac{2\pi m_e k_B T_e}{\hbar^2}\right)^{\frac{3}{2}} \exp\left(-\frac{\epsilon_i}{k_B T_e}\right) \tag{3.36}$$

It should be noted here that to examine generator performance more precisely, a detailed Collisional-Radiative (C-R) model should be constructed that takes into account many excitation energy levels, and at each excitation energy level considers the collisional excitation, collisional de-excitation, de-excitation due to the radiation and energy loss due to the radiation. However, in the present study since only one excitation energy level was considered and additionally the nonequilibrium plasma treated here was assumed to be optically thick, the radiative process was not taken into account.

Table 3.2 Plasma reaction model

Gas species	Reactions	Rate coefficients[a]	Ref.
Mother gases (Ar, Ne, He)	$Ar + e^- \xrightarrow{k_f} Ar^+ + 2e^-$	Eq. (3.36)	–
	$Ar^+ + 2e^- \xrightarrow{k_r} Ar + e^-$	Eq. (3.30)	–
	$Ar + e^- \xrightarrow{k_{ex}} Ar^m + e^-$	$4.549 \times 10^{-17} T_e^{0.5} \cdot \exp\left(-\frac{135190}{T_e}\right)\ [m^3/s]$	[47]
	$Ar^m + e^- \xrightarrow{k_{dex}} Ar + e^-$	$4.456 \times 10^{-18} T_e^{0.5}$	[47]
	$Ar^m + e^- \xrightarrow{k_{cu}} Ar^+ + 2e^-$	$1.272 \times 10^{-15} T_e^{0.5} \cdot \exp\left(-\frac{47690}{T_e}\right)\ [m^3/s]$	[47]
	$Ar^+ + 2e^- \xrightarrow{k_{rcu}} Ar^m + e^-$	$-\ [m^3/s]$	[47],[7][b]
	$Ne + e^- \xrightarrow{k_f} Ne^+ + 2e^-$	Eq. (3.36)	–
	$Ne^+ + 2e^- \xrightarrow{k_r} Ne + e^-$	Eq. (3.30)	–
	$Ne + e^- \xrightarrow{k_{ex}} Ne^m + e^-$	$6.825 \times 10^{-22} T_e^{1.69} \cdot \exp\left(-\frac{192630}{T_e}\right)\ [m^3/s]$	[29]
	$Ne^m + e^- \xrightarrow{k_{dex}} Ne + e^-$	$2.0 \times 10^{-16}\ [m^3/s]$	[30]
	$Ne^m + e^- \xrightarrow{k_{cu}} Ne^+ + 2e^-$	$4.027 \times 10^{-17} T_e^{0.74} \cdot \exp\left(-\frac{58020}{T_e}\right)\ [m^3/s]$	[29]
	$Ne^+ + 2e^- \xrightarrow{k_{rcu}} Ne^m + e^-$	$-\ [m^3/s]$	[29],[7][b]
	$Ne^m + Xe \xrightarrow{k_{pen}} Ne + Xe^+ + e^-$	$7.5 \times 10^{-17}\ [m^3/s]$	[29]
	$He + e^- \xrightarrow{k_f} He^+ + 2e^-$	Eq. (3.36)	–
	$He^+ + 2e^- \xrightarrow{k_r} He + e^-$	Eq. (3.30)	–
	$He + e^- \xrightarrow{k_{ex}} He^m + e^-$	$2.31 \times 10^{-16} T_e^{0.31} \cdot \exp\left(-\frac{229770}{T_e}\right)\ [m^3/s]$	[48]
	$He^m + e^- \xrightarrow{k_{dex}} He + e^-$	$1.099 \times 10^{-17} T_e^{0.31}\ [m^3/s]$	[48]
	$He^m + e^- \xrightarrow{k_{cu}} He^+ + 2e^-$	$4.66 \times 10^{-16} T_e^{0.6} \cdot \exp\left(-\frac{55470}{T_e}\right)\ [m^3/s]$	[48]
	$He^+ + 2e^- \xrightarrow{k_{rcu}} He^m + e^-$	$-\ [m^3/s]$	[48],[7][b]
	$He^m + Xe \xrightarrow{k_{pen}} He + Xe^+ + e^-$	$1.24 \times 10^{-16}\ [m^3/s]$	[48]
Seed material (Xe)	$Xe + e^- \xrightarrow{k_f} Xe^+ + 2e^-$	Eq. (3.36)	–
	$Xe^+ + 2e^- \xrightarrow{k_r} Xe + e^-$	Eq. (3.30)	–

[a]The electron temperature T_e is in Kelvin.
[b]Reaction-rate coefficient derived from detailed balance.

ii) Generalized Ohm's law

$$\vec{j} + \frac{\beta}{|\vec{B}|}\vec{j} \times \vec{B} = \sigma\left(\vec{E} + \vec{u} \times \vec{B} + \frac{\nabla p_e}{e n_e}\right) \tag{3.37}$$

iii) Electron energy equation

$$\frac{\partial U_e}{\partial t} + \nabla \cdot [(U_e + p_e)\vec{u}] = \frac{|\vec{j}|^2}{\sigma} + \vec{u} \cdot \nabla p_e - \nabla \cdot \vec{q}_e - \frac{3}{2} k_B n_e (T_e - T_g) \sum_h \frac{2m_e}{m_h} \nu_{eh} \tag{3.38}$$

$$U_e = \frac{3}{2} n_e k_B T_e + \sum_i \epsilon_i n_i \tag{3.39}$$

Here, n_i is the number density of particle i (M^+, M^m, S^+), ϵ_i the ionization or excitation energy of particle i, β the Hall parameter, ν_{eh} the collision frequency of electron with heavy particle h, and σ the electrical conductivity.

Electrical conductivity and Hall parameter

The electrical conductivity and the Hall parameter are expressed as follows. The electrical conductivity expression in Eq. (3.40) is derived on the basic of mean-free-path arguments, and is generally accurate to within a factor of two or three in the complete range of ionization degree. For a typical plasma in MHD generator with an ionization level of $10^{-5} - 10^{-2}$, the accuracy is within 30 percent [6], [49], [50].

$$\sigma = \frac{e^2 n_e}{m_e \nu_e}, \qquad \beta = \frac{e|\vec{B}|}{m_e \nu_e} \tag{3.40}$$
$$\nu_e = \sum_h \nu_{eh} = \sum_h c_e Q_{eh} n_h$$

Here, c_e is the mean thermal velocity of the electron [Eq. (3.41)], Q_{eh} the average momentum transfer cross section of an electron with a heavy particle h. The average momentum transfer cross section of an electron with an ion Q_{ei} [Eq. (3.42)] is taken from [6] and an electron with a neutral atom Q_{en} [Eqs. (3.43)–(3.46))] is obtained by convolving the cross section listed in [31] over a Maxwellian distribution.

$$c_e = \sqrt{\frac{8 k_B T_e}{\pi m_e}} \tag{3.41}$$

$$Q_{ei} = 6\pi \times \left(\frac{e^2}{12\pi\epsilon_0 k_B T_e}\right)^2 \ln\left\{12\pi \left(\frac{\epsilon_0 k_B}{e^2}\right)^{\frac{3}{2}} \sqrt{\frac{T_e^3}{n_e}}\right\} \tag{3.42}$$

$$Q_{en}(\mathrm{Xe}) = \begin{cases} Te < 5000\ K\text{: } 1.81 \times 10^{-33} T_e^4 - 2.68 \times 10^{-29} T_e^3 + 1.51 \times 10^{-25} T_e^2 \\ \qquad -3.76 \times 10^{-22} T_e + 3.79 \times 10^{-19} \\ Te \geq 5000\ K\text{: } 4.29 \times 10^{-36} T_e^4 - 2.41 \times 10^{-31} T_e^3 + 3.96 \times 10^{-27} T_e^2 \\ \qquad -3.71 \times 10^{-24} T_e + 4.09 \times 10^{-21} \end{cases} \tag{3.43}$$

$$Q_{en}(\mathrm{Ar}) = -9.63 \times 10^{-33} T_e^3 + 2.53 \times 10^{-28} T_e^2 + 3.46 \times 10^{-24} T_e + 4.96 \times 10^{-22} \tag{3.44}$$

$$Q_{en}(\mathrm{Ne}) = 4.79 \times 10^{-33} T_e^3 - 1.91 \times 10^{-28} T_e^2 + 2.66 \times 10^{-24} T_e + 1.24 \times 10^{-20} \tag{3.45}$$

$$Q_{en}(\mathrm{He}) = 7.42 \times 10^{-33} T_e^3 - 3.12 \times 10^{-28} T_e^2 + 3.36 \times 10^{-24} T_e + 8.16 \times 10^{-20} \tag{3.46}$$

iv) Maxwell's equations

The electromagnetic field in the plasma can be described by the Maxwell equations (see chapter 2, section 2.2.1d). Under the assumptions of charge neutrality and low magnetic Reynolds number, the Maxwell's equations are reduced to as follows.

$$\nabla \times \vec{\mathrm{E}} = \vec{0}, \qquad \nabla \cdot \vec{j} = 0 \tag{3.47}$$

3.2.2 Numerical procedures

a) Scheme for hyperbolic equations

System equations for r-z simulation

The hyperbolic equations (3.1) – (3.3), (3.26) – (3.28) and (3.38) are extended into the equations in r-z plane of (r, θ, z) cylindrical coordinate system. Here, the following assumptions are adopted.

- The plasma is treated as the perfect gas.
- The applied magnetic flux density is held in z-direction only and is constant through the generator. $\vec{B} = (0, 0, B_z)$
- Each property of the plasma fluid is uniform in azimuthal (θ-) direction.

$$\frac{\partial}{\partial \theta} = 0$$

- Continuity equation

$$\frac{\partial \rho}{\partial t} + \frac{\partial (\rho u_z)}{\partial z} + \frac{\partial (\rho u_r)}{\partial r} = -\frac{\rho u_r}{r} \tag{3.48}$$

- Momentum equation

z-direction

$$\frac{\partial (\rho u_z)}{\partial t} + \frac{\partial (\rho u_z^2 + p)}{\partial z} + \frac{\partial (\rho u_r u_z)}{\partial r} = \frac{\partial \tau_{zz}}{\partial z} + \frac{\partial \tau_{rz}}{\partial r} - \frac{\rho u_r u_z}{r} + \frac{\tau_{rz}}{r} \tag{3.49}$$

r-direction

$$\frac{\partial (\rho u_r)}{\partial t} + \frac{\partial (\rho u_r u_z)}{\partial z} + \frac{\partial (\rho u_r^2 + p)}{\partial r} = \frac{\partial \tau_{zr}}{\partial z} + \frac{\partial \tau_{rr}}{\partial r} - \frac{\rho u_r^2}{r} + \frac{\rho u_\theta^2}{r} + \frac{\tau_{rr}}{r} - \frac{\tau_{\theta\theta}}{r} + j_\theta B_z \tag{3.50}$$

θ-direction

$$\frac{\partial (\rho u_\theta)}{\partial t} + \frac{\partial (\rho u_\theta u_z)}{\partial z} + \frac{\partial (\rho u_r u_\theta)}{\partial r} = \frac{\partial \tau_{z\theta}}{\partial z} + \frac{\partial \tau_{r\theta}}{\partial r} - \frac{2\rho u_r u_\theta}{r} + \frac{2\tau_{r\theta}}{r} - j_r B_z \tag{3.51}$$

- Energy equation

$$\begin{aligned}
&\frac{\partial E_s}{\partial t}+\frac{\partial[(E_s+p)u_z]}{\partial z}+\frac{\partial[(E_s+p)u_r]}{\partial r}\\
&\qquad=\frac{\partial(u_r\tau_{rz}+u_\theta\tau_{z\theta}+u_z\tau_{zz})}{\partial z}+\frac{\partial(u_r\tau_{rr}+u_\theta\tau_{r\theta}+u_z\tau_{rz})}{\partial r}-\frac{\partial(q_{gz}+q_{ez})}{\partial z}\\
&\qquad-\frac{\partial(q_{gr}+q_{er})}{\partial r}+\frac{u_r\tau_{rr}}{r}+\frac{u_\theta\tau_{\theta r}}{r}+\frac{u_z\tau_{rz}}{r}-\frac{(E_s+p)u_r}{r}-\frac{q_{gr}+q_{er}}{r}\\
&\qquad+j_rE_r+j_zE_z+\vec{u}\cdot\nabla p_e
\end{aligned}\tag{3.52}$$

- Continuity equations for charged particles (Rate equations)

$$\begin{aligned}
&\frac{\partial n_{\mathrm{M}}^+}{\partial t}+\frac{\partial(n_{\mathrm{M}}^+u_z)}{\partial z}+\frac{\partial(n_{\mathrm{M}}^+u_r)}{\partial r}=\dot{n}_{\mathrm{M}}^+-\frac{n_{\mathrm{M}}^+u_r}{r}\\
&\frac{\partial n_{\mathrm{M}^m}}{\partial t}+\frac{\partial(n_{\mathrm{M}^m}u_z)}{\partial z}+\frac{\partial(n_{\mathrm{M}^m}u_r)}{\partial r}=\dot{n}_{\mathrm{M}^m}-\frac{n_{\mathrm{M}^m}u_r}{r}\\
&\frac{\partial n_{\mathrm{S}}^+}{\partial t}+\frac{\partial(n_{\mathrm{S}}^+u_z)}{\partial z}+\frac{\partial(n_{\mathrm{S}}^+u_r)}{\partial r}=\dot{n}_{\mathrm{S}}^+-\frac{n_{\mathrm{S}}^+u_r}{r}
\end{aligned}\tag{3.53}$$

- Electron energy equation

$$\begin{aligned}
&\frac{\partial U_e}{\partial t}+\frac{\partial[(U_e+p_e)u_z]}{\partial z}+\frac{\partial[(U_e+p_e)u_r]}{\partial r}=-\frac{\partial q_{ez}}{\partial z}-\frac{\partial q_{er}}{\partial r}-\frac{(U_e+p_e)u_r}{r}\\
&\qquad+\frac{|\vec{j}|^2}{\sigma}-\frac{q_{er}}{r}+\vec{u}\cdot\nabla p_e-\frac{3}{2}k_Bn_e(T_e-T_g)\sum_h\frac{2m_e}{m_h}\nu_{eh}
\end{aligned}\tag{3.54}$$

The above equations can be written into a system of equations as follows.

$$\frac{\partial U}{\partial t}+\frac{\partial E}{\partial z}+\frac{\partial F}{\partial r}=\frac{\partial E_v}{\partial z}+\frac{\partial F_v}{\partial r}+S\tag{3.55}$$

Here,

$$U=\begin{bmatrix}\rho\\ \rho u_z\\ \rho u_r\\ \rho u_\theta\\ E_s\\ n_{\mathrm{M}}^+\\ n_{\mathrm{M}^m}\\ n_{\mathrm{S}}^+\\ U_e\end{bmatrix},E=\begin{bmatrix}\rho u_z\\ \rho u_z^2+p\\ \rho u_ru_z\\ \rho u_\theta u_z\\ (E_s+p)u_z\\ n_{\mathrm{M}}^+u_z\\ n_{\mathrm{M}^m}u_z\\ n_{\mathrm{S}}^+u_z\\ (U_e+p_e)u_z\end{bmatrix},F=\begin{bmatrix}\rho u_r\\ \rho u_ru_z\\ \rho u_r^2+p\\ \rho u_\theta u_r\\ (E_s+p)u_r\\ n_{\mathrm{M}}^+u_r\\ n_{\mathrm{M}^m}u_r\\ n_{\mathrm{S}}^+u_r\\ (U_e+p_e)u_r\end{bmatrix},$$

$$E_v = \begin{bmatrix} 0 \\ \tau_{zz} \\ \tau_{zr} \\ \tau_{z\theta} \\ u_r\tau_{zr} + u_\theta\tau_{z\theta} + u_z\tau_{zz} - q_{gz} - q_{ez} \\ 0 \\ 0 \\ 0 \\ -q_{ez} \end{bmatrix}, F_v = \begin{bmatrix} 0 \\ \tau_{rz} \\ \tau_{rr} \\ \tau_{r\theta} \\ u_r\tau_{rr} + u_\theta\tau_{r\theta} + u_z\tau_{rz} - q_{gr} - q_{er} \\ 0 \\ 0 \\ 0 \\ -q_{er} \end{bmatrix}$$

$$S = \begin{bmatrix} -\dfrac{\rho u_r}{r} \\ -\dfrac{\rho u_r u_z}{r} + \dfrac{\tau_{rz}}{r} \\ -\dfrac{\rho u_r^2}{r} + \dfrac{\rho u_\theta^2}{r} + \dfrac{\tau_{rr}}{r} - \dfrac{\tau_{\theta\theta}}{r} + j_\theta B_z \\ -\dfrac{2\rho u_r u_\theta}{r} + \dfrac{2\tau_{r\theta}}{r} - j_r B_z \\ \dfrac{u_r\tau_{rr}}{r} + \dfrac{u_\theta\tau_{\theta r}}{r} + \dfrac{u_z\tau_{rz}}{r} - \dfrac{(E_s+p)u_r}{r} - \dfrac{q_{gr}+q_{er}}{r} + j_r E_r + j_z E_z + \vec{u}\cdot\nabla p_e \\ \dot{n}_{\mathrm{M}}^{+} - \dfrac{n_{\mathrm{M}}^{+} u_r}{r} \\ \dot{n}_{\mathrm{M^m}} - \dfrac{n_{\mathrm{M^m}} u_r}{r} \\ \dot{n}_{\mathrm{S}}^{+} - \dfrac{n_{\mathrm{S}}^{+} u_r}{r} \\ -\dfrac{(U_e+p_e)u_r}{r} + \dfrac{|\vec{j}|^2}{\sigma} - \dfrac{q_{er}}{r} + \vec{u}\cdot\nabla p_e - \dfrac{3}{2}k_B n_e (T_e - T_g)\displaystyle\sum_h \frac{2m_e}{m_h}\nu_{eh} \end{bmatrix}$$

System equations for r-θ simulation

In the r-θ simulation, the equations are solved in the x-y plane of Cartesian coordinate system. The hyperbolic equations (3.1) – (3.3), (3.26) – (3.28) and (3.38) are first extended to the equations in r-θ plane of cylindrical coordinate system, and then transformed into the equations written in x-y plane of Cartesian coordinate system. Here, the following assumptions are adopted.

- The plasma is treated as the perfect gas.
- The applied magnetic flux density is held in z-direction only and is constant through the generator. $\vec{B} = (0, 0, B_z)$
- The flow velocity and current density in z- direction are neglected. $u_z = 0, j_z = 0$
- Each property of the plasma fluid is uniform in z- direction.

$$\frac{\partial}{\partial z} = 0$$

The equations are as follows.

- Continuity equation

  In r-θ plane

$$\frac{\partial \rho}{\partial t}+\frac{\partial(\rho u_r)}{\partial r}+\frac{1}{r}\frac{\partial(\rho u_\theta)}{\partial \theta}+\frac{\rho u_r}{r}=-\rho u_r\frac{1}{h_z}\frac{\partial h_z}{\partial r} \tag{3.56-1}$$

  In x-y plane

$$\frac{\partial \rho}{\partial t}+\frac{\partial(\rho u_x)}{\partial x}+\frac{\partial(\rho u_y)}{\partial y}=-\rho u_r\frac{1}{h_z}\frac{\partial h_z}{\partial r} \tag{3.56-2}$$

- Momentum equation

  In r-θ plane

$$\begin{cases}\dfrac{\partial(\rho u_r)}{\partial t}+\dfrac{\partial(\rho u_r^2)}{\partial r}+\dfrac{1}{r}\dfrac{\partial(\rho u_r u_\theta)}{\partial \theta}+\dfrac{\rho u_r^2}{r}-\dfrac{\rho u_\theta^2}{r} \\ \qquad =-\dfrac{\partial p}{\partial r}+\dfrac{1}{r}\dfrac{\partial(r\tau_{rr})}{\partial r}+\dfrac{1}{r}\dfrac{\partial \tau_{\theta r}}{\partial \theta}-\dfrac{\tau_{\theta\theta}}{r}-\rho u_r u_r\dfrac{1}{h_z}\dfrac{\partial h_z}{\partial r}+j_\theta B_z-P_{LOSS,r} \\ \dfrac{\partial(\rho u_\theta)}{\partial t}+\dfrac{\partial(\rho u_r u_\theta)}{\partial r}+\dfrac{1}{r}\dfrac{\partial(\rho u_\theta^2)}{\partial \theta}+\dfrac{2\rho u_r u_\theta}{r} \\ \qquad =-\dfrac{1}{r}\dfrac{\partial p}{\partial \theta}+\dfrac{1}{r^2}\dfrac{\partial(r^2\tau_{r\theta})}{\partial r}+\dfrac{1}{r}\dfrac{\partial \tau_{\theta\theta}}{\partial \theta}-\rho u_r u_\theta\dfrac{1}{h_z}\dfrac{\partial h_z}{\partial r}-j_r B_z-P_{LOSS,\theta}\end{cases} \tag{3.57-1}$$

  In x-y plane

$$\begin{cases}\dfrac{\partial(\rho u_x)}{\partial t}+\dfrac{\partial(\rho u_x^2)}{\partial x}+\dfrac{\partial(\rho u_x u_y)}{\partial y} \\ \qquad =-\dfrac{\partial p}{\partial x}+\dfrac{\partial \tau_{xx}}{\partial x}+\dfrac{\partial \tau_{xy}}{\partial y}+j_y B_z-\rho u_r\dfrac{1}{h_z}\dfrac{\partial h_z}{\partial r}u_x-P_{LOSS,x} \\ \dfrac{\partial(\rho u_y)}{\partial t}+\dfrac{\partial(\rho u_x u_y)}{\partial x}+\dfrac{\partial(\rho u_y^2)}{\partial y} \\ \qquad =-\dfrac{\partial p}{\partial y}+\dfrac{\partial \tau_{xy}}{\partial x}+\dfrac{\partial \tau_{yy}}{\partial y}-j_x B_z-\rho u_r\dfrac{1}{h_z}\dfrac{\partial h_z}{\partial r}u_y-P_{LOSS,y}\end{cases} \tag{3.57-2}$$

- Energy equation

  In r-θ plane

$$\begin{aligned}&\frac{\partial E_s}{\partial t}+\frac{\partial[(E_s+p)u_r]}{\partial r}+\frac{1}{r}\frac{\partial[(E_s+p)u_\theta]}{\partial \theta}+\frac{(E_s+p)u_r}{r} \\ &\qquad=\frac{\partial(u_r\tau_{rr}+u_\theta\tau_{r\theta})}{\partial r}+\frac{1}{r}\frac{\partial(u_r\tau_{\theta r}+u_\theta\tau_{\theta\theta})}{\partial z}+\frac{u_r\tau_{rr}+u_\theta\tau_{r\theta}}{r} \\ &\qquad+\frac{u_r\tau_{rr}+u_\theta\tau_{r\theta}}{h_z}\frac{\partial h_z}{\partial r}-\left(\frac{q_{gr}}{\partial r}+\frac{1}{r}\frac{q_{g\theta}}{\partial \theta}+\frac{q_{gr}}{r}+\frac{q_{gr}}{h_z}\frac{\partial h_z}{\partial r}\right) \\ &\qquad+\left(u_r\frac{\partial p_e}{\partial r}+\frac{u_\theta}{r}\frac{\partial p_e}{\partial \theta}\right)-\left(\frac{q_{er}}{\partial r}+\frac{1}{r}\frac{q_{e\theta}}{\partial \theta}+\frac{q_{er}}{r}+\frac{q_{er}}{h_z}\frac{\partial h_z}{\partial r}\right)+j_r E_r+j_z E_z \\ &\qquad-(E_s+p)u_r\frac{1}{h_z}\frac{\partial h_z}{\partial r}-(u_r P_{LOSS,r}+u_\theta P_{LOSS,\theta})-Q_{LOSS}\end{aligned} \tag{3.58-1}$$

In x-y plane

$$\frac{\partial E_s}{\partial t}+\frac{\partial[(E_s+p)u_x]}{\partial x}+\frac{\partial[(E_s+p)u_y]}{\partial y}$$
$$=\frac{\partial(u_x\tau_{xx}+u_y\tau_{xy})}{\partial x}+\frac{\partial(u_x\tau_{yx}+u_y\tau_{yy})}{\partial y}-\left(\frac{q_{gx}}{\partial x}+\frac{q_{gy}}{\partial y}\right)-\left(\frac{q_{ex}}{\partial x}+\frac{q_{ey}}{\partial y}\right)$$
$$+j_rE_r+j_zE_z+\left(u_x\frac{\partial p_e}{\partial x}+u_y\frac{\partial p_e}{\partial y}\right)+\frac{u_r\tau_{rr}+u_\theta\tau_{r\theta}}{h_z}\frac{\partial h_z}{\partial r}-\frac{q_{gr}}{h_z}\frac{\partial h_z}{\partial r}$$
$$-\frac{q_{er}}{h_z}\frac{\partial h_z}{\partial r}-(E_s+p)u_r\frac{1}{h_z}\frac{\partial h_z}{\partial r}-(u_xP_{LOSS,x}+u_yP_{LOSS,y})$$
$$-Q_{LOSS} \qquad (3.58-2)$$

- Continuity equations for charged particles (Rate equations)

In r-θ plane

$$\begin{aligned}
&\frac{\partial n_{\mathrm{M}}^+}{\partial t}+\frac{\partial(n_{\mathrm{M}}^+u_r)}{\partial r}+\frac{1}{r}\frac{\partial(n_{\mathrm{M}}^+u_\theta)}{\partial\theta}+\frac{n_{\mathrm{M}}^+u_r}{r}=\dot{n}_{\mathrm{M}}^+-\frac{n_{\mathrm{M}}^+u_r}{h_z}\frac{\partial h_z}{\partial r}\\
&\frac{\partial n_{\mathrm{M}^m}}{\partial t}+\frac{\partial(n_{\mathrm{M}^m}u_r)}{\partial r}+\frac{1}{r}\frac{\partial(n_{\mathrm{M}^m}u_\theta)}{\partial\theta}+\frac{n_{\mathrm{M}^m}u_r}{r}=\dot{n}_{\mathrm{M}^m}-\frac{n_{\mathrm{M}^m}u_r}{h_z}\frac{\partial h_z}{\partial r} \qquad (3.59-1)\\
&\frac{\partial n_{\mathrm{S}}^+}{\partial t}+\frac{\partial(n_{\mathrm{S}}^+u_r)}{\partial r}+\frac{1}{r}\frac{\partial(n_{\mathrm{S}}^+u_\theta)}{\partial\theta}+\frac{n_{\mathrm{S}}^+u_r}{r}=\dot{n}_{\mathrm{S}}^+-\frac{n_{\mathrm{S}}^+u_r}{h_z}\frac{\partial h_z}{\partial r}
\end{aligned}$$

In x-y plane

$$\begin{aligned}
&\frac{\partial n_{\mathrm{M}}^+}{\partial t}+\frac{\partial(n_{\mathrm{M}}^+u_x)}{\partial x}+\frac{\partial(n_{\mathrm{M}}^+u_y)}{\partial y}=\dot{n}_{\mathrm{M}}^+-\frac{n_{\mathrm{M}}^+u_r}{h_z}\frac{\partial h_z}{\partial r}\\
&\frac{\partial n_{\mathrm{M}^m}}{\partial t}+\frac{\partial(n_{\mathrm{M}^m}u_x)}{\partial x}+\frac{\partial(n_{\mathrm{M}^m}u_y)}{\partial y}=\dot{n}_{\mathrm{M}^m}-\frac{n_{\mathrm{M}^m}u_r}{h_z}\frac{\partial h_z}{\partial r} \qquad (3.59-2)\\
&\frac{\partial n_{\mathrm{S}}^+}{\partial t}+\frac{\partial(n_{\mathrm{S}}^+u_x)}{\partial x}+\frac{\partial(n_{\mathrm{S}}^+u_y)}{\partial y}=\dot{n}_{\mathrm{S}}^+-\frac{n_{\mathrm{S}}^+u_r}{h_z}\frac{\partial h_z}{\partial r}
\end{aligned}$$

- Electron energy equation

In r-θ plane

$$\frac{\partial U_e}{\partial t}+\frac{\partial[(U_e+p_e)u_r]}{\partial r}+\frac{1}{r}\frac{\partial[(U_e+p_e)u_\theta]}{\partial\theta}+\frac{(U_e+p_e)u_r}{r}$$
$$=-\left(\frac{\partial q_{er}}{\partial r}+\frac{1}{r}\frac{\partial q_{e\theta}}{\partial\theta}+\frac{q_{er}}{r}\right)+\frac{|\vec{j}|^2}{\sigma}+\left(u_r\frac{\partial p_e}{\partial r}+\frac{u_\theta}{r}\frac{\partial p_e}{\partial\theta}\right)$$
$$-\frac{3}{2}k_Bn_e(T_e-T_g)\sum_h\frac{2m_e}{m_h}\nu_{eh}-\frac{(U_e+p_e)u_r}{h_z}\frac{\partial h_z}{\partial r}-\frac{q_{er}}{h_z}\frac{\partial h_z}{\partial r} \qquad (3.60-1)$$

In x-y plane

$$\frac{\partial U_e}{\partial t}+\frac{\partial[(U_e+p_e)u_x]}{\partial x}+\frac{\partial[(U_e+p_e)u_y]}{\partial y}$$
$$=-\left(\frac{\partial q_{ex}}{\partial x}+\frac{\partial q_{ey}}{\partial y}\right)+\frac{|\vec{j}|^2}{\sigma}+\left(u_x\frac{\partial p_e}{\partial x}+u_y\frac{\partial p_e}{\partial y}\right)$$
$$-\frac{3}{2}k_B n_e(T_e-T_g)\sum_h\frac{2m_e}{m_h}\nu_{eh}-\frac{(U_e+p_e)u_r}{h_z}\frac{\partial h_z}{\partial r}-\frac{q_{er}}{h_z}\frac{\partial h_z}{\partial r} \quad (3.60-2)$$

- Relation between r-θ and x-y coordinates

For any vector quantity $\vec{f}$ such as velocity $\vec{u}$, current density $\vec{j}$ and so on, the following relational expression between r-θ and x-y coordinates holds true.

$$\begin{cases} f_x = f_r\cos\theta - f_\theta\sin\theta \\ f_y = f_r\sin\theta + f_\theta\cos\theta \end{cases} \quad or \quad \begin{cases} f_r = f_x\cos\theta + f_y\sin\theta \\ f_\theta = -f_x\sin\theta + f_y\cos\theta \end{cases} \quad (3.61)$$

Here, $\tan\theta = y/x$, $x = r\cos\theta$, and $y = r\sin\theta$.

The above equations can be written into a system of equations in x-y coordinate as follows.

$$\frac{\partial U}{\partial t}+\frac{\partial E}{\partial x}+\frac{\partial F}{\partial y}=\frac{\partial E_v}{\partial x}+\frac{\partial F_v}{\partial y}+S \quad (3.62)$$

$$U=\begin{bmatrix}\rho\\ \rho u_x\\ \rho u_y\\ E_s\\ n_{\mathrm{M}}^+\\ n_{\mathrm{M}^m}\\ n_{\mathrm{S}}^+\\ U_e\end{bmatrix}, E=\begin{bmatrix}\rho u_x\\ \rho u_x^2+p\\ \rho u_x u_y\\ (E_s+p)u_x\\ n_{\mathrm{M}}^+ u_x\\ n_{\mathrm{M}^m}u_x\\ n_{\mathrm{S}}^+u_x\\ (U_e+p_e)u_x\end{bmatrix}, F=\begin{bmatrix}\rho u_y\\ \rho u_x u_y\\ \rho u_y^2+p\\ (E_s+p)u_y\\ n_{\mathrm{M}}^+ u_y\\ n_{\mathrm{M}^m}u_y\\ n_{\mathrm{S}}^+u_y\\ (U_e+p_e)u_y\end{bmatrix},$$

$$E_v=\begin{bmatrix}0\\ \tau_{xx}\\ \tau_{xy}\\ u_x\tau_{xx}+u_y\tau_{xy}-q_{gx}-q_{ex}\\ 0\\ 0\\ 0\\ -q_{ex}\end{bmatrix}, F_v=\begin{bmatrix}0\\ \tau_{yx}\\ \tau_{yy}\\ u_x\tau_{yx}+u_y\tau_{yy}-q_{gy}-q_{ey}\\ 0\\ 0\\ 0\\ -q_{ey}\end{bmatrix}$$

$$
S=\begin{bmatrix}
-\rho u_r \dfrac{1}{h_z}\dfrac{\partial h_z}{\partial r} \\
j_y B_z-\rho u_r \dfrac{1}{h_z}\dfrac{\partial h_z}{\partial r}u_x-P_{LOSS,x} \\
-j_x B_z-\rho u_r \dfrac{1}{h_z}\dfrac{\partial h_z}{\partial r}u_y-P_{LOSS,y} \\
\left\{\begin{array}{r} j_xE_x+j_yE_y+u_x\dfrac{\partial p_e}{\partial x}+u_y\dfrac{\partial p_e}{\partial y}-(u_xP_{LOSS,x}+u_yP_{LOSS,y})-Q_{LOSS} \\ +\dfrac{u_r\tau_{rr}+u_\theta\tau_{r\theta}}{h_z}\dfrac{\partial h_z}{\partial r}-\dfrac{[(E_s+p)u_r+q_{gr}+q_{er}]}{h_z}\dfrac{\partial h_z}{\partial r}\end{array}\right\} \\
\dot{n}_{\mathrm{M}}^{+}-n_{\mathrm{M}}^{+}u_r\dfrac{1}{h_z}\dfrac{\partial h_z}{\partial r} \\
\dot{n}_{\mathrm{M}^{\mathrm{m}}}-n_{\mathrm{M}^{\mathrm{m}}}u_r\dfrac{1}{h_z}\dfrac{\partial h_z}{\partial r} \\
\dot{n}_{\mathrm{S}}^{+}-n_{\mathrm{S}}^{+}u_r\dfrac{1}{h_z}\dfrac{\partial h_z}{\partial r} \\
\dfrac{|\vec{j}|^2}{\sigma}+u_x\dfrac{\partial p_e}{\partial x}+u_y\dfrac{\partial p_e}{\partial y}-\dfrac{3}{2}k_Bn_e(T_e-T_g)\displaystyle\sum_h\dfrac{2m_e}{m_h}\nu_{eh}-[(U_e+p_e)u_r+q_{er}]\dfrac{1}{h_z}\dfrac{\partial h_z}{\partial r}
\end{bmatrix}
$$

Generalized coordinate system transformation

The system of equations (3.55) and (3.62) are transformed into the generalized coordinate system (ξ-η plane) as follows.

$$
\frac{\partial \hat{U}}{\partial t}+\frac{\partial \hat{E}}{\partial \xi}+\frac{\partial \hat{F}}{\partial \eta}=\frac{\partial \hat{E}_v}{\partial \xi}+\frac{\partial \hat{F}_v}{\partial \eta}+\hat{S} \tag{3.63}
$$

Here, for r-z simulation,

$$
\begin{aligned}
&\hat{U}=\frac{U}{J}, \qquad \hat{E}=r_\eta E-z_\eta F, \qquad \hat{F}=-r_\xi E+z_\xi F, \\
&\hat{E}_v=r_\eta E_v-z_\eta F_v, \qquad \hat{F}_v=-r_\xi E_v+z_\xi F_v, \qquad \hat{S}=\frac{S}{J}
\end{aligned} \tag{3.64}
$$

J is the Jacobian, and is defined as follows.

$$
J^{-1}=\begin{vmatrix}\dfrac{\partial z}{\partial \xi} & \dfrac{\partial z}{\partial \eta} \\ \dfrac{\partial r}{\partial \xi} & \dfrac{\partial r}{\partial \eta}\end{vmatrix}=\frac{\partial z}{\partial \xi}\frac{\partial r}{\partial \eta}-\frac{\partial z}{\partial \eta}\frac{\partial r}{\partial \xi}=z_\xi r_\eta-z_\eta r_\xi \tag{3.65}
$$

The second-order central difference method is used to evaluate metrics, and is expressed as follows.

$$\begin{aligned} \frac{\xi_z}{J} = r_\eta = \frac{r_{i,j+1} - r_{i,j-1}}{2}, \qquad & -\frac{\xi_r}{J} = z_\eta = \frac{z_{i,j+1} - z_{i,j-1}}{2} \\ -\frac{\eta_z}{J} = r_\xi = \frac{r_{i+1,j} - r_{i-1,j}}{2}, \qquad & \frac{\eta_r}{J} = z_\xi = \frac{z_{i+1,j} - z_{i-1,j}}{2} \end{aligned} \tag{3.66}$$

For r-θ simulation, just replace z and r in Eqs. (3.64) – (3.66) with x and y, respectively.

The advection terms in Eq. (3.63) [or Eqs. (3.55) and (3.62)] are discretized using the Harten-Yee second-order upwind TVD scheme [32], the viscosity and the heat flux terms are discretized using the second-order differential method. Then, the equations are solved using the second-order Runge-Kutta method for r-z simulation and the Fractional Step Method for r-θ simulation with a time step dt that satisfies the CFL condition.

Initial conditions

The initial condition for plasma fluid flow is set to be constant in the entirety of the generator and to be the same as the inlet values. For r-z simulation, the velocities in z- and θ-direction (u_z, u_θ) are set to be zero. For r-θ simulation, the velocity in θ-direction is set to be zero ($u_\theta = 0$), so from equation (3.61), u_x and u_y are determined.

For the initial condition relating to charged particles (for both r-z and r-θ simulations), the electron temperature is set to be the same as the gas temperature in the entirety of the generator. The ionization degree is set to be 1×10^{-7}, constant in the whole generator. From this ionization degree, electron and ion number densities are determined.

Boundary conditions

Inlet condition for plasma fluid flow

The inlet condition for the fluid flow is given by the isentropic relation for the total pressure $p_{0,in}$, total temperature $T_{0,in}$, and Mach number M_{in} at the generator inlet.

$$p_{in} = p_{0,in} \times \left(1 + \frac{\gamma - 1}{2} M_{in}^2\right)^{-\frac{\gamma}{\gamma - 1}} \tag{3.67}$$

$$T_{g,in} = T_{0,in} \times \left(1 + \frac{\gamma - 1}{2} M_{in}^2\right)^{-1} \tag{3.68}$$

$$\rho_{in} = \frac{p_{in}}{R_s T_{g,in}} \tag{3.69}$$

$$u_{r,in} = M_{in} \cdot \sqrt{\gamma R_s T_{g,in}} \tag{3.70}$$

The total energy density at generator inlet $E_{s,in}$ is given by equation (3.6) with the properties at generator inlet. For r-z simulation, u_z and u_θ at generator inlet are assumed to

be zero. For r-θ simulation, u_θ at generator inlet is assumed to be zero, and from equations (3.61) and (3.70), $u_{x,in}$ and $u_{y,in}$ are determined.

The gas constant R_s [J/(K·kg)] in equation (3.69) is calculated using the universal gas constant $R_c = 8.3145$ [J/(K·mol)] and molar mas m_w [kg/mol].

$$R_s = \frac{R_c}{m_w} \tag{3.71}$$

For the mixed gas (seeded plasma) with a seed fraction (*S.F.*, mole percent), the molar mass m_w is given by

$$m_w = (1 - S.F.) \times m_{w,\mathrm{M}} + S.F. \times m_{w,\mathrm{S}} \tag{3.72}$$

where $m_{w,\mathrm{M}}$ and $m_{w,\mathrm{S}}$ are the molar masses of mother gas and seed material.

Inlet condition for charged particles

The inlet condition for each particle number density is determined from the value at an equilibrium state ($\dot{n}^+_{\mathrm{M}} = 0, \dot{n}_{\mathrm{M^m}} = 0, \dot{n}^+_{\mathrm{S}} = 0$) for a given inlet electron temperature T_{e-in}. At the equilibrium state, from equations (3.26) – (3.28), we obtained

$$\begin{cases} k_{f,\mathrm{M}} n_{\mathrm{M}} n_e + k_{cu} n_{\mathrm{M^m}} n_e - k_{r,\mathrm{M}} n^+_{\mathrm{M}} n_e^2 - k_{rcu} n^+_{\mathrm{M}} n_e^2 = 0 \\ k_{ex} n_{\mathrm{M}} n_e + k_{rcu} n^+_{\mathrm{M}} n_e^2 - k_{dex} n_{\mathrm{M^m}} n_e - k_{cu} n_{\mathrm{M^m}} n_e - k_{pen} n_{\mathrm{M^m}} n_{\mathrm{S}} = 0 \\ k_{f,\mathrm{S}} n_{\mathrm{S}} n_e + k_{pen} n_{\mathrm{M^m}} n_{\mathrm{S}} - k_{r,\mathrm{S}} n^+_{\mathrm{S}} n_e^2 = 0 \end{cases} \tag{3.73}$$

Here,

$$n_{\mathrm{M}} = (n_{\mathrm{M}})_0 - n^+_{\mathrm{M}} - n_{\mathrm{M^m}}, n_{\mathrm{S}} = (n_{\mathrm{S}})_0 - n^+_{\mathrm{S}}, n_e = n^+_{\mathrm{M}} + n^+_{\mathrm{S}} \tag{3.74}$$

where $(n_{\mathrm{M}})_0$ and $(n_{\mathrm{S}})_0$ are the atomic number densities of mother gas and seed material before ionization, respectively.

Substitute Eq. (3.74) in Eq. (3.73) and rearrange the equations, we obtained

$$\begin{cases} k_{f,\mathrm{M}}[(n_{\mathrm{M}})_0 - \boldsymbol{n}^+_{\mathbf{M}} - \boldsymbol{n}_{\mathbf{M^m}}] + k_{cu} \boldsymbol{n}_{\mathbf{M^m}} - (k_{r,\mathrm{M}} + k_{rcu}) \boldsymbol{n}^+_{\mathbf{M}} (\boldsymbol{n}^+_{\mathbf{M}} + \boldsymbol{n}^+_{\mathbf{S}}) = 0 \\ k_{ex}[(n_{\mathrm{M}})_0 - \boldsymbol{n}^+_{\mathbf{M}}](\boldsymbol{n}^+_{\mathbf{M}} + \boldsymbol{n}^+_{\mathbf{S}}) - (k_{ex} + k_{dex} + k_{cu}) \boldsymbol{n}_{\mathbf{M^m}} (\boldsymbol{n}^+_{\mathbf{M}} + \boldsymbol{n}^+_{\mathbf{S}}) \\ \qquad + k_{rcu} \boldsymbol{n}^+_{\mathbf{M}} (\boldsymbol{n}^+_{\mathbf{M}} + \boldsymbol{n}^+_{\mathbf{S}})^2 - k_{pen} \boldsymbol{n}_{\mathbf{M^m}} [(n_{\mathrm{S}})_0 - \boldsymbol{n}^+_{\mathbf{S}}] = 0 \\ k_{f,\mathrm{S}}[(n_{\mathrm{S}})_0 - \boldsymbol{n}^+_{\mathbf{S}}](\boldsymbol{n}^+_{\mathbf{M}} + \boldsymbol{n}^+_{\mathbf{S}}) + k_{pen} \boldsymbol{n}_{\mathbf{M^m}} [(n_{\mathrm{S}})_0 - \boldsymbol{n}^+_{\mathbf{S}}] - k_{r,\mathrm{S}} \boldsymbol{n}^+_{\mathbf{S}} (\boldsymbol{n}^+_{\mathbf{M}} + \boldsymbol{n}^+_{\mathbf{S}})^2 = 0 \end{cases} \tag{3.75}$$

The above system of nonlinear equations is solved using Newton's method and SOR method. In the simulation, to reduce the computational time, each particle number density ($n^+_{\mathrm{M}}, n_{\mathrm{M^m}}, n^+_{\mathrm{S}}$) is calculated separately in advance, then the data of particle number density against electron temperature (in 1 K increments) are loaded into the programming code.

The inlet condition for electron energy U_{e-in} is given as $U_e = \frac{3}{2} n_e k_B T_e + \sum_i \epsilon_e n_i$ with the properties at the inlet.

Outlet condition

The outlet condition is determined by the free outflow boundary condition.

$$f(i_{max}+1, j) = f(i_{max}, j) \tag{3.76}$$

where i is the number of grid in r-direction. j is the number of grid in z-direction for r-z simulation and in θ-direction for r-θ simulation. i_{max} is the number of grid at outlet boundary.

Walls boundary condition (for r-z simulation)

At the walls, the derivative with respect to z (z-direction) is set to be zero.

$$\begin{cases} Lower\ wall: f(i,-1) = f(i,1) \\ Upper\ wall: f(i, j_{max}+1) = f(i, j_{max}-1) \end{cases} \tag{3.77}$$

Here, $j = 0$ is the grid on the lower wall, $j = j_{max}$ is the grid on the upper wall.

For the flow velocity, the Non-slip condition is adopted.

$$\begin{cases} Lower\ wall: \vec{u}(i,0) = \vec{0}, & \vec{u}(i,-1) = -\vec{u}(i,1) \\ Upper\ wall: \vec{u}(i, j_{max}) = \vec{0}, & \vec{u}(i, j_{max}+1) = -\vec{u}(i, j_{max}-1) \end{cases} \tag{3.78}$$

The wall temperature T_w is fixed.

Periodic boundary condition (for r-θ simulation)

For r-θ simulation, the below periodic boundary condition is adopted.

$$f|_{\theta=2\pi} = f|_{\theta=0} \tag{3.79}$$

c) Scheme of elliptic partial differential equation

The elliptic partial differential equations (3.80) and (3.81) for r-z and r-θ numerical simulations are derived from Eqs. (3.37), (3.47), and the electric field $\vec{E} = -\nabla\phi$, where ϕ is the electric potential. The equations (3.80) and (3.81) are discretized using the Galerkin finite element method (for r-z simulation) and the second-order central difference method (for r-θ simulation), respectively, and are solved using the BiCG-Safe method [33], [34].

For r-z simulation

$$\frac{1}{r}\frac{\partial}{\partial r}\left[\frac{r\sigma}{1+\beta^2}\left(-\frac{\partial\phi}{\partial r} + \beta u_r B_z + u_\theta B_z + \frac{1}{e n_e}\frac{\partial p_e}{\partial r}\right)\right] + \frac{\partial}{\partial z}\left[\sigma\left(-\frac{\partial\phi}{\partial z} + \frac{1}{e n_e}\frac{\partial p_e}{\partial z}\right)\right] = 0 \tag{3.80}$$

For r-θ simulation

$$\frac{\partial}{\partial r}\left\{\frac{rh_z\sigma}{1+\beta^2}\left[\left(-\frac{\partial\phi}{\partial r}+u_\theta B_z+\frac{1}{en_e}\frac{\partial p_e}{\partial r}\right)-\beta\left(-\frac{1}{r}\frac{\partial\phi}{\partial\theta}-u_r B_z+\frac{1}{en_e}\frac{\partial p_e}{r\partial\theta}\right)\right]\right\}$$
$$+\frac{\partial}{\partial\theta}\left\{\frac{h_z\sigma}{1+\beta^2}\left[\beta\left(-\frac{\partial\phi}{\partial r}+u_\theta B_z+\frac{1}{en_e}\frac{\partial p_e}{\partial r}\right)+\left(-\frac{1}{r}\frac{\partial\phi}{\partial\theta}-u_r B_z+\frac{1}{en_e}\frac{\partial p_e}{r\partial\theta}\right)\right]\right\}=0 \quad (3.81)$$

Here, h_z is the height of the generator channel.

Boundary conditions

The boundary condition for the electric potential in equations (3.80) and (3.81) is given as $\phi = 0$ on the anode and as $\phi = V_{out}$ on the cathode, where V_{out} is the output voltage. V_{out} should satisfy the relation of $V_{out} = I_{out} \times R_L$, where R_L is the external load resistance, I_{out} is the output current which is expressed as

$$I_{out} = \int_A j_r dA \quad (3.82)$$

and the radial current density (Hall current density) j_r is calculated from the generalized Ohm's law [Eq. (3.37)].

In the actual simulation, for a given load resistance R_L, at first an output voltage (V_b) is given → the electric potential ϕ is calculated from equation (3.80) or (3.81) → the Hall current density j_r is calculated from generalized Ohm's law → the output current I_{out} is calculated from equation (3.82) → $V_{out} = I_{out} \times R_L$. Then, compare V_b and V_{out}. If

$$\left|\frac{V_{out}-V_b}{V_b}\right| < \epsilon \quad (3.83)$$

is true, it is convergent. This means that $V_b = I_{out} \times R_L$ is satisfied, and V_{out} ($\approx V_b$) and I_{out} are the solutions. If it is false, renew V_b by using the below recurrence relation and repeat the process until it is convergent.

$$V_{i+1} = V_i + \alpha(I_{out}R_L - V_i) \quad (3.84)$$

Here, α is the relaxation coefficient and can be from 0.01 to 0.1.

3.2.3 Numerical region and conditions

A cross-sectional view of the disk-shaped Hall-type MHD generator in the r-z plane is shown in Fig. 3.1. Fig. 3.2 shows the view of the disk generator in r-θ plane. The radius of the throat is 80 mm and height of it is 10 mm. The numerical region is from the upstream edge of the anode (r = 90 mm, height h_z = 10.2 mm) to the downstream edge of the cathode (r = 200 mm, height h_z = 12 mm) in the r-z and r-θ planes for r-z and r-θ simulations, respectively. In r-

z simulation, there are 101 grids in the r-direction and 31 grids in the z-direction. The mesh sizes in the r-direction are Δr = 0.73 mm on the electrode surfaces and 1.2 mm in the generator channel (r = 98–192 mm), whereas in the z-direction the mesh is set to be finer near the wall, the value of it at the main stream is Δz = 0.71 mm and that near the wall is 0.08 mm. In r-θ simulation, there are 56 grids in the r-direction and 360 grids in the θ-direction. The mesh sizes in the r- and θ-directions are Δr = 2 mm and $\Delta\theta = \pi/180$, respectively.

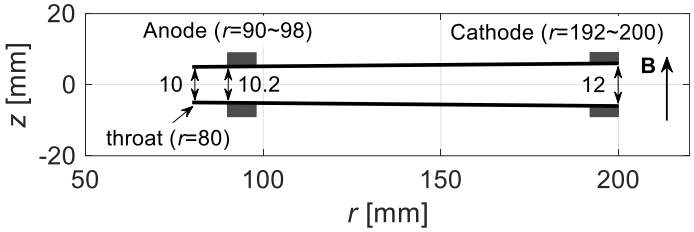

Fig. 3.1 Cross-sectional view of a disk-shaped MHD generator in the *r*-*z* plane. The gas flows in the *r*-direction.

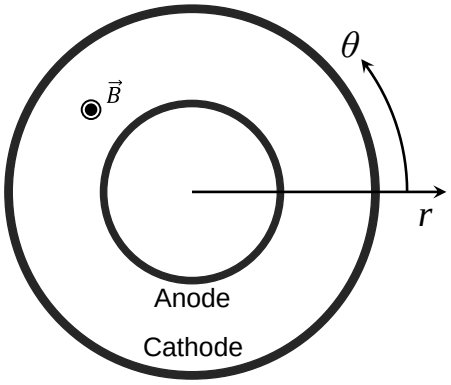

Fig. 3.2 A disk-shaped MHD generator shown in the *r*-θ plane.

The numerical conditions are shown in Table 3.3. The working gases are Xe-seeded Ar (Ar/Xe), Xe-seeded Ne (Ne/Xe), and Xe-seeded He (He/Xe). The seed fraction (*S.F.*, mole % of Xe) is varied from 0.0% to 100.0%. *S.F.* = 0.0% means pure Ar, pure Ne, pure He, and *S.F.* = 100.0% means pure Xe. The numerical simulations are conducted under an inlet total pressure of 0.3 MPa, inlet total temperature of 2500 K, inlet Mach number of 1.49, and magnetic flux density of 2.0 T. In the simulation, the inlet electron temperature and external load resistance are varied, then the enthalpy extraction ratio (*E.E.R.*) of Eq. (3.85) and isentropic efficiency (*I.E.*) of Eq. (3.86) are calculated. The enthalpy extraction ratio has the maximum value against the load resistance. Therefore, the maximum enthalpy extraction ratio at the optimum load resistance at a given inlet electron temperature will be subject to discussion.

Table 3.3 Numerical conditions

Working gas		Ar/Xe, Ne/Xe, He/Xe
Seed fraction (*S.F.*)	[%]	0.0 – 100.0
Inlet total pressure	[MPa]	0.30
Inlet total temperature	[K]	2500
Inlet Mach number	[–]	1.49
Wall temperature	[K]	1000
Magnetic flux density	[T]	2.0
Load resistance	[Ω]	0.01 – 5.0

$$E.E.R. = \frac{V_{out} I_{out}}{Q_{in}} \tag{3.85}$$

$$I.E. = \frac{E.E.R.}{1 - \left(\frac{p_{0,out}}{p_{0,in}}\right)^{\frac{\gamma-1}{\gamma}}} \tag{3.86}$$

$$P.P. = \left(\frac{3}{2} n_e k_B T_e + \sum_i \epsilon_i n_i + p_e\right) u_r A_{in} \tag{3.87}$$

$$P.P.R. = \frac{P.P.}{Q_{in}} \tag{3.88}$$

$$Q_{in} = \left[\rho_g \left(c_\nu T_g + \frac{1}{2}|\vec{u}|^2\right) + p_g\right] u_r A_{in} + P.P. \tag{3.89}$$

Here, A_{in} is the cross-sectional area at the generator inlet, $p_{0,in}$ the inlet total pressure, $p_{0,out}$ the outlet total pressure, Q_{in} the thermal input.

The pre-ionization power ($P.P.$) of Eq. (3.87) is defined as the net power used for plasma production (in the physical meaning, it is the electron thermal input), and the pre-ionization power ratio ($P.P.R.$) of Eq. (3.88) is defined as the ratio of the pre-ionization power ($P.P.$) to the thermal input (Q_{in}).

The outlet total pressure $p_{0,out}$ is obtained by mass flow rate-weighted average [Eq. (3.90)] in z-direction for r-z simulation and in θ-direction for r-θ simulation.

$$p_{0,out} = \frac{\int_{A_{out}} (\rho u) p_0 dA}{\int_{A_{out}} \rho u dA} \tag{3.90}$$

3.3 Performance of Xe-seeded noble gas plasma MHD generator (*r-z* simulation)

In this section, the power generator performance in Xe-seeded noble gas (Ar, Ne, He) plasma obtained by r-z two-dimensional numerical simulation under various seed fractions (*S.F.*) is presented. *S.F.* = 0.0% means pure Ar, pure Ne, pure He, and *S.F.* = 100.0% means pure Xe. First, in subsection 3.3.1, we describe the features of generator performance in pure noble gases. Then, the effect of Xe on the power generator performance will be described in subsection 3.3.2.

3.3.1 Generator performance in pure noble gases

In this section, the power generator performance in pure Xe, pure Ar, pure Ne, and pure He is discussed. The enthalpy extraction ratio (*E.E.R.*, closed dot) and isentropic efficiency (*I.E.*, open dot) against the inlet electron temperature under each working gas are shown in Fig. 3.3. At each inlet electron temperature, the load resistance is varied so as to obtain optimum load resistance for providing maximum output power (maximum *E.E.R.*). It can be seen from Fig. 3.3 that there exists an optimum inlet electron temperature for providing maximum enthalpy extraction ratio for any working gas. This is because the electrical conductivity in the generator increases with increasing inlet electron temperature, but an excessively high inlet electron temperature reduces the Hall parameter, resulting in degradation of the enthalpy extraction ratio. Table 3.4 shows various quantities relating to generator performance at optimum condition in pure noble working gases. As shown in the figure and table, the maximum *E.E.R.* and the corresponding *I.E.* of each working gas from the highest are Ne, Ar, He, and Xe. The inlet electron temperatures at that time (optimum value) in the ascending order are Xe (6700 K), Ar (7900 K), Ne (10000 K), and He (11400 K). This is because the lower the ionization potential of the noble gas, the higher electrical conductivity can be obtained even at low electron temperature. As shown in the same table, the pre-ionization power [*P.P.*, Eq. (3.87)] is on the same level for Xe, Ar, Ne, but comparatively large for He due to the very high ionization potential, excitation energy and high velocity in He. The pre-ionization power ratios [*P.P.R.*, Eq. (3.88)] from the highest are Xe, Ar, Ne because the thermal inputs are getting larger in that order [Q_{in}(Xe) < Q_{in}(Ar) < Q_{in}(Ne)]. However, the pre-ionization power ratio in He is higher compared with Ne regardless of the high thermal input, due to the pre-ionization power is high. Among these four types of noble gases, Ne provides the highest net enthalpy extraction ratio (*net E.E.R.* = *E.E.R.* – *P.P.R.*, equivalent to the value obtained by subtracting pre-ionization power from output power).

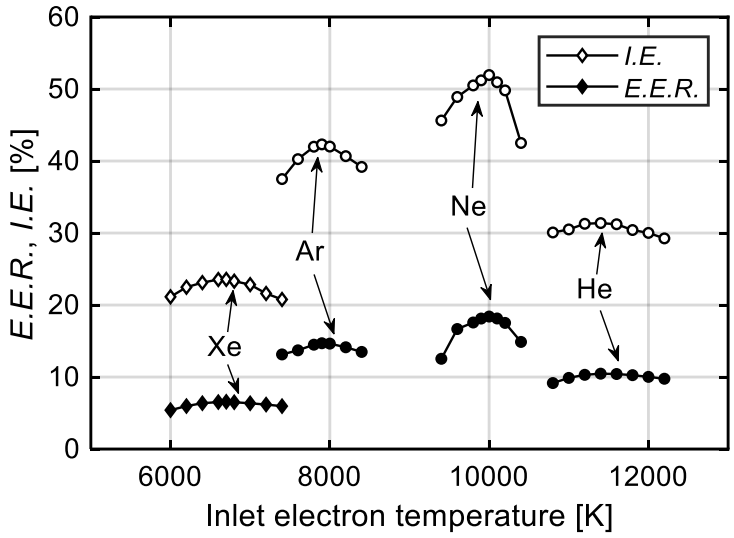

Fig. 3.3 Enthalpy extraction ratio (*E.E.R.*, closed dot) and isentropic efficiency (*I.E.*, open dot) against inlet electron temperature under pure noble gas.

Table 3.4 Various quantities at optimum condition in pure noble working gases

Working gas (*S.F.* [%])		Pure Xe (100.0%)	Pure Ar (0.0%)	Pure Ne (0.0%)	Pure He (0.0%)
Q_{in}	[MW]	1.13	2.02	2.82	6.34
T_{e-in}	[K]	6700	7900	10000	11400
R_L	[Ω]	0.31	0.29	0.41	0.77
S_p	[-]	1.41×10^{-2}	2.13×10^{-2}	2.33×10^{-2}	1.85×10^{-2}
$E.E.R.$	[%]	6.57	14.7	18.4	10.5
$I.E.$	[%]	23.6	42.3	51.9	31.4
$P.P.$	[kW]	39.8	43.7	47.0	109.4
$P.P.R.$	[%]	3.53	2.17	1.67	1.72

The factors that Ne provides the highest enthalpy extraction ratio and isentropic efficiency are explained as follows. The S_p shown in Table 3.4 is the interaction parameter at optimum condition under each working gas. The interaction parameter, as shown in equation (3.91), is the strength of Lorentz force with respect to the inertial force of the fluid [51], and it depicts the strength of MHD interaction (an interaction between a conducting fluid with a magnetic field).

$$S_p = \frac{\int_{V_{all}} |-j_\theta B_z| dV}{\int_{A_{in}} (p + \rho u_r^2) dA} \tag{3.91}$$

Here, V_{all} is the generator volume. High interaction parameter under the same magnetic flux density indicates that the current density in the generator channel is high. As shown in Table 3.4, the interaction parameters in the descending order are Ne (high), Ar, He, and Xe (low). For Ne, due to the high electrical conductivity, relatively high velocity (relatively small atomic weight), the current density is high compared with the other working gases, as a result the interaction parameter becomes higher, which is a primary factor for providing the highest enthalpy extraction ratio. It should be noted that for Xe or He, we can also improve the enthalpy extraction ratio by increasing the interaction parameter, in a direct way is to increase the applied magnetic flux density.

Fig. 3.4 shows the radial distribution of electrical efficiency η_e at optimum condition under each working gas. The electrical efficiency [2], as defined by equation (3.92), is the ratio between the electrical power output and the "push work" which is a work done by the gas pushing itself against the Lorentz force.

$$\eta_e = \frac{\left|\vec{j}\cdot\vec{E}\right|}{\left|-\vec{u}\cdot\left(\vec{j}\cdot\vec{B}\right)\right|} = \frac{\beta^2 K_h}{1+\beta^2 K_h}(1-K_h) \tag{3.92}$$

Here, $K_h = -E_r/\beta u_r B_z$ is the loading parameter. As seen in the figure, Ne has a high electrical efficiency due to the high Hall parameter β which is a result of small collision cross section of Ne atom with electron compared with other noble gases. This is a primary factor which gives the highest isentropic efficiency in pure Ne. In case of Xe, mainly because of the low flow velocity (low electromotive force) due to the large atomic weight, and in case of He, mainly because of the low Hall parameter and electrical conductivity due to the large collision cross section of He with electron, the generator performance becomes relatively low.

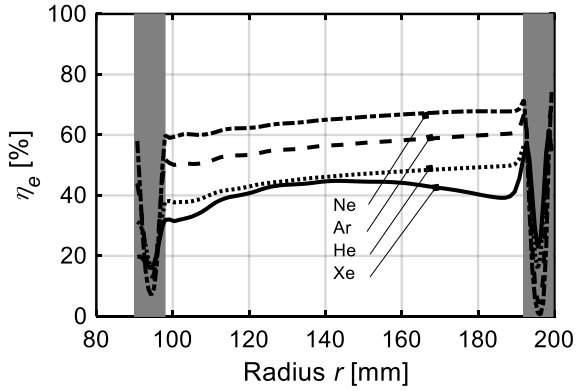

Fig. 3.4 Radial distribution of electrical efficiency η_e at optimum condition under each pure noble gas (at $z = 0$).

3.3.2 Effect of xenon seed on generator performance

In this subsection, the effects that Xe seed have on the generator performance are discussed. Fig 3.5 shows the enthalpy extraction ratio and isentropic efficiency against the inlet electron temperature at various seed fractions under (a) Ar/Xe, (b) Ne/Xe, and (c) He/Xe working gases. The closed dot indicates the enthalpy extraction ratio, and the open dot indicates the isentropic efficiency. It can be seen from the figure that for any working gas, as the seed fraction increases the maximum *E.E.R.* remain almost the same, whereas the optimum inlet electron temperature for providing maximum *E.E.R.* decreases. This is because high electrical conductivity can be obtained as the amount of Xe in the mixed gas increases, even at a low inlet electron temperature, due to the low ionization potential of Xe.

Table 3.5 shows various quantities relating to generator performance at optimum condition under various seed fractions in (a) Ar/Xe, (b) Ne/Xe, and (c) He/Xe working gases. As seen in the table, for Ne/Xe and He/Xe, by adding (seeding) a small amount of Xe (seed fraction around 0.05 – 1.0%), the optimum inlet electron temperature and *P.P.R.* greatly decrease compared with those in Ar/Xe, whereas the generator performance remains almost the same. This is due to the difference in ionization potential of Xe seed and mother gas. For Ar/Xe, because the difference in ionization potential between those gas is small, the decreases of the optimum inlet electron temperature and *P.P.R.* are also small. Note that in cases of Ne/Xe and He/Xe, at a low seed fraction of around 0.01%, the required inlet electron temperature becomes close to that in pure working gas because to obtain adequate electrical conductivity, it is necessary to ionize even the mother gas.

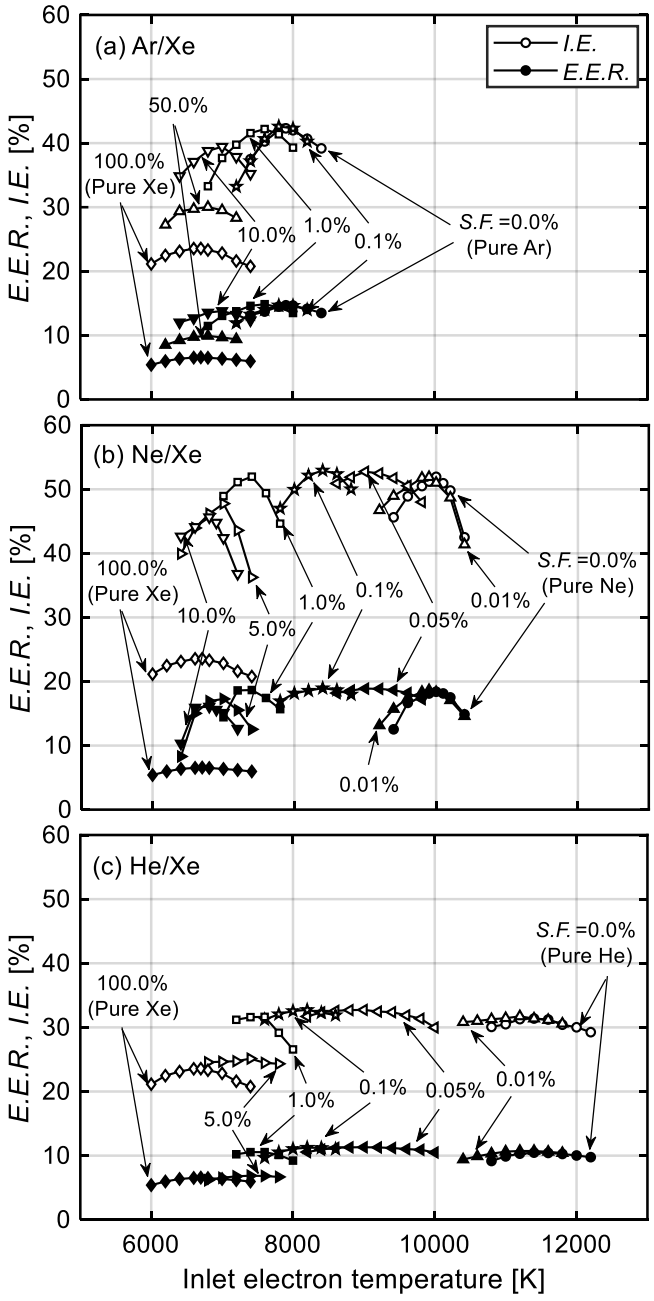

Fig. 3.5 Enthalpy extraction ratio (*E.E.R.*, closed dot) and isentropic efficiency (*I.E.*, open dot) against inlet electron temperature at various seed fractions (*S.F.*) under (a) Ar/Xe, (b) Ne/Xe, and (c) He/Xe working gases.

Table 3.5 Each quantity at optimum condition in Xe-seeded working gases

(a) Ar/Xe

$S.F.$	[%]	0.0 (Ar)	0.1	1.0	10.0	50.0	100.0 (Xe)
Q_{in}	[MW]	2.02	2.01	1.99	1.81	1.35	1.13
T_{e-in}	[K]	7900	7800	7600	7000	6800	6700
R_L	[Ω]	0.29	0.29	0.20	0.16	0.22	0.31
S_p	[–]	14.7	14.7	14.9	13.8	9.92	6.57
$E.E.R.$	[%]	42.3	42.6	42.2	39.4	30.0	23.6
$I.E.$	[%]	43.7	38.7	37.5	34.3	41.3	39.8
$P.P.$	[kW]	2.17	1.93	1.89	1.89	2.97	3.53
$P.P.R.$	[%]	2.02	2.01	1.99	1.81	1.35	1.13

(b) Ne/Xe

$S.F.$	[%]	0.0 (Ne)	0.01	0.05	0.1	1.0	5.0	10.0	100.0 (Xe)
Q_{in}	[MW]	2.82	2.82	2.80	2.80	2.73	2.49	2.26	1.13
T_{e-in}	[K]	10000	9900	9000	8400	7400	7000	6800	6700
R_L	[Ω]	0.41	0.40	0.34	0.31	0.23	0.17	0.18	0.31
S_p	[–]	18.4	18.6	18.9	19.0	18.7	17.3	16.1	6.57
$E.E.R.$	[%]	51.9	51.9	52.7	52.9	52.0	47.8	45.6	23.6
$I.E.$	[%]	47.0	42.2	26.5	26.3	28.5	32.6	30.4	39.8
$P.P.$	[kW]	1.67	1.50	0.95	0.94	1.04	1.31	1.35	3.53
$P.P.R.$	[%]	2.82	2.82	2.80	2.80	2.73	2.49	2.26	1.13

(c) He/Xe

$S.F.$	[%]	0.0 (He)	0.01	0.05	0.1	1.0	5.0	100.0 (Xe)
Q_{in}	[MW]	6.34	6.32	6.24	6.19	5.51	3.96	1.13
T_{e-in}	[K]	11400	11200	9000	8200	7600	7400	6700
R_L	[Ω]	0.77	0.71	0.44	0.48	0.58	1.96	0.31
S_p	[–]	10.5	10.7	11.3	11.2	10.6	6.87	6.57
$E.E.R.$	[%]	31.4	31.7	32.7	32.7	31.6	25.1	23.6
$I.E.$	[%]	109.4	88.1	54.7	48.2	74.7	92.3	39.8
$P.P.$	[kW]	1.72	1.39	0.88	0.78	1.36	2.33	3.53
$P.P.R.$	[%]	6.34	6.32	6.24	6.19	5.51	3.96	1.13

As discussed above, although the effect of seeding Xe is varied to a greater or lesser extent under each working gas, is has the same tendency. Here, we focus and discuss in detail on the case of Ne/Xe which has a remarkable seeding effect and has the highest maximum *E.E.R.* and *I.E.*

As shown in Table 3.5(b), at low seed fractions (around 0.01 – 1.0%), both pre-ionization power and pre-ionization power ratio decrease with increasing seed fraction due to the decrease in the required inlet electron temperature (optimum inlet electron temperature). In particular, at seed fractions around 0.05 – 1.0%, they decrease to about 60% of those of pure Ne. However, as we further increase the seed fraction, the pre-ionization power and pre-ionization power ratio increase in spite of the decrease in optimum inlet electron temperature. At excessively high seed fraction, the flow velocity reduces owing to large atomic weight of Xe; consequently, more seed material needs to be ionized to maintain high performance. Moreover, at low seed fractions (around 0.01 – 1.0%) both *E.E.R.* and *I.E.* remain almost the same, but at a high seed fraction (5.0% or above) *E.E.R.* and *I.E.* decrease with increasing seed fraction. The effect of seed fraction on the generator performance can be explained using the radial distributions of electrical efficiency, Hall parameter, electrical efficiency, and radial velocity at optimum condition as shown in Fig. 3.6. As shown in the figure, at low seed fractions the electrical conductivity [Eq. (3.40)] increases with increasing seed fraction; however, at excessively high seed fractions it gradually decreases. This is because the electron number density increases with increasing seed fraction, but as the seed fraction increase excessively the increment of electron collision frequency becomes dominant owing to the increase in the ion number density (= electron number density) and the large collision cross section of Xe with electron. The Hall parameter [Eq. (3.40)], on the other hand, only slightly decreases at low seed fractions, but at excessively high seed fractions it decreases greatly due to the significant increase in electron collision frequency as stated above. There is almost no difference in electrical efficiency [Eq. (3.92)] at low seed fractions, but at excessively high seed fractions it decreases greatly due to the decrease in Hall parameter. Similar to electrical efficiency, the radial velocity remains almost the same at low seed fractions, but decreases greatly at excessively high seed fractions due to the large atomic weight of Xe (this results in the decrease of Hall electromotive force $\beta u_r B_z$). The decreases in electrical conductivity, Hall parameter, electrical efficiency and velocity are the factor to deteriorate the generator performance at excessively high seed fractions. Note that in the conditions of Fig. 3.6, the Mach number of the flow changes smoothly from 1.49 at the upstream edge (the left end) of anode to around 1.3 for pure Ne, around 1.1 – 1.2 for Ne/Xe, and around 1.8 for pure Xe, at the upstream edge (the left end) of cathode, while maintaining the supersonic speed.

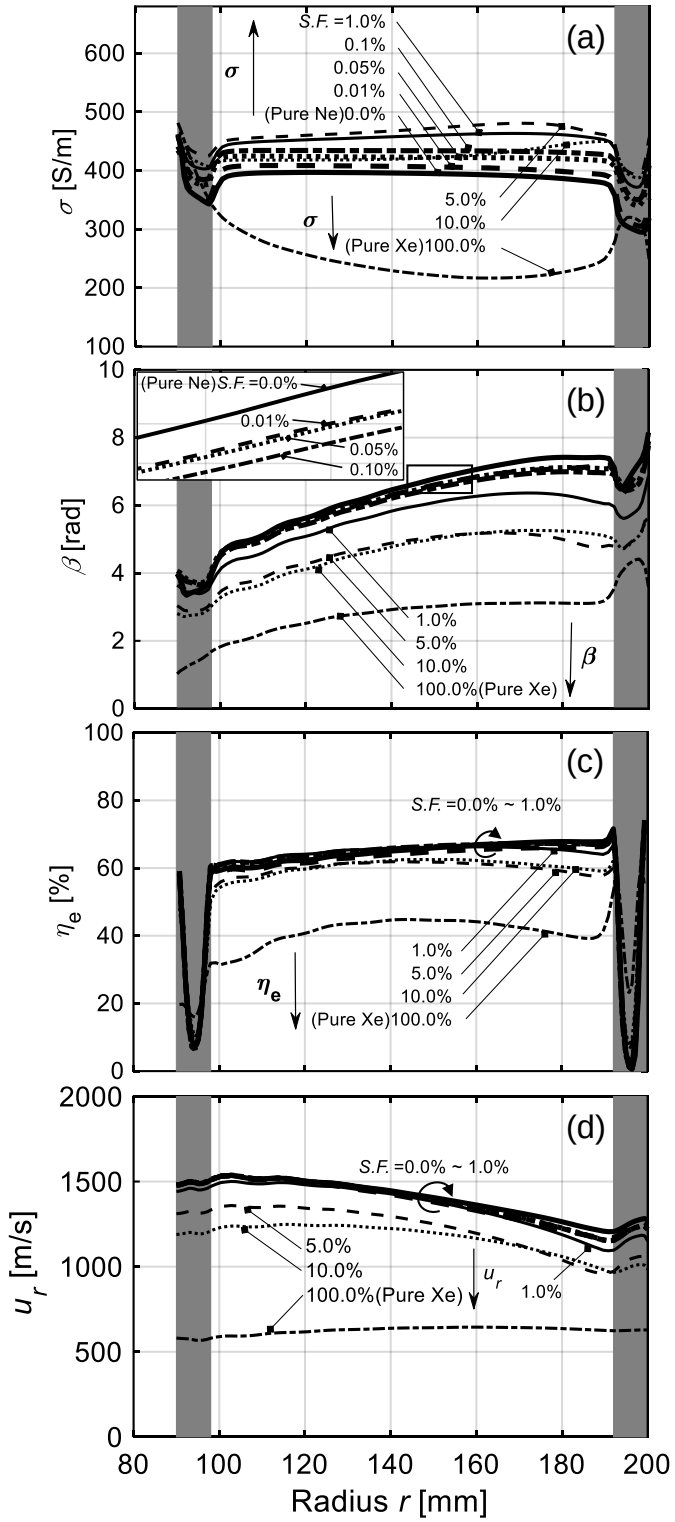

Fig. 3.6 Radial distributions of (a) electrical conductivity σ, (b) Hall parameter β, (c) electrical efficiency η_e, and (d) radial velocity u_r at the optimum condition under various seed fractions in Ne/Xe (at $z = 0$).

Now, only direct ionization and three-body recombination are considered as an ionization-recombination model in Xe-seeded noble gas plasma like in the conventional alkali metal seeded plasma [52] (also see section 2.2.1a of chapter 2). Under this simple ionization-recombination model, at a representative condition of Ne/Xe, the decrease rate of Xe ion is around 1%, the maximum *E.E.R.* remains the same; however, the inlet ionization at that time increases, and the pre-ionization power increases by around 3%. This difference is mainly due to the presence or absence of the Penning ionization process in the model. Although the effect of the Penning ionization cannot be neglected in the plasma reaction model utilized in the present study, we can say that it is not so much as to affect the approximate evaluation of generator performance. In this regard, however, for more precisely, a detailed Collisional-Radiative (C-R) model should be constructed that takes into account many excitation energy levels, and at each excitation energy level considers the collisional excitation, collisional de-excitation, de-excitation due to the radiation and energy loss due to the radiation.

3.4 Performance and plasma behavior in Ne/Xe plasma MHD generator (comparison of *r-z* and *r-θ* simulations)

In this section, the generator performance with a Ne/Xe working gas is examined by r-θ two-dimensional numerical simulations. The results obtained from the r-θ simulation are compared with r-z simulation in order to evaluate the generator performance more precisely, including the effects of the boundary layer and plasma uniformity.

3.4.1 Generator performance under different seed fractions

Fig. 3.7a and Fig. 3.7b show the enthalpy extraction ratio and isentropic efficiency against the inlet electron temperature as obtained from the r-z and r-θ numerical simulations, respectively, under different seed fractions. The closed dot indicates the enthalpy extraction ratio, and the open dot indicates the isentropic efficiency. As shown in both figures, for any seed fraction there is an optimum inlet electron temperature for providing maximum enthalpy extraction ratio. Moreover, at low seed fractions (0.01–1.0%), the maximum enthalpy extraction ratio and isentropic efficiency remain almost the same as the seed fraction increases, whereas the optimum inlet electron temperature decreases. At an excessively high seed fraction (5.0% or above), on the other hand, the enthalpy extraction ratio and isentropic efficiency decrease. Namely, results obtained from the r-θ simulation have the same tendency as those results obtained from r-z simulation, i.e., the profiles of the *E.E.R.* and *I.E.* in both figures are the almost the same. The reasons and factors leading to this profile were discussed in subsection 3.3.2.

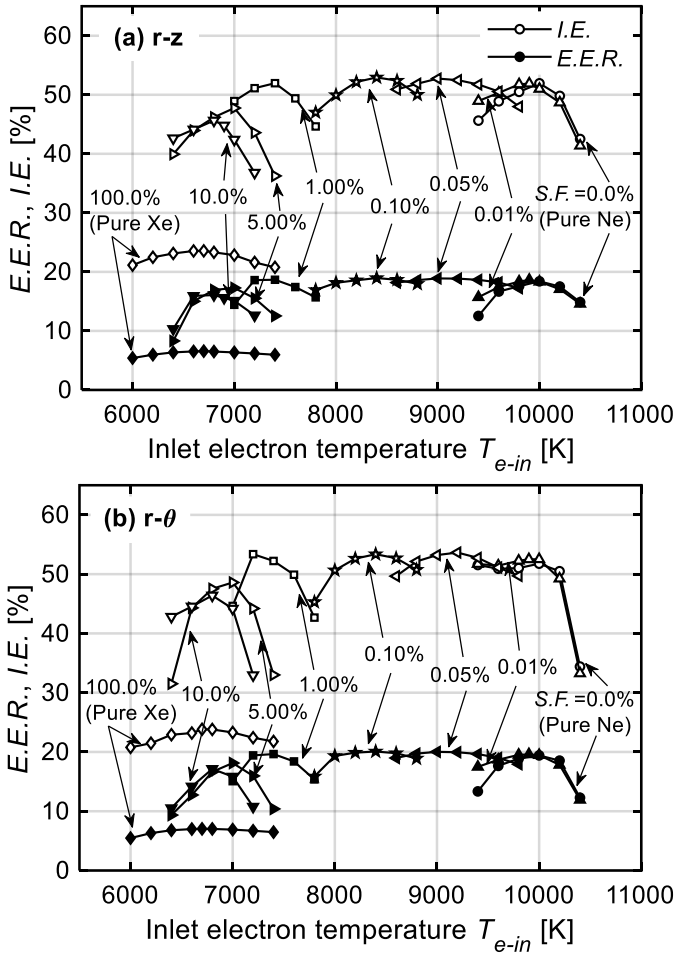

Fig. 3.7 Enthalpy extraction ratio and isentropic efficiency against inlet electron temperature obtained from (a) *r-z* numerical simulation and (b) *r-θ* numerical simulation.

Fig. 3.8a and Fig. 3.8b show the enthalpy extraction ratio and isentropic efficiency against the pre-ionization power ratio obtained by the r-z and r-θ numerical simulations, respectively, under different seed fractions. Similar to the inlet electron temperature in Fig. 3.7, there is an optimum pre-ionization power ratio for providing the maximum enthalpy extraction ratio. As the seed fraction increases, although the optimum inlet electron temperature largely decreases, the optimum pre-ionization power ratio seems to only slightly change, which is a result of the non-linear relationship between the electron temperature and the pre-ionization power [Eq. (3.87)].

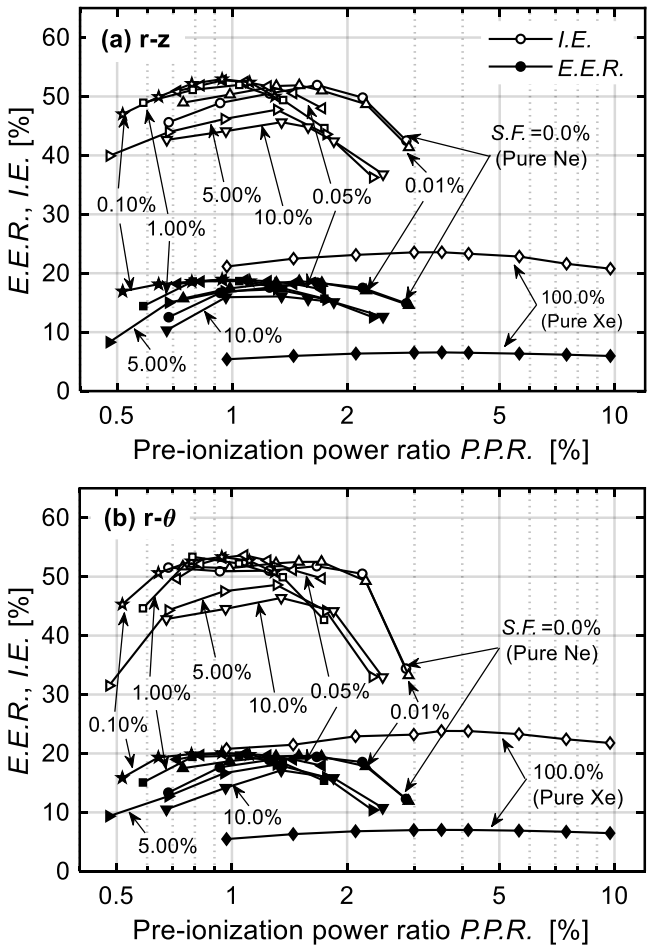

Fig. 3.8 Enthalpy extraction ratio and isentropic efficiency against pre-ionization power ratio obtained from (a) *r-z* numerical simulation and (b) *r-θ* numerical simulation.

By comparing the performance obtained from the r-z and r-θ simulations (Figs. 3.8 and 3.9), it can be seen that the performance in the r-θ simulation is almost the same as that in the r-z simulation for any seed fraction. Table 3.6 shows a quantitative comparison of the performance obtained by the r-z and r-θ simulations at optimum condition for each seed fraction. At each seed fraction, the optimum inlet electron temperatures and pre-ionization power ratios for giving the maximum enthalpy extraction ratio in the r-θ simulation match with those in the r-z simulation for increments of 100 K in the inlet electron temperature. At low seed fractions (0.01–1.00%), the pre-ionization power ratio *P.P.R.* decreases with increasing seed fraction due to the decreasing inlet electron temperature. However, at an excessively high seed fraction (5.0% or above), the pre-ionization power ratio increases as the seed fraction increases. At excessively high seed fraction, the flow velocity reduces owing to large atomic weight of Xe; consequently, more seed material needs to be ionized to maintain high performance. The optimum load resistances in the r-z and r-θ simulations are almost the same. The enthalpy extraction ratio and isentropic

efficiency obtained from the r-θ simulation almost match with those obtained from the r-z simulation with differences within around 1.0 %point.

Table 3.6 A quantitative comparison of performance obtained from *r-z* and *r-θ* simulations at optimum condition

S.F. [%]	Q_{in} [MW]	$T_{e\text{-}in}$ [K]		*P.P.R.* [%]	R_L [Ω]		*E.E.R.* [%]		*I.E.* [%]		$E.E.R._{r\text{-}\theta} - E.E.R._{r\text{-}z}$ [% pt]	$I.E._{r\text{-}\theta} - I.E._{r\text{-}z}$ [% pt]
		r-z	*r-θ*		*r-z*	*r-θ*	*r-z*	*r-θ*	*r-z*	*r-θ*		
0.0 (Ne)	2.82	10000	10000	1.67	0.41	0.42	18.4	19.4	51.9	51.8	1.0	–0.1
0.01	2.82	9900	9900	1.50	0.40	0.38	18.6	19.6	51.9	52.2	1.0	0.3
0.05	2.80	9000	9000	0.95	0.34	0.34	18.9	20.0	52.7	53.2	1.1	0.5
0.10	2.80	8400	8400	0.94	0.31	0.31	19.0	20.1	52.9	53.4	1.1	0.5
1.00	2.73	7400	7400	1.04	0.23	0.23	18.7	19.6	52.0	52.2	0.9	0.2
5.00	2.49	7000	7000	1.31	0.17	0.16	17.3	18.1	47.8	48.6	0.8	0.8
10.0	2.26	6800	6800	1.35	0.18	0.18	16.1	17.1	45.6	46.4	1.0	0.8
100.0 (Xe)	1.13	6700	6700	3.53	0.31	0.31	6.57	7.02	23.6	23.8	0.5	0.2

3.4.2 Generator performance and plasma behavior at a representative seed fraction of 0.1%

Fig. 3.9a and Fig. 3.9b show the output voltage-current characteristics, and the enthalpy extraction ratio and isentropic efficiency against load resistance, respectively, as obtained from the r-z and r-θ simulations at a seed fraction of 0.1% and an optimum inlet electron temperature of 8400 K. For the results obtained from both simulations, the output power (Fig. 3.9a) and enthalpy extraction ratio (Fig. 3.9b) increase with increasing load resistance, reaching maximum at a load resistance of 0.31 Ω which is attributed to the increase in electrical conductivity. Above this optimum load resistance of 0.31 Ω, however, the output power and enthalpy extraction ratio decrease gradually owing to the reduction in the Hall parameter and flow velocity. Similar to the enthalpy extraction ratio, the isentropic efficiency increases with increasing load resistance and decreases at excessively high load resistance. Note here that for the results obtained from the r-θ simulation, for a load resistance of 0.39 Ω or above where the plasma is not uniform (which we will discuss below), the output voltage (Fig. 3.9a) drops abruptly. Then, the enthalpy extraction

ratio and isentropic efficiency decrease greatly and become lower than those in the r-z simulation (Fig. 3.9b).

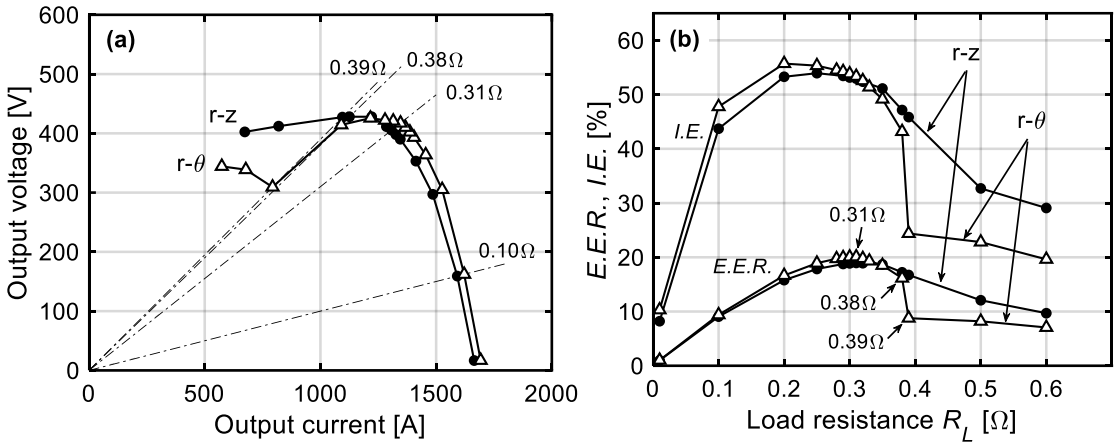

Fig. 3.9 Comparison of performance obtained from the *r-z* and *r-θ* numerical simulations at a seed fraction of 0.1% and an inlet electron temperature of 8400 K: (a) output voltage-current characteristics and (b) enthalpy extraction ratio and isentropic efficiency against load resistance.

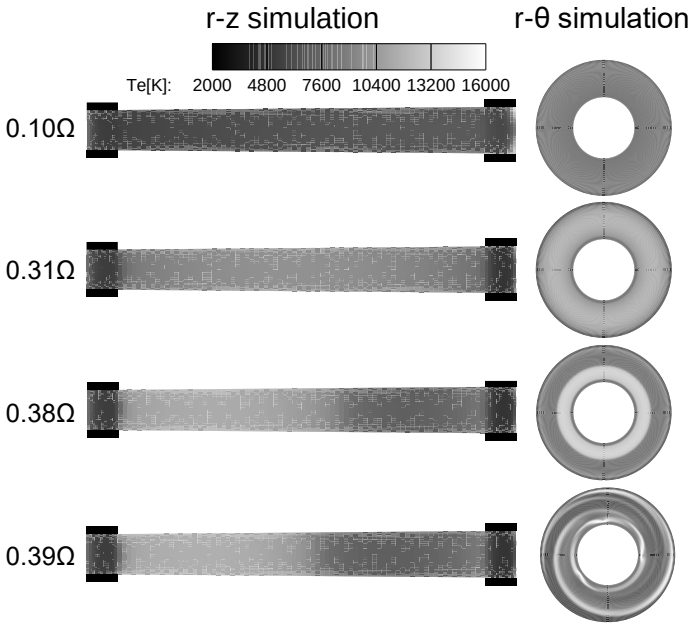

Fig. 3.10 Electron temperature distribution obtained from the *r-z* numerical simulation and that from the *r-θ* numerical simulation at a seed fraction of 0.1% and an inlet electron temperature of 8400 K.

Fig. 3.10 shows the plasma structures (electron temperature distribution) from the r-z and r-θ numerical simulations at different load resistances. At load resistances of 0.38 Ω or below, the plasmas are almost uniform in the r-z and r-θ planes. At a higher load resistance (0.39 Ω), the plasma obtained from the r-θ simulation becomes nonuniform with the spiral structure rotating clockwise, whereas the plasma obtained from the r-z simulation appears to stay almost uniform, where the plasma is compulsorily assumed to be uniform in θ-direction. This non-uniform plasma in the r-θ plane at high load resistance contributes greatly to the deterioration of generator performance and results in lower generator performance in the r-θ simulation compared with the r-z simulation.

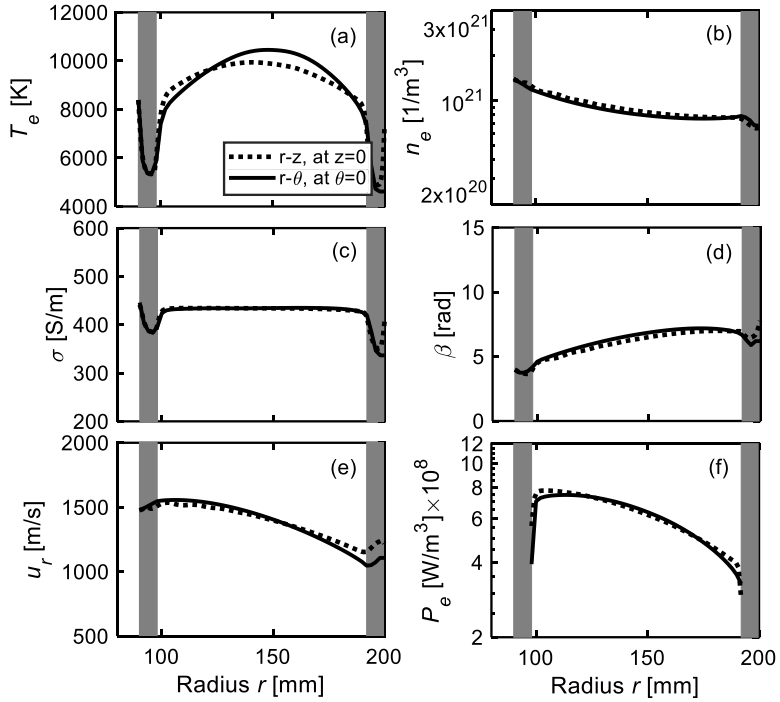

Fig. 3.11 Comparison of (a) electron temperature, (b) electron number density, (c) electrical conductivity, (d) Hall parameter, (e) radial flow velocity, and (f) electrical power output density between the *r-z* and *r-θ* simulations at an optimum load resistance of 0.31 Ω under a seed fraction of 0.1% and an inlet electron temperature of 8400 K.

Fig. 3.11 shows a comparison of electron temperature, electron number density, electrical conductivity, Hall parameter, radial flow velocity, and electrical power output density [Eq. (3.93)] between the r-z and r-θ simulations at the optimum load resistance of 0.31 Ω under a seed fraction of 0.1% and an inlet electron temperature of 8400 K, in which the plasma is uniform. The plasma fluid properties in the r-z simulation are taken at the mainstream ($z = 0$) and those in the r-θ numerical simulation are taken at $\theta = 0$ deg.

$$P_e = -\vec{j}\cdot\vec{E} = \frac{\beta^2}{1+\beta^2} K_h(1-K_h)\sigma u_r^2 B_z^2 \tag{3.93}$$

Here, $K_h = -E_r/\beta u_r B_z$ is the loading parameter, and E_r is the electric field in the r-direction.

Under the uniform plasma, each plasma fluid property obtained in the r-θ simulation, including electron temperature, electron number density, electrical conductivity, Hall parameter, and flow velocity, is almost the same as that at the mainstream in the r-z simulation (Figs. 3.11a – 3.11e). Consequently, the electrical power output densities in the r-θ and r-z simulations are almost the same (Fig. 3.11f). It should be noted here that under the uniform structure, the parameters of the plasma fluid are uniform in θ-direction, such that the value at $\theta =$ 0 deg is the same as the value averaged in the θ-direction.

The height distributions of electron temperature, electron number density, electrical conductivity, Hall parameter, flow velocity, and electrical power output density in the r-θ simulation are shown in Fig. 3.12. The values are taken at the downstream edge of the anode (r = 98 mm; solid line), at the center of the generator channel (r = 145 mm; dashed line), and at the upstream edge of the cathode (r = 192 mm; dotted line). In the boundary layer region near the walls, basically, with the reduction of flow velocity (Fig. 3.12e), the static temperature increases and mass density decreases under the almost constant static pressure. The electron temperature (Fig. 3.12a) appears to be roughly constant in the z-direction even in the boundary layer region. This can be attributed to the static gas temperature increasing but the Joule heating decreasing due to low flow velocity. The electron number density decreases greatly near the walls (Fig. 3.12b) because of the reduction of mass density, resulting in a decrease in electrical conductivity (Fig. 3.12c) and an increase in Hall parameter (Fig. 3.12d) near the walls. The electric power output density decreases greatly near the walls (Fig. 3.12f) which is basically attributed to the low velocity in the boundary layer. The decrease in electrical power output density near the walls causes the enthalpy extraction ratio and isentropic efficiency in the r-z simulation to become slightly lower than those in the r-θ simulation as shown in Figs. 3.7 – 3.9, and Table 3.6.

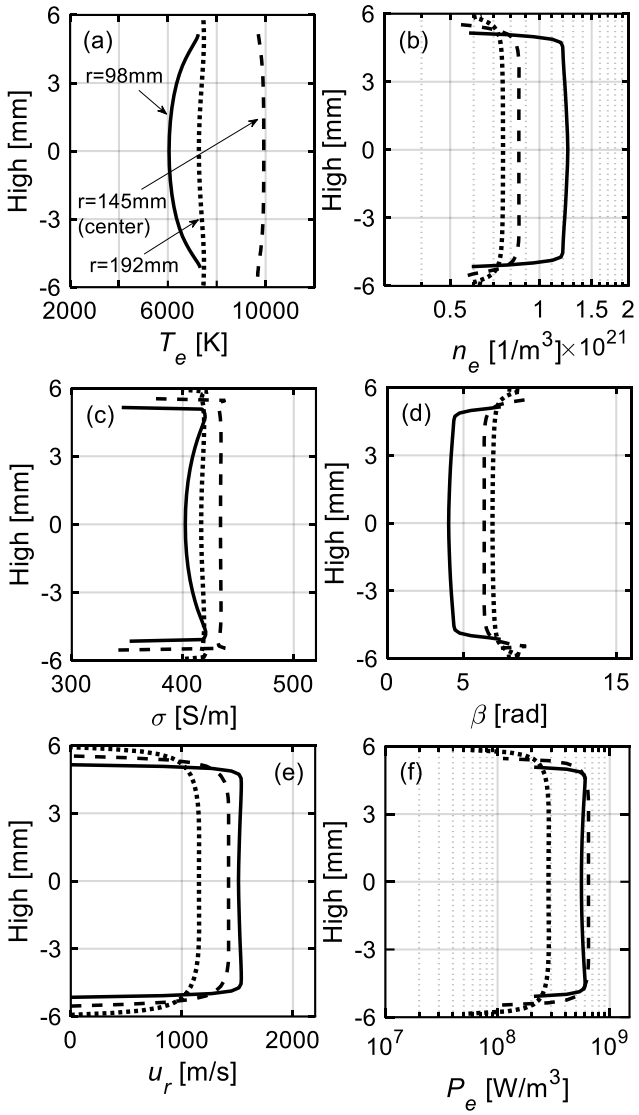

Fig. 3.12 Height distributions of (a) electron temperature, (b) electron number density, (c) electrical conductivity, (d) Hall parameter, (e) flow velocity, and (f) electrical power output density obtained in the *r-z* numerical simulation at an optimum load resistance of 0.31 Ω under a seed fraction of 0.1% and an inlet electron temperature of 8400 K.

Finally, the plasma uniformity is discussed. As shown in chapter 2 assuming an isentropic gas flow and a non-MHD interaction, a uniform plasma is maintained when the characteristic time of the electron number density is longer than the residence time of the working gas. Fig. 3.13 shows the characteristic time of electron number density as a function of electron temperature under a seed fraction of 0.10%. The characteristic times are calculated for two different ionization degrees. One is a typical scenario under the minimum ionization degree at a low load resistance

of 0.10 Ω, and the other is an extreme scenario under the maximum ionization degree at an appropriate load resistance of 0.38 Ω. The horizontal dotted line and dash-dotted line indicate the residence time of the working gas at these respective load resistances. In the electron temperature region where the characteristic time is longer than the residence time, the uniform plasma can be maintained. From the figure, it can be seen that the range of electron temperatures for maintaining a uniform plasma is approximately 5000 – 14000 K. Fig. 3.14 shows radial distributions of electron temperature (at θ = 0 deg) at different load resistances under a seed fraction of 0.10% and an inlet electron temperature of 8400 K as obtained from the r-θ numerical simulation. At load resistances of 0.38 Ω or below, the electron temperature in the generator channel is roughly in the range of 5400–13000 K. In this electron temperature region, the characteristic time is longer than the residence time and thus the uniform plasma is maintained as shown in Fig. 3.10. At an excessively high load resistance (0.39 Ω), on the other hand, the electron temperature is elevated greatly to 18000 K. Under this electron temperature region, the characteristic time becomes shorter than the residence time, and a nonuniform plasma appears as shown in Fig. 3.10. Thus, the insight about plasma uniformity from chapter 2 is also applicable even when the MHD interaction is taken into account.

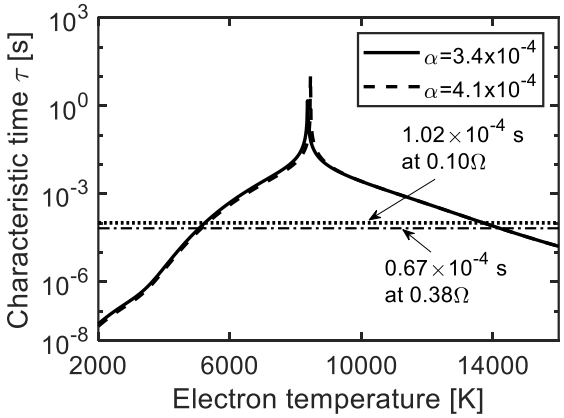

Fig. 3.13 Characteristic time of the electron number density as a function of electron temperature.

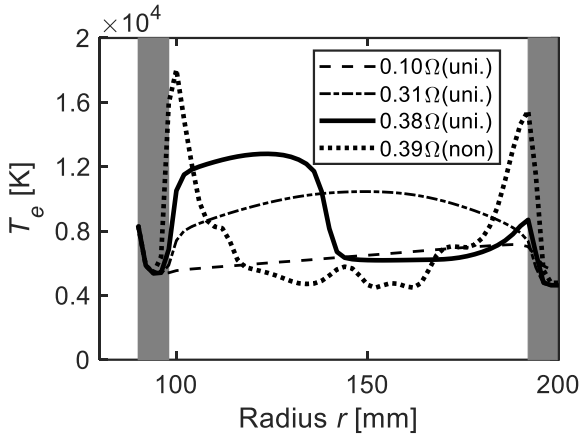

Fig. 3.14 Radial distributions of electron temperature at different load resistance under a seed fraction of 0.10% and an inlet electron temperature of 8400 K (at $\theta = 0$ deg) obtained from the *r*-θ numerical simulation.

3.5 Summary of chapter 3

In this chapter, the power generator performance with Xe-seeded Ar (Ar/Xe), Xe-seeded Ne (Ne/Xe), and Xe-seeded He (He/Xe) has been examined by taking an MHD interaction into account using r-z 2-D numerical simulation. The seed fraction (mole percent of Xe) was varied from 0.0% (i.e., pure Ar, pure Ne, pure He) to 100.0% (pure Xe) in order to clarity the effect of Xe on the performance. The performance with Ne/Xe working gas has been examined using r-θ 2-D numerical simulation, and compared with the results from r-z simulation in order to evaluate the generator performance more precisely including the effects of boundary layer and plasma uniformity. The followings conclusion can be drawn.

(1) For pure Ne, the highest enthalpy extraction ratio and isentropic efficiency are obtained among pure Xe, Ar, Ne, and He working gases. At that time, the required (optimum) inlet electron temperature in Ne is higher than that in Xe and Ar, but the pre-ionization power ratio (ratio of pre-ionization power to thermal input) is smaller.

(2) Adding small amounts of Xe (around 0.01–1.0 mol%) to the Ar, Ne, He can reduce pre-ionization power ratio with keeping the generator performance the same. Particularly, among Ar/Xe, Ne/Xe, and He/Xe, Ne/Xe provides the highest generator performance, and at seed fractions around 0.05–1.0%, the pre-ionization power and pre-ionization power ratio decrease to about 60% of those for pure Ne. Adding excessively amounts of Xe, however, deteriorates the performance. These are attributed to a relatively small atomic weight of Ne, a small

collision cross section of Ne atom with electron, a low ionization potential of Xe, and a large atomic weight of Xe and a large collision cross section of Xe atom with electron.

(3) Under condition at which the uniform plasma structure is achieved, the plasma and fluid flow properties including electron temperature, electrical conductivity, Hall parameter, and radial flow velocity obtained in r-θ simulation are almost the same to those obtained in r-z simulation. At that time, the enthalpy extraction ratio and isentropic efficiency obtained in r-z and r-θ simulations are almost similar with a difference within 1.0 %point. Generator performance is slightly lower in the r-z simulation than that in the r-θ simulation because of the flow velocity decrease in the boundary layer near the wall.

(4) In r - θ simulation, when a nonuniform plasma appears, the generator performance deteriorates drastically and becomes much lower than that in r-z simulation.

Chapter 4 Fundamental Experiment and Numerical Simulation of Xenon-Seeded Noble Gas Plasma MHD Power Generation

4.1 Introduction and objectives

In chapter 2, the plasma behavior of Xe-seeded noble gas plasma was examined by r-θ two-dimensional numerical simulation without taking the MHD interaction into account. In chapter 3, the performance of Xe-seeded noble gas plasma MHD generator was examined using two-dimensional numerical simulations by taking the MHD into account. It was shown that seeding appropriate amounts (around 0.05 – 1.0%) of Xe can reduce the pre-ionization power ratio while maintaining high generator performance, and that Ne/Xe provides the highest generator performance. However, it is necessary to conduct actually the power generation experiment using Ne/Xe as the working gas, and to discuss the features of power generation performance in Ne/Xe plasma based on the experimental results.

In this chapter, the MHD electrical power generation experiment is carried out using pure Ar and Ne seeded with Xe (Ne/Xe) working gases in a shock-tube facility. Then, the plasma behavior and power generation characteristics are examined using time-dependent r-θ two-dimensional numerical simulations based on the experimental generator and conditions. The generator performance and plasma behavior in both the experiments and simulations are discussed and compared so that guidelines can be developed for improving the experimental generator performance. First, the experiment and numerical simulation with pure Ar working gas are carried out for comparison with Ne/Xe working gas (section 4.3), followed by the experiment and numerical simulation with Ne/Xe working gas (section 4.4).

4.2 Experimental and numerical procedures

4.2.1 Experimental setup

Fig. 4.1 shows the experimental set-up, comprising a shock tube, a disk-shaped MHD generator, a superconducting magnet, a radio frequency (RF) power supply, and a dump tank.

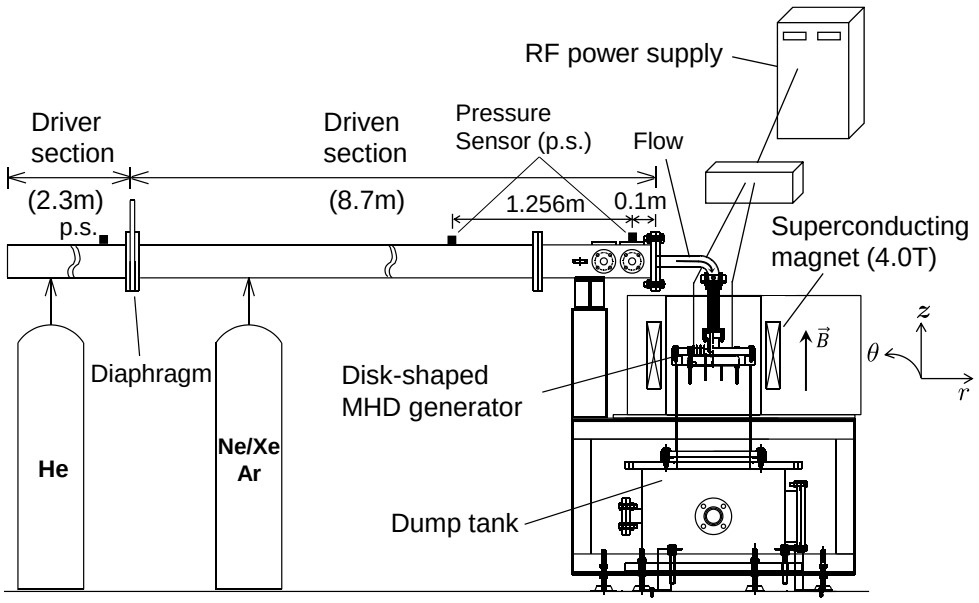

Fig. 4.1 Experimental setup.

a) Shock tube

The shock tube is made of SUS304 and has an inner diameter of 130 mm. An aluminum diaphragm separates the shock tube into a 2.3 m driver section and an 8.7 m driven section. In the present experiments, the driver section is filled with helium (He), and the driven section is filled with Ne/Xe mixture with the seed fractions (mole percent of Xe) of 0.1%, 1.0%, and 5.0%, and pure Ar. The pressure difference between the driver and driven sections naturally ruptures the diaphragm, and simultaneously a shock wave is generated, producing high-temperature high-pressure working gas at the end of the shock tube. The gas pressure and temperature at the end of the tube are determined by the pressure ratio between the driver section and the driven section. The pressure of the driver section when the diaphragm ruptures is controlled by the thickness of the diaphragm and the depth of the score, and the actual rupture pressure is in the range from 0.27 MPa to 0.28 MPa with well repeatability for all the experiments. The hot working gas produced at the end of the shock tube flows around the bend (Fig. 4.1) and goes down vertically along the

inflow duct (Figs. 4.1 and 4.2) into the disk MHD generator, and the exhaust gas is eventually evacuated to the dump tank. The working gas flows in the MHD channel during about 10 ms.

b) RF power supply system

The RF power supply consists of a pulsed RF power source (13.56 MHz), a matching circuit, and an RF induction coil. The maximum power of the RF power source is 10 kW, and the maximum duration time is 3 ms. The RF input power supplied to the induction coil is defined as the difference between the forward power and the reflected power. The matching circuit has two variable capacitors, and can decrease the reflected power. The forward power and reflected power both have the accuracy within ±3%. Because the duration time of the power generation is on the order of milliseconds in the shock-tube facility, however, it is impossible to optimize the matching by changing the capacitance during the plasma flow in the generator. Therefore, we set the matching beforehand without the gas flow for the gas pressure corresponding to the atomic number density that is estimated from the pressure and temperature during the power generation.

c) Disk-shaped MHD Generator

The top and the cross-sectional views of the disk-shaped MHD generator in cylindrical coordinates (r, θ, z) are shown in Fig. 4.2. The MHD generator is placed inside the cylindrical bore of a superconducting magnet (inner diameter of 400 mm). The magnetic flux densities are 4.00 T at the center (r = 0 mm) and 4.26 T at the upstream edge of the cathode (r = 90 mm), which can be recognized as almost the uniform. The generator is composed of a pair of disks between which the working gas flows in the r-direction. The upper disk is made of acrylic and has a cathode (r = 90–110 mm) and an optical port (r = 62.5 mm). The lower disk is made of Bakelite and has an anode (r = 30–35 mm), a cathode (r = 90–110 mm), and an inlet pressure port at the center. Both anode and cathode are made of stainless-steel. The anode is segmented into three parts in circumferential direction to suppress the loss due to the induced RF electromagnetic field. The generator channel length between the downstream edge (the right end) of anode and the upstream edge (the left end) of cathode is 65 mm. A four-turn RF induction coil is embedded in the upper disk at the upstream region of the generator channel for ionizing working gas.

Two MHD generators with different locations of the RF induction coil are used for carrying out experiments with pure Ar working gas and Ne/Xe working gas. Fig. 4.3 shows the enlarged cross-sectional views of disk-shaped MHD generator. A generator at which the RF induction coil is placed in the subsonic-supersonic region (Subsonic-Supersonic generator), is utilized for experiment with pure Ar working gas (Fig. 4.3a). This Subsonic-Supersonic generator has a throat radius of 26 mm, throat height of 2 mm. The other one generator at which the RF induction coil

is placed in the supersonic region (Supersonic generator), is utilized for experiment with Ne/Xe working gas (Fig. 4.3b). This Supersonic generator has a throat radius of 20 mm, throat height of 3 mm.

After the working gas enters the nozzle of the MHD generator from the inflow duct, it accelerates to supersonic flow and at the same time it is pre-ionized by the RF induction coil; consequently, plasma with velocity $\vec{u}$ flows in the MHD generator channel in r-direction where the magnetic flux density $\vec{B}$ is applied in z-direction perpendicular to the flow of the plasma (Figs. 4.2 and 4.3). Then, the output power originating from the Hall electromotive force induced in the r-direction is extracted from the load resistance connected between the ring-shaped anode and cathode located at upstream and downstream, respectively, in the generator channel.

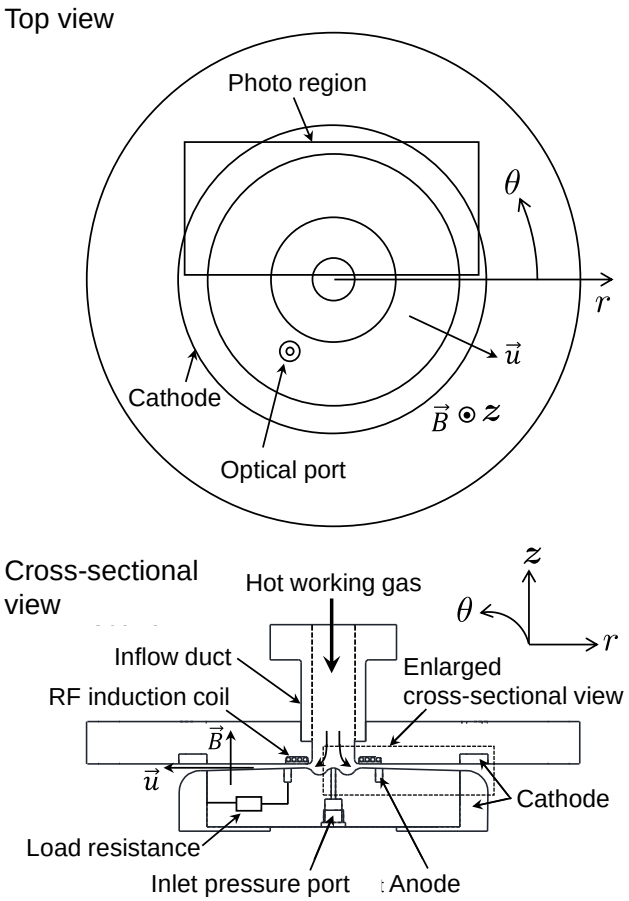

Fig. 4.2 Experimental disk-shaped MHD generator.

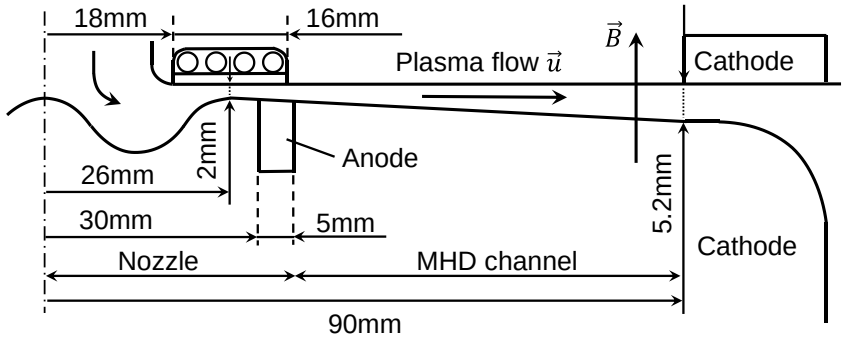

(a) Subsonic-Supersonic generator with a 2-mm-high throat for **experiment with Ar working gas** (section 4.3).

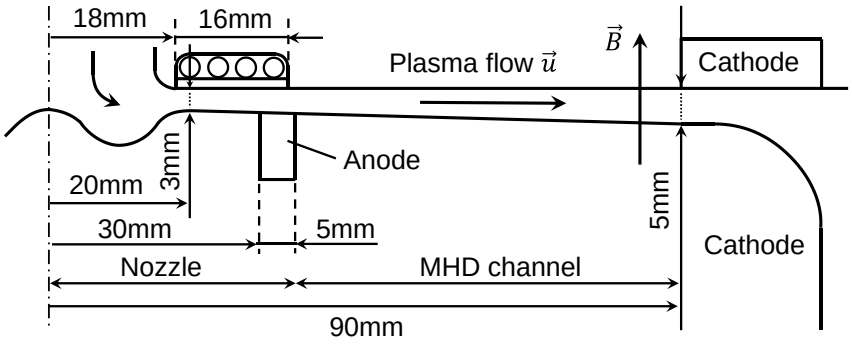

(b) Supersonic generator with a 3-mm-high throat for **experiment with Ne/Xe working gas** (section 4.4).

Fig. 4.3 Enlarged cross-sectional views of disk-shaped MHD generator.

d) Measurement method

Pressure and temperature measurement

There are 3 pressure sensors for pressure measurement in the shock tube, one is in the driver section located at 1.65 m from the left edge of the shock tube and the other two sensors are in the driven section which locates at 0.1 m and 1.356 m from the end (right edge) of the tube as shown in Fig. 4.1. The shock wave propagation speed is obtained from the distance of the two sensors in the driven section and the time which the shock propagates in that distance. The inlet total pressure $p_{0,in}$ is measured by the pressure sensor at the center of the lower disk (the inlet pressure port) which is the stagnation region (Fig. 4.2).

For the total temperature at generator inlet $T_{0,in}$, since we cannot measure it directly, it is determined as follows.

$$T_{0,in} = T_{0,end} \cdot \left(\frac{p_{0,in}}{p_{0,end}} \right)^{\frac{\gamma-1}{\gamma}} \tag{4.1}$$

where $T_{0,end}$ and $p_{0,end}$ are the total temperature and total pressure at the end (right edge) of the shock tube (Fig. 4.1), which can be calculated by the following expressions [53], [54].

$$\frac{T_{0,end}}{T_1} = \frac{[2(\gamma-1)M_s^2 + (3-\gamma)][(3\gamma-1)M_s^2 - 2(\gamma-1)]}{(\gamma+1)^2 M_s^2} \tag{4.2}$$

$$\frac{p_{0,end}}{p_1} = \left[\frac{2\gamma M_s^2 - (\gamma-1)}{\gamma+1}\right]\left[\frac{(3\gamma-1)M_s^2 - 2(\gamma-1)}{(\gamma-1)M_s^2 + 2}\right] \tag{4.3}$$

Here, T_1 is the initial temperature of the gas at the driven section (300 K), p_1 is the initial pressure at the driven section. M_s is the shock wave Mach number calculated from the shock wave propagation speed and sound speed ($\sqrt{\gamma R_s T_1}$).

The initial pressures in the driven section for pure Ar is 2.3 kPa and that for Ne/Xe at seed fractions of 0.1%, 1.0% and 5.0% are 1.5 kPa, 1.5 kPa and 1.9 kPa, respectively, which generate almost the same inlet total pressure and temperature under the fixed rupture pressure in the driver section.

Output voltage and current measurements

The output voltage between the anode and cathode is measured with a voltage probe. The output current flowing in the load resistance is measured with a current probe.

Plasma structure and behavior observations

The plasma emission intensity is measured at the optical port using an optical fiber and a photomultiplier tube (Fig. 2). The spectral wavelengths of the optical filters for Ne/Xe and pure Ar are 640.2 nm (Ne, 3s–3p) and 706.7 nm (Ar, 4s–4p), respectively. A high-speed video camera with a resolution of 128 × 64, a frame rate of 220472 fps (4.54 μs/frame), a focus number of 4.0, an exposure time of 1 μs, and no optical filter is used to observe the plasma. This camera can capture the light emission from the plasma through the upper disk made of transparent acrylic (Fig. 4.2) and can detect the plasma structure and behavior.

4.2.2 Experimental conditions

Table 4.1 and Table 4.2 shows the conditions for the experiment with Ar working gas using a Subsonic-Supersonic generator with 2-mm-high throat, and for the experiment with Ne/Xe working gas using a Supersonic generator with 3-mm-high throat, respectively. In the experiment with Ne/Xe working gas, the seed fraction (mole percent of Xe) is varied from 0.1%, 1.0%, and 5.0%, and the pure Ar working gas is also included for comparison. In both generators, the power generation experiments are performed by changing the RF input power and the load resistance at a fixed inlet total pressure of 0.10 (±0.01) MPa, an inlet total temperature of 2400 (±100) K and a magnetic flux density of 4.0 T at the bore center. Here, the inlet total temperature is determined using the measured inlet total pressure, the initial temperature (300 K), the initial pressure and the

shock Mach number in the driven section since we cannot measure it directly (see section 4.2.1d). The Mach numbers at the inlet of Subsonic-Supersonic generator and Supersonic generator are 2.11 and 2.40, respectively, obtained under the assumption that the Mach number at the throat is unity.

Using the isentropic relation, the static pressure and static temperature at the inlet of Subsonic-Supersonic generator are 10.2 kPa and 960 K, respectively, and those at the inlet of Supersonic generator are 6.85 kPa and 820 K, respectively. The velocity at the inlet of Subsonic-Supersonic generator is 1220 m/s. The velocities at the inlet of Supersonic generator are 1800 m/s, 1750 m/s, 1600 m/s for Ne/Xe at seed fractions of 0.1%, 1.0%, 5.0%, and 1280 m/s for pure Ar.

The enthalpy extraction ratio, which is an important performance index of the generator, has the maximum value against the load resistance. Therefore, the maximum enthalpy extraction ratio at the optimum load resistance at a given RF input power is subject to discussion.

Table 4.1 Experimental conditions in the Subsonic-Supersonic generator (section 4.3)

Working gas		Ar
Thermal input	[kW]	41.9±0.9
Inlet total pressure	[MPa]	0.1±0.01
Inlet total temperature	[K]	2400±100
Inlet Mach number	[–]	2.11
Magnetic flux density	[T]	4.0
Load resistance	[Ω]	10.0 – 100.0
RF input power	[kW]	1.9 – 6.1

Table 4.2 Experimental conditions in the Supersonic generator (section 4.4).

Working gas		Ne/Xe			Ar
Seed fraction	[%]	0.1	1.0	5.0	–
Thermal input	[kW]	67.9±1.5	66.3±1.4	60.3±1.3	48.4±1.0
Inlet total pressure	[MPa]	0.1±0.01			
Inlet total temperature	[K]	2400±100			
Inlet Mach number	[–]	2.40			
Magnetic flux density	[T]	4.0			
Load resistance	[Ω]	5.0 – 30.0			
RF input power	[kW]	3.0 – 7.5			

4.2.3 Numerical region and conditions

The governing equations and numerical procedures used in this simulation are shown in section 3.2 of chapter 3.

The numerical region is in r-θ plane, and from downstream edge of anode (r = 35 mm) to upstream edge of cathode (r = 90 mm) in r-direction and from 0 to 2π in θ-direction (Fig. 4.2). There are 50 cells in r-direction and 360 cells in θ-direction. The cell sizes in r- and θ-direction are Δr = 1.1 mm and $\Delta\theta = \pi/180$, respectively. A mesh refinement study was also conducted to verify accuracy and reliability in the numerical results using three types of mesh system including the mesh used in the present study, as will be described in subsection 4.4.2. The working gases are pure Ar and Ne/Xe with the seed fractions (*S.F.*, mole percent of Xe) of 0.1%, 1.0% and 5.0%. The pure Ne is also included for comparison. The inlet total pressure and inlet total temperature are the same to experimental conditions. The applied magnetic flux density is assumed to hold in z-direction only and to be constant (4.0 T) throughout the generator.

In the numerical simulation, the inlet electron temperature ($T_{e\text{-}in}$, 5400–12000 K) and load resistance (R_L, 0.01–150.0 Ω) are varied, then the output voltage, current and enthalpy extraction ratio are calculated, and the plasma behavior and power generation characteristic are clarified. It should be noted that the power generation characteristic is dominated by inlet ionization degree (inlet electron number density/inlet atomic number density before ionization) rather than by inlet electron temperature, since the characteristic time of ionization degree is longer than that of electron temperature, so we show the inlet electron temperature together with the inlet ionization degree in the following section.

In the numerical simulation, the enthalpy extraction ratio *E.E.R.* is defined as the ratio of the output power to the thermal input Q_{in} [Eq. (4.4)], a sum of thermal input of heavy particle Q_{in-h} [Eq. (4.5)] and thermal input of electron Q_{in-e} [Eq. (4.6)]. However, in the experiment the enthalpy extraction ratio is evaluated using thermal input of heavy particles since we cannot measure the electron temperature and electron number density at generator inlet. Since the thermal input of electron is relatively small, the difference in enthalpy extraction ratio due to the different evaluation of thermal input is small. The pre-ionization power *P.P.* is the net power used for plasma production (in physical meaning, it is the inflow energy of electron at generator inlet) and is the same to the thermal input of electron here [Eq. (4.6)]. The pre-ionization power ratio *P.P.R.* [Eq. (4.7)] is defined as the ratio of pre-ionization power to the thermal input. It should be noted here that pre-ionization power is not the RF input power which is the actual power flowing into the RF induction coil, and the RF input power ratio *R.P.R.* [Eq. (4.8)] is defined as the ratio of RF input power to the thermal input (of heavy particle) in the experiment.

$$Q_{in} = Q_{in-h} + Q_{in-e} \tag{4.4}$$

$$Q_{in-h} = \left[\rho_g \left(c_v T_g + \frac{1}{2}|\vec{u}|^2\right) + p_g\right] u_r A_{in} \tag{4.5}$$

$$Q_{in-e} = P.P. = \left(\frac{3}{2} n_e k T_e + \sum_i \epsilon_i n_i + p_e\right) u_r A_{in} \tag{4.6}$$

$$P.P.R. = \frac{P.P.}{Q_{in}} \tag{4.7}$$

$$R.P.R. = \frac{\text{RF input power}}{Q_{in-h}} \tag{4.8}$$

4.3 Experiment and numerical simulation of Ar plasma MHD power generation

In this section, power generation experiment and r-θ 2-D numerical simulation are conducted with Ar working gas. The experiment is carried out using a Subsonic-Supersonic generator with 2-mm-high throat (Fig. 4.3a) under the conditions as shown in Table 4.1. The simulation is carried out based on the experimental conditions and experimental generator.

First, the experimental results will be described, after which the numerical results are discussed and compared with those from the experiment.

4.3.1 Representative experimental results

Fig. 4.4 shows the time variations of (a) the radio-frequency (RF) input power, (b) the plasma emission intensity, (c) the output voltage, (d) the output current, and (e) the output power (=output voltage×output current) obtained in the experiment with Ar working gas at an RF input power of 5.91 kW and a load resistance of 13.0 Ω. The time at 0 ms corresponds to the time of the pressure rise at the end of the shock tube. The gray region in the figure depicts the test time of 3.2–3.5 ms, the time during which the nominal working gas conditions can be precisely obtained. As shown in Fig. 4.4a, the RF input power is supplied to the induction coil for 2 ms during 2.5–4.5 ms after the operation of the shock tube. The plasma emission intensity (Fig. 4.4b), the output voltage (Fig. 4.4c), and the output current (Fig. 4.4d) rise only during the period when the RF input power is supplied.

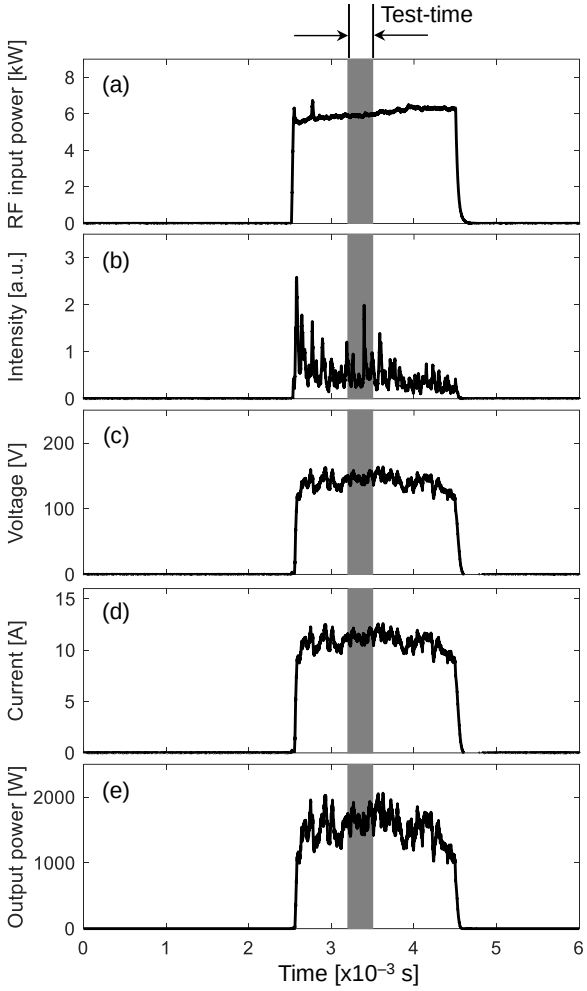

Fig. 4.4 Time variations of (a) RF input power, (b) plasma emission intensity, (c) output voltage, (d) output current, and (e) output power, obtained in the experiment with Ar working gas at an RF input power of 5.91 kW and a load resistance of 13.0 Ω.

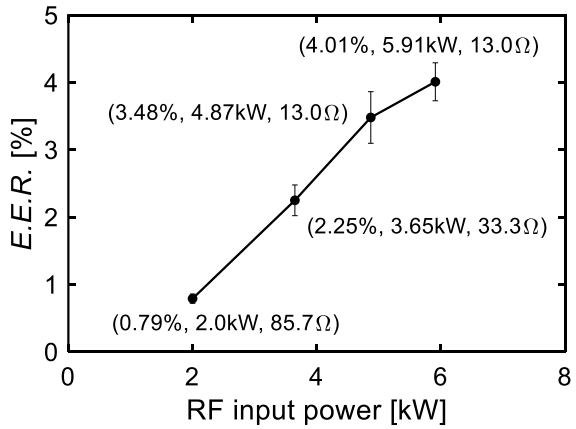

Fig. 4.5 Enthalpy extraction ratio against RF input power obtained in the experiment with Ar working gas.

Fig. 4.5 shows the enthalpy extraction ratio, *E.E.R.* (the average value at the test time in Fig. 4.4), plotted against the RF input power. As shown in the figure, the enthalpy extraction ratio increases with increasing RF input power. This is attributed to the increases in the inlet electron temperature, inlet electron number density, and electrical conductivity in the generator channel as the RF input power increases. The maximum *E.E.R.* of 4.01% is obtained at an RF input power of 5.91 kW (RF input power ratio of 14.3%) and a load resistance of 13.0 Ω.

4.3.2 Representative numerical results

Fig. 4.6 shows the enthalpy extraction ratio *E.E.R.* against the inlet electron temperature, and Table 4.3 shows the generator performance at optimum load resistance under each inlet electron temperature, obtained by numerical simulation with Ar working gas. The α_{in} in Table 4.3 is the inlet ionization degree (= inlet electron number density/Ar atomic number density of 7.68×10^{23} m^{-3}). It should be noted that the results presented here are time-averaged over a period of about 1×10^{-3} s of the last part of the output result during which the periodic state is reached. As can be seen from Fig. 4.6 and Table 4.3, at low inlet electron temperature region the enthalpy extraction ratio increases with increasing inlet electron temperature; at an inlet electron temperature of 7000 K (corresponding to an inlet ionization degree of 3.15×10^{-4}) the *E.E.R.* exceeds 10%, at 7200 K (4.64×10^{-4}) – 8000 K (1.79×10^{-3}) the *E.E.E.* reaches 13 – 15%. A maximum *E.E.R.* of 15.0% is obtained at 7600 K (9.40×10^{-4}). However, at higher inlet electron temperatures, particularly at the inlet electron temperatures over 8200 K (2.40×10^{-3}), the *E.E.R.* decreases. Consequently, there exits an optimal inlet electron temperature (inlet ionization degree) for providing the maximum enthalpy extraction ratio.

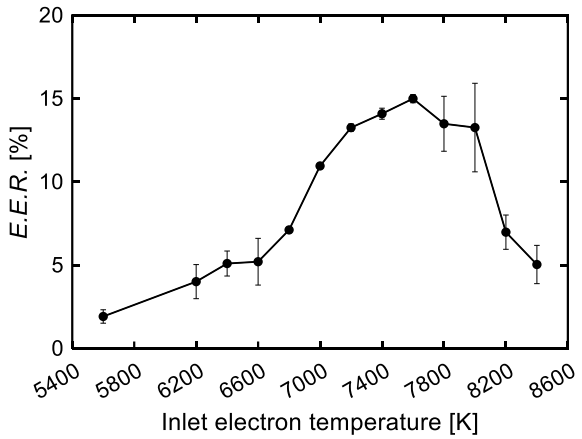

Fig. 4.6 Enthalpy extraction ratio against inlet electron temperature obtained by numerical simulation with Ar working gas.

Table 4.3 Generator performance at optimum load resistance under various inlet electron temperatures in simulations with Ar working gas

$T_{e\text{-}in}$ [K]	5600	6200	6400	6600	6800	7000	7200	7400	7600	7800	8000	8200	8400
$\alpha_{in} \times 10^{-4}$ [–]	0.10	0.53	0.86	1.36	2.10	3.15	4.64	6.66	9.40	13.1	17.9	24.0	31.8
Q_{in} [kW]	41.9	42.0	42.0	42.1	42.2	42.4	42.6	42.9	43.2	43.8	44.4	45.3	46.4
P.P. [kW]	0.01	0.07	0.12	0.19	0.29	0.44	0.65	0.94	1.33	1.85	2.53	3.42	4.55
P.P.R. [%]	0.03	0.18	0.29	0.45	0.70	1.04	1.53	2.19	3.07	4.22	5.70	7.54	9.79
R_L [Ω]	10.0	6.00	3.00	1.40	10.0	7.00	4.00	2.10	0.90	2.20	1.20	1.80	1.40
P_{out} [kW]	0.81	1.69	2.15	2.19	3.01	4.64	5.64	6.04	6.49	5.90	5.90	3.17	2.34
E.E.R. [%]	1.93	4.02	5.10	5.21	7.12	11.0	13.3	14.1	15.0	13.5	13.3	6.99	5.04
(P_{out} / $Q_{in\text{-}h}$)	(1.93)	(4.02)	(5.12)	(5.24)	(7.17)	(11.1)	(13.5)	(14.4)	(15.5)	(14.1)	(14.1)	(7.56)	(5.59)
I.E. [%]	4.02	7.63	9.89	10.3	13.1	19.9	23.7	25.3	27.0	24.9	25.3	12.4	8.98

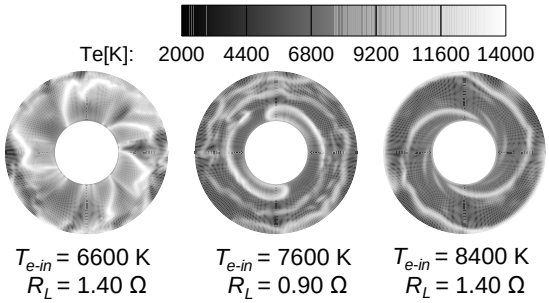

Fig. 4.7 Electron temperature distributions at low, optimum and high inlet electron temperatures.

Fig. 4.7 shows the distributions of electron temperature (plasma structure) in the generator channel at optimum load resistance under a low inlet electron temperature of 6600 K (α_{in} = 1.36×10^{-4}), an optimum inlet electron temperature of 7600 K (9.40×10^{-4}), and a high inlet electron temperature of 8400 K (3.18×10^{-3}). As shown in the figure, at low inlet electron temperature a radially expanding spoke-like nonuniform structure, at optimum inlet electron temperature a nonuniform spiral structure rotating counter clockwise, and at high inlet electron temperature a nonuniform spiral structure rotating clockwise, occur. Namely, nonuniform plasma structure occurs even at optimum inlet electron temperature.

As shown in chapter 2 and chapter 3, when the characteristic time of electron number density is shorter than the residence time of the working gas, a duration time for the working gas passes through the generator channel, the uniform plasma cannot be maintained and becomes nonuniform in the generator channel. The characteristic time of electron number density as a

function of electron temperature is shown in Fig. 4.8. As shown in the figure, the range of electron temperature for maintaining uniform plasma structure is approximately 5000 – 9500 K. However, as shown in Fig. 4.7, the electron temperature in the generator channel is varied from 3500 – 14000 K, at the low or high electron temperature region the characteristic time becomes short which causes a nonuniform plasma structure to occur.

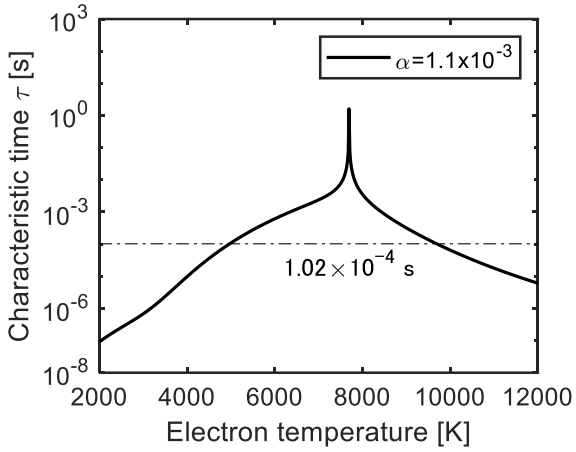

Fig. 4.8 Characteristic time of electron number density as a function of electron temperature. The characteristic time is calculated at an averaged ionization degree in the generator channel. The dashed-dotted line indicates the residence time of the working gas.

Fig. 4.9 shows the radial distributions of (a) electrical conductivity and (b) Hall parameter at optimum load resistance under low, optimum and high inlet electron temperatures. Value is averaged in θ-direction at a time instant. The electron number density at generator inlet increases with increasing inlet electron temperature, resulting in the increase in electrical conductivity (Fig. 4.9a). The Hall parameter (Fig. 4.9b), on the other hand, decreases due to the increase in electron collision frequency which is a result of the increase in ion number density ($=$ electron number density). The low electrical conductivity at low inlet electron temperature and the low Hall parameter at high inlet electron temperature are the factors that lead to the deterioration in enthalpy extraction ratio.

Based on the above discussion, higher inlet electron temperature (inlet ionization degree) is necessary to obtain sufficient electrical conductivity for power generation, but excessively high inlet electron temperature (inlet ionization degree) causes a decline in Hall parameter, thus impairing the generator performance.

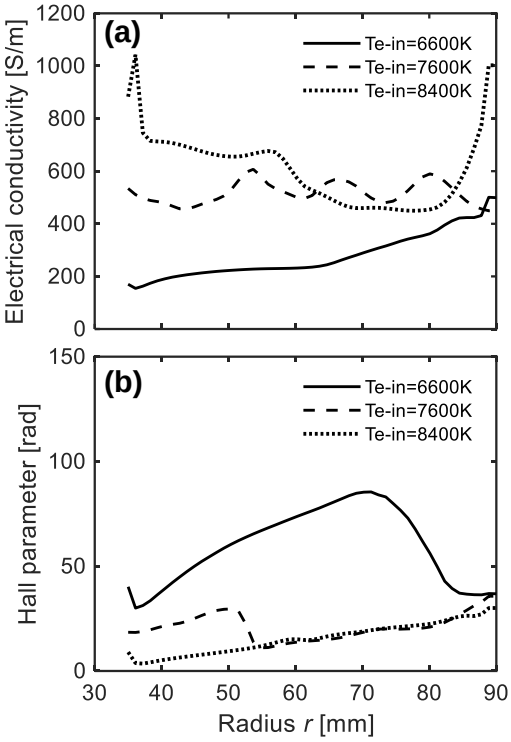

Fig. 4.9 Distributions of (a) electrical conductivity and (b) Hall parameter at low, optimum and high inlet electron temperatures at optimum load resistance. Value is averaged in θ-direction.

4.3.3 Comparison of numerical and experimental results

As shown in Fig. 4.6, the enthalpy extraction ratios obtained by numerical simulation at inlet electron temperature of around 5600 K (α_{in} = 0.10×10^{-4}) – 6600 K (1.36×10^{-4}) and at 8400 K (3.18×10^{-3}) are close to the enthalpy extraction ratio of 4.01% obtained in the experiment. Fig. 4.10 presents plasma structures captured by a high-speed video camera in the experiments and plasma structures (electron temperature distributions) obtained in the numerical simulations at a low inlet electron temperature of 6600 K and a high inlet electron temperature of 8400 K. The load resistance in the simulation is set the same as that in the experiment (13.0 Ω). The white region in the video image from the experiment is the area in which plasma emission is strong, and the electron temperature is thought to be high. Although both (plasma emission and electron temperature) do not always have a linear relationship, in the present simulation the electron temperature was given at the generator inlet, additionally, as mentioned above, this electron temperature is an important parameter to discuss the plasma uniformity; thus, plasma structure was shown in terms of electron temperature distribution. The nonuniform distribution of the white bright color region in the generator indicates that the electron temperature is not uniformly

distributed, saying in other word, the plasma is nonuniform. Fig. 4.10 indicates that the nonuniform plasma observed in the experiment (Fig. 4.10a) is closer to the many-fine-streaked structure at 6600 K (Fig. 4.10b) than to the less-coarse-streaked structure at 8400 K (Fig. 4.10c). In addition, as shown in Table 4.4, the radial plasma flow velocity that estimated from the time evolution of nonuniform structure at a radius of r = 72.5 mm is 955 m/s in the experiment (Fig. 4.10a), 917 m/s in the simulation at low inlet electron temperature of 6600 K (Fig. 4.10b), and 733 m/s in the simulation at high inlet electron temperature of 8400 K (Fig. 4.10c); that is, the plasma flow velocity in the experiment is closer to the simulation at low inlet electron temperature of 6600 K. Furthermore, an increase in RF input power is supposed to boost the inlet electron temperature and electron number density; therefore, it is believed that the experimental results in Fig. 4.5 can be reproduced by the numerical simulation at a low inlet electron temperature of 5600–6600 K. Thus, below the experimental results are compared in more detail with the numerical simulation results at the low inlet electron temperature region.

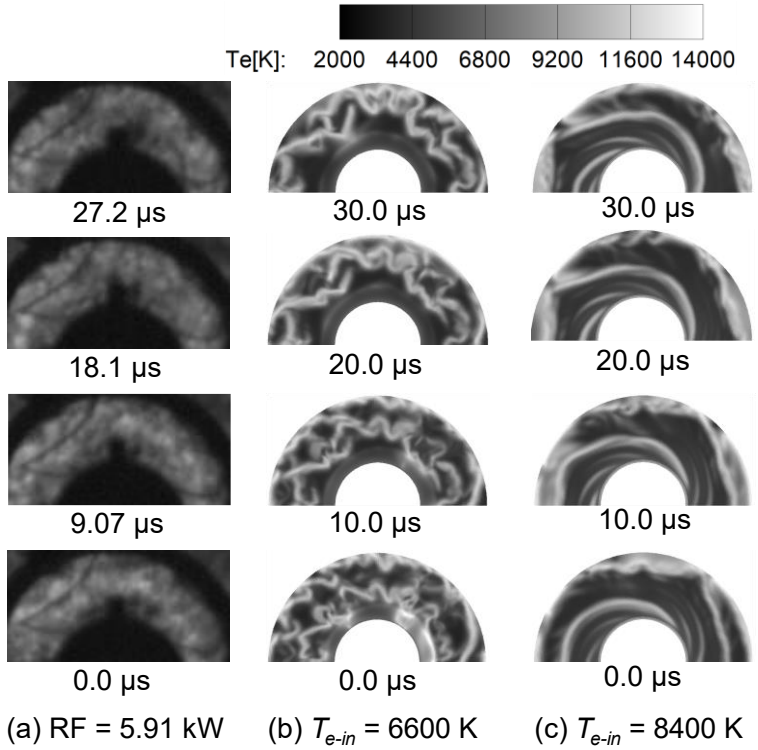

Fig. 4.10 Time evolution of plasma behavior in experiment (a) and electron temperature distribution in numerical simulation (b) and (c) at the same load resistance 13.0 Ω.

Table 4.4 Radial plasma flow velocities estimated from the time evolution of nonuniform structure in the experiment and numerical simulation at a radius of 72.5 mm

	Experiment	Simulation	
	RF power = 5.91 kW	$T_{e\text{-}in}$ = 6600 K	$T_{e\text{-}in}$ = 8400 K
	R_L =13.0 Ω	R_L =13.0 Ω	R_L =13.0 Ω
Plasma flow velocity [m/s]	955	917	733

Fig. 4.11 shows the output voltage-current characteristics obtained in the experiment and numerical simulation. In the figure, variations of output voltage and current are shown by bars. Table 4.5 gives details of the experimental results (Fig. 4.5) and presents numerical simulation results obtained under the inlet electron temperature at which the output power is relatively close to that of the experiment at the experimental load resistance. As can be seen from Fig. 4.11 and Table 4.5, output powers at the RF input powers of 2.0 kW, 3.65 kW, 4.87 kW, and 5.91 kW are close to the numerical simulation results at the assumed inlet electron temperatures of 5600 K (α_{in} = 0.10×10^{-4}), 6200 K (0.530×10^{-4}), 6400 K (0.86×10^{-4}), and 6600 K (1.36×10^{-4}), respectively. In the experiments, the inlet electron temperature and electron number density cannot be measured, whereas in the numerical simulations it is not easy to evaluate the RF input power. Therefore, it is difficult to establish a direct correspondence; however, it is believed that the present numerical simulations can provide a rough explanation of the experimental results. Besides, it is shown from the present study that the experiments were conducted with rather high load resistance, and in the future, it is necessary to carry out the comparative study of the power generation characteristics obtained by the experiment over a wider range of load resistance.

The results of the present numerical simulations suggest that the inlet electron temperature (inlet ionization degree) must be increased [7000 K (α_{in} = 3.15×10^{-4}) or higher] to further improve enthalpy extraction ratio, and also show that under the present experimental conditions and experimental generator, plasma structure in the generator channel will becomes nonuniform even at optimum inlet electron temperatures (7200–8000 K) at which high enthalpy extraction ratio is expected. One can expect higher performance if a uniform plasma structure is realized; thus, in the future, experiments and numerical simulations are necessary toward optimizing generator shape and other parameters for maintaining electron temperature within a proper range in order to improve plasma uniformity. In addition, in order to increase the inlet electron temperature (inlet ionization degree) in the experiment, it is necessary to optimize the arrangement of the RF power transition system; meanwhile, utilizing a dielectric barrier discharge or a nano-second pulse discharge as other possible ways for efficient pre-ionization is also necessary. In other words, just as with alkali metal-seeded plasma [12], [55], [56], the key is to demonstrate that control of plasma inside the generator for improving uniformity and stability is technically possible.

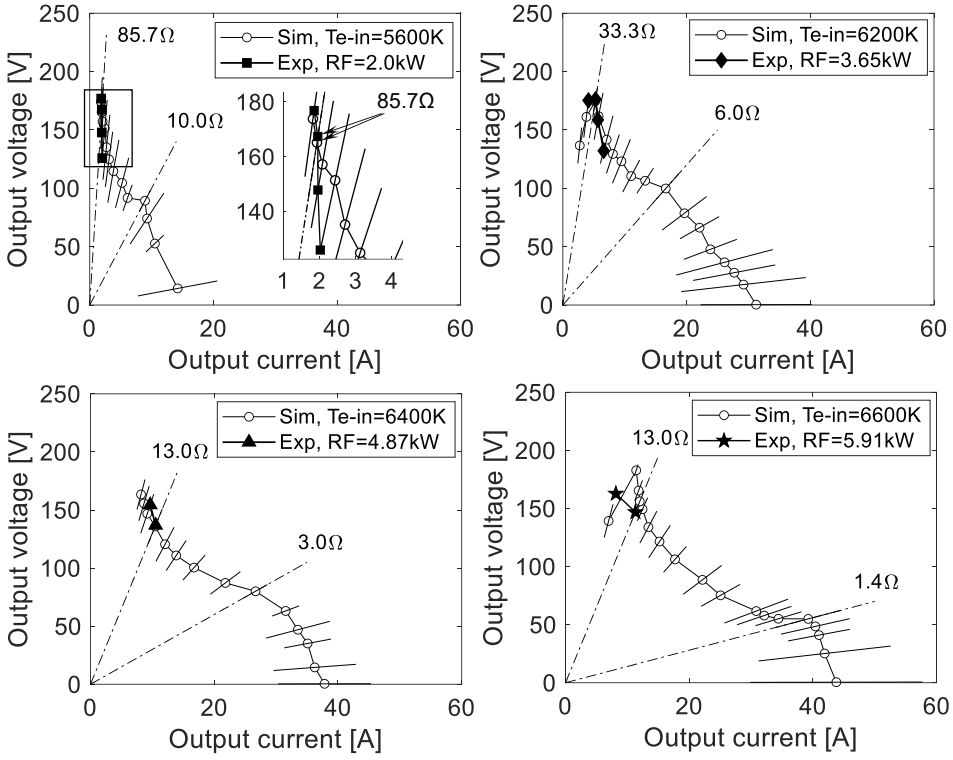

Fig. 4.11 Comparison of output voltage-current characteristics obtained in the experiment and numerical simulation.

Table 4.5 Comparison of generator performance in experiment and numerical simulation. The load resistance in the simulation is chosen the same to that in the experiment

	Experiment (Fig. 4.5)	Simulation
	RF power = 2.0 kW	$T_{e\text{-}in}$ = 5600 K
V_{out} [V] / I_{out} [A] (R_L [Ω])	167.4 / 1.95 (85.7)	165.2 / 1.93 (87.5)
Power output [kW] (*E.E.R.* [%])	0.33 (0.79)	0.32 (0.77)
	RF power = 3.65 kW	$T_{e\text{-}in}$ = 6200 K
V_{out} [V] / I_{out} [A] (R_L [Ω])	176.2 / 5.29 (33.3)	174.7 / 5.25 (33.3)
Power output [kW] (*E.E.R.* [%])	0.93 (2.25)	0.92 (2.19)
	RF power = 4.87 kW	$T_{e\text{-}in}$ = 6400 K
V_{out} [V] / I_{out} [A] (R_L [Ω])	136.9 / 10.5 (13.0)	135.8 / 10.4 (13.0)
Power output [kW] (*E.E.R.* [%])	1.44 (3.48)	1.44 (3.42)
	RF power = 5.91 kW	$T_{e\text{-}in}$ = 6600 K
V_{out} [V] / I_{out} [A] (R_L [Ω])	146.8 / 11.3 (13.0)	156.0 / 12.0 (13.0)
Power output [kW] (*E.E.R.* [%])	1.66 (4.01)	1.88 (4.46)

4.4 Experiment and numerical simulation of Ne/Xe plasma MHD power generation

In this section, power generation experiment and r-θ 2-D numerical simulation are carried out with Ne/Xe working gas. The experiment is carried out using a Supersonic generator with 3-mm-high throat (Fig. 4.3b) under the conditions as shown in Table 4.2. The simulation is carried out based on the experimental conditions and experimental generator.

First, the experimental results will be described, after which the numerical results are discussed and compared with those from the experiment.

4.4.1 Representative experimental results

Fig. 4.12 shows the time variations of (a) the radio-frequency (RF) input power, (b) the plasma emission intensity, (c) the output voltage, (d) the output current, (e) the output power, and (f) the load resistance estimated from (output voltage/output current) for a seed fraction of 5.0% at an RF input power ratio of 11.4% and a load resistance of 5.67 Ω. The time at 0 ms corresponds to the time of the pressure rise at the end of the shock tube. As shown in Fig. 4.12a, the RF input power is supplied to the induction coil for 2 ms during 2.7–4.7 ms after the operation of the shock tube. The plasma emission intensity (Fig. 4.12b), the output voltage (Fig. 4.12c), and the output current (Fig. 4.12d) rise only during the period when the RF input power is supplied. During the test time of 3.4–3.7 ms, the time during which the nominal working gas conditions can be precisely obtained, the average output power is 2.97 kW and the estimated load resistance is 5.71 Ω, which is similar to the actual load resistance of 5.67 Ω. Thus, the measured voltage and current are reliable.

Fig. 4.13 shows the enthalpy extraction ratio, *E.E.R.* (the average value at the test time in Fig. 4.12), plotted against the RF input power ratio, *R.P.R.* [Eq. (4.8)], obtained in the experiments under Ne/Xe at different seed fractions and under pure Ar. For any working gas, the enthalpy extraction ratio increases along with the RF input power ratio, which can be attributed to the increases in the inlet electron temperature, inlet electron number density, and electrical conductivity in the generator channel. The enthalpy extraction ratio is about 0.5–2.0% for a seed fraction of 0.1% (*R.P.R.* = 7.68–10.9%), and 3.0–5.0% for seed fractions of 1.0% (*R.P.R.* = 5.88–11.1%) and 5.0% (*R.P.R.* = 7.60–11.4%). The enthalpy extraction ratios at seed fractions of 1.0% and 5.0% are higher than those at 0.1%, which can be due to the increase in electrical conductivity as the seed fraction increases. For pure Ar, on the other hand, an enthalpy extraction ratio of about 3.0–5.0% is obtained at *R.P.R.* = 6.92–12.6%. Thus, the enthalpy extraction ratio for Ne/Xe at seed fractions of 1.0% and 5.0% is almost the same as that for pure Ar. In the higher RF input power ratio region; however, they seem to be higher than in the case of pure Ar for the same RF

input power ratio. The difference between Ne/Xe and Ar is more clearly shown in the numerical simulations below. For pure Ne (*S.F.* = 0.0%), it was hard to produce plasma with enough electrical conductivity for power generation using the current plasma production equipment, probably due to the very high ionization potential of Ne, which prevents us from performing the power generation experiment using pure Ne.

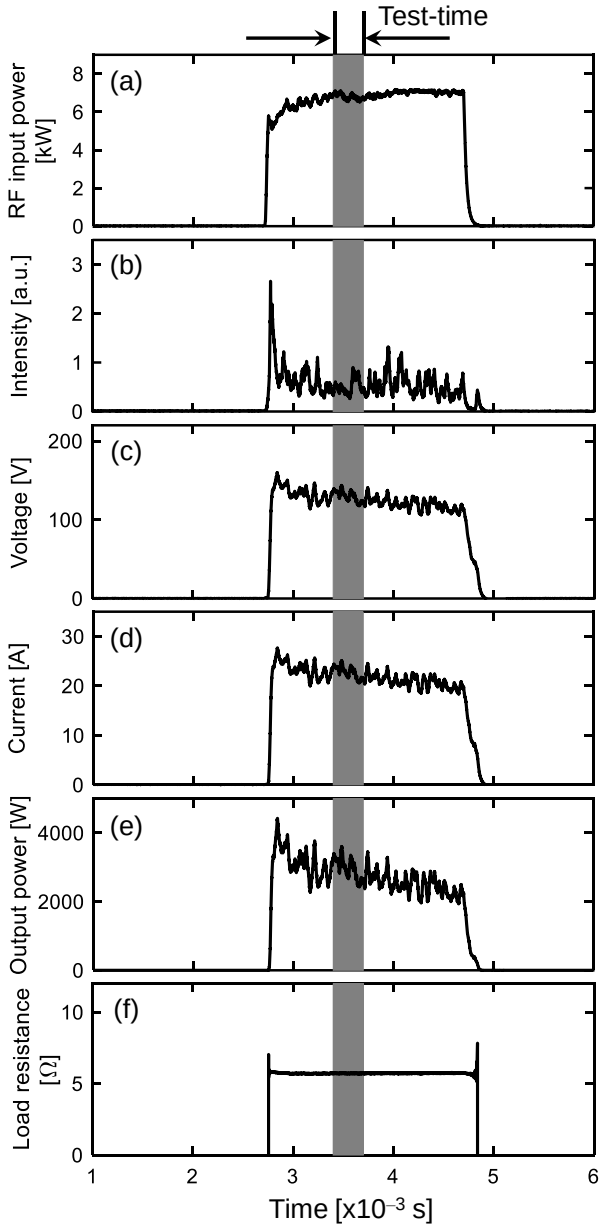

Fig. 4.12 Time variations of (a) RF input power, (b) plasma emission intensity, (c) output voltage, (d) output current, (e) output power, and (f) estimated load resistance obtained in the experiments with Ne/Xe working gas under *S.F.* = 5.0% (*R.P.R.* = 11.4%, R_L = 5.67 Ω).

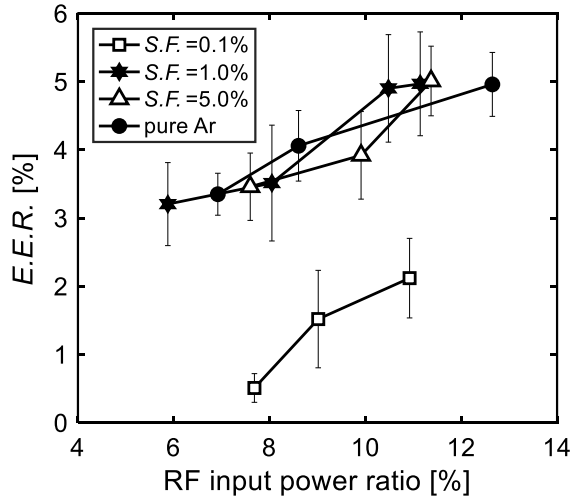

Fig. 4.13 Enthalpy extraction ratio *E.E.R.* against RF input power ratio *R.P.R.* obtained in the experiments with Ne/Xe working gas. Pure Ar is also included for comparison.

4.4.2 Representative numerical results

Fig. 4.14 shows the enthalpy extraction ratio *E.E.R.* plotted against (a) the inlet electron temperature $T_{e\text{-}in}$ and (b) the pre-ionization power ratio *P.P.R.* [Eq. (4.7)] at different seed fractions, the data of which was obtained using numerical simulations. In this figure, the enthalpy extraction ratios for pure Ne and pure Ar are also shown. It is noted that the results presented here (also in Fig. 4.18 of subsection 4.4.3) are time-averaged over a period of about 1×10^{-3} s of the last part of the output result during which the periodic state is reached. As is seen in Figs. 4.14a and 4.14b, the enthalpy extraction ratio increases along with the inlet electron temperature and pre-ionization power ratio for any seed fraction. However, when either of them is excessively high, the enthalpy extraction ratio decreases gradually. Consequently, there exits an optimal inlet electron temperature and pre-ionization power ratio for providing the maximum enthalpy extraction ratio. As the seed fraction increases, the required (optimum) inlet electron temperature decreases rapidly (Fig. 4.14a). This is because a high electrical conductivity can be obtained as the amount of Xe increases, even at a low inlet electron temperature, due to Xe's low ionization potential. It is noted here, however, that the required (optimum) pre-ionization power ratio seems to be only slightly different (Fig. 4.14b), which is a consequence of the non-linear relation between the electron temperature and the pre-ionization power *P.P.* [Eq. (4.6)]. An enthalpy extraction ratio over 20% is obtained for pure Ne (*S.F.* = 0.0%) at an inlet electron temperature $T_{e\text{-}in}$ = 9600–10400 K (corresponding to a pre-ionization power ratio *P.P.R.* = 2.4–8.0%, inlet ionization degree α_{in} = 5.3×10^{-4} – 1.8×10^{-3}), for a seed fraction of 0.1% at $T_{e\text{-}in}$ = 8000–10200 K (*P.P.R.* = 1.3–7.0%, α_{in} = 5×10^{-4} – 2×10^{-3}) and 1.0% at $T_{e\text{-}in}$ = 7000–8000 K (*P.P.R.* = 1.5–5.2%, α_{in} = 5.7×10^{-4} – 2×10^{-3}). For Ne/Xe at a seed fraction of 5.0% and pure Ar, an enthalpy extraction ratio of over 10% is

obtained at $T_{e\text{-}in}$ = 6400–7400 K (*P.P.R.* = 1.2–5.8%, $\alpha_{in} = 4.8\times10^{-4} - 2.3\times10^{-3}$) and $T_{e\text{-}in}$ = 6900–7500 K (*P.P.R.* = 0.9–3.0%, $\alpha_{in} = 3\times10^{-4} - 9\times10^{-4}$), respectively. It is noted in the figure that the enthalpy extraction ratio improves as we add small amounts (around *S.F.* = 0.1–1.0%) of Xe, but adding excessive amounts (over 5.0%) reduces the enthalpy extraction ratio until it becomes lower than that for pure Ar. Furthermore, for Ne/Xe at a seed fraction of 5.0% and pure Ar, the enthalpy extraction ratio seems to be almost the same as that for Ne/Xe at a seed fraction of 0.1–1.0% under a low inlet electron temperature (or low pre-ionization power ratio), but the maximum enthalpy extraction ratio achievable for a higher inlet electron temperature (or higher pre-ionization power) is much lower than that for Ne/Xe at a seed fraction of 0.1–1.0%.

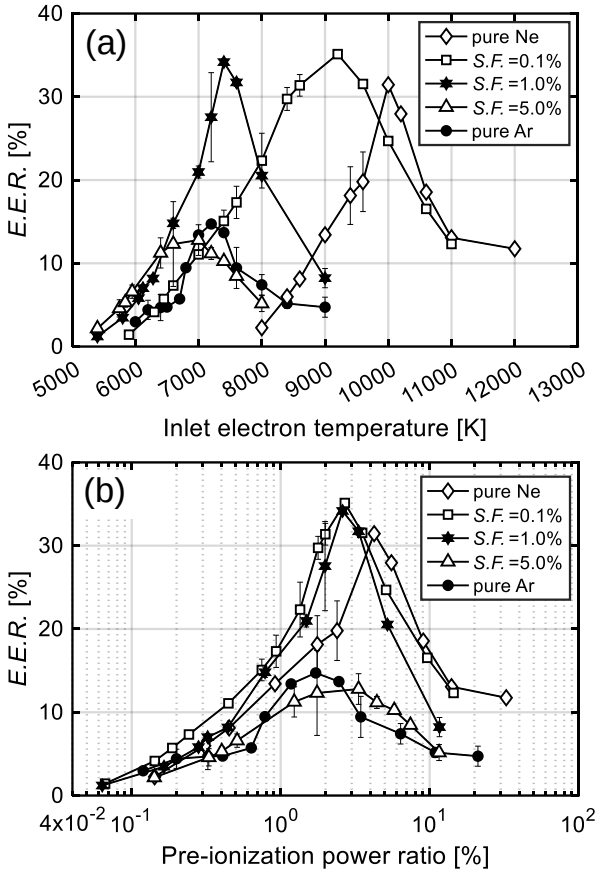

Fig. 4.14 Enthalpy extraction ratio *E.E.R.* against (a) inlet electron temperature $T_{e\text{-}in}$ and (b) pre-ionization power ratio *P.P.R.* obtained by numerical simulation under Ne/Xe working gas. Pure Ne and pure Ar are also included for comparison.

Fig. 4.15 shows the radial distributions of the electron temperature, electron number density, electrical conductivity, and Hall parameter for Ne/Xe, pure Ne, and pure Ar under optimum conditions, at which the maximum enthalpy extraction ratio is obtained. Each value is

circumferentially averaged at a time instant. As we add small amounts (0.1–1.0%) of Xe, the electron temperature is relaxed and slightly lower than that of pure Ne. The electron number density and electrical conductivity are enhanced due to the low ionization potential of Xe, resulting in an increase of the enthalpy extraction ratio. On the other hand, at an excessively high seed fraction (5.0%), the Hall parameter decreases because of the large Coulomb collision frequency ν_{ei} [$= c_e Q_{ei} n_i^+$, Eq. (3.40)] due to the high electron number density (= ion number density), and large elastic collision frequency ν_{en} [$= c_e Q_{en} n_n$, Eq. (3.40)] due to large collision cross section of Xe atoms with electrons. According to the present numerical simulation, under pure Ne, seed fractions of 0.1%, 1.0%, and 5.0%, the spatial average Coulomb collision frequencies are 2.41×10^{10}, 3.29×10^{10}, 3.38×10^{10}, and 4.53×10^{10} Hz, respectively, meanwhile the spatial average elastic collision frequencies are 9.27×10^{9}, 1.13×10^{10}, 1.21×10^{10}, and 1.28×10^{10} Hz, respectively. Both Coulomb collision frequency and elastic collision frequency increase with increasing seed fraction.

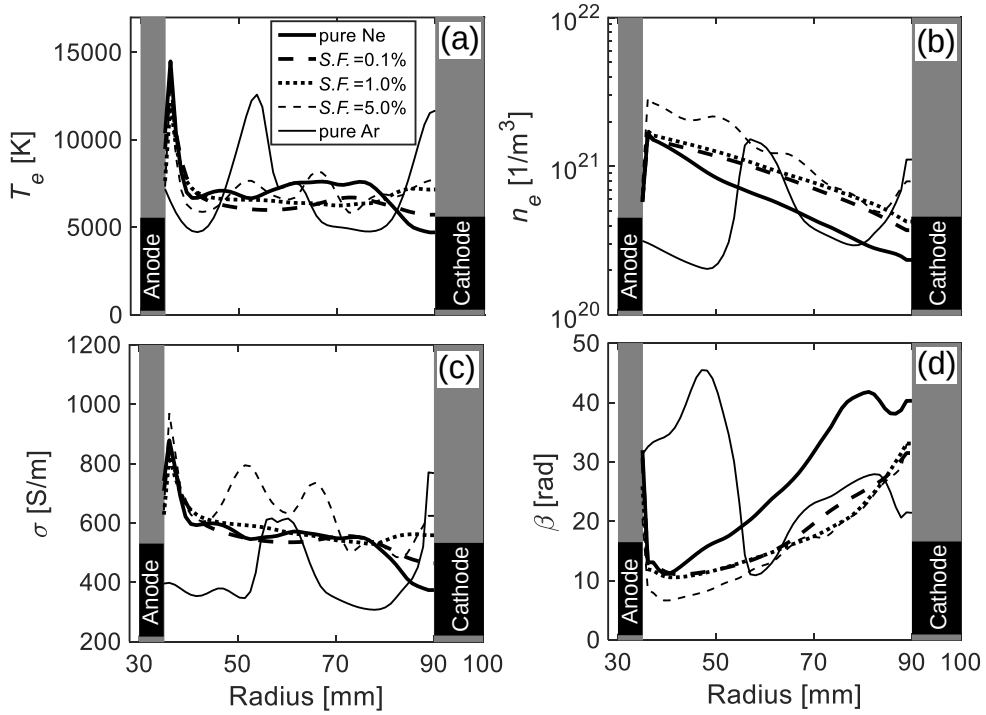

Fig. 4.15 Radial distributions of (a) electron temperature T_e, (b) electron number density n_e, (c) electrical conductivity σ and (d) Hall parameter β.

For pure Ar, although the electron temperature in the generator channel is in the same order to those of Ne/Xe and pure Ne, the electron number density and the electrical conductivity are relatively low because the electron number density supplied at the generator inlet is low. Regardless of the reduced Coulomb collision frequency (spatial average of 1.94×10^{10} Hz, lower

than that of pure Ne of 2.41×10^{10} Hz) due to the low electron (ion) number density, the Hall parameter (spatial average around 27.0 rad) is about the same as that of pure Ne (spatial average around 26.4 rad), a result of the large collision cross section of Ar atoms with electrons (spatial average elastic collision frequency of 1.21×10^{10} Hz, higher than that of pure Ne of 9.27×10^{9} Hz). Thus, the reduced Hall parameter under a high seed fraction (5.0%) and the lower electrical conductivity of pure Ar are the factors that cause the deterioration of the enthalpy extraction ratio compared with that under a low seed fraction, which is also strongly related to the nonuniform plasma structure in the generator, as will be discussed later.

Fig. 4.16 shows the electron temperature distribution and current streamline for Ne/Xe, pure Ne, and pure Ar under optimum conditions. For pure Ne, a nonuniform spiral plasma structure rotating clockwise occurs. For low seed fractions (0.1–1.0%), the plasma structure is more uniform; the electron temperature is almost uniformly distributed, the Hall (radial) current j_r is positive in almost the entirety of the generator channel, and the streamline spacing becomes almost uniform. For a high seed fraction (5.0%), the nonuniform spiral plasma structure rotating clockwise occurs. In the spiral structure region, the electron temperature is extremely high, and the Hall parameter and Hall electromotive force become small, which leads the Hall current to flow backward upstream locally ($j_r < 0$). For pure Ar, the electron temperature is extremely elevated locally along the θ-direction, forming a ring-shaped nonuniform plasma structure with twist. In this nonuniform structure, the Hall current changes from positive in the low electron temperature region to negative in the high electron temperature region, forming a local eddy current that does not contribute to the output current. Thus, these kinds of nonuniform plasma structures, particularly those that cause negative Hall current locally in the generator channel, are also the primary factors that degrade generator performance, in addition to what is displayed in Fig. 4.15 above. It should be noted here that changing the cell number does not result in much of a difference in generator performance or plasma structure. At a seed fraction of 0.1%, an inlet electron temperature of 9200 K and a load resistance of 3.0 Ω, the enthalpy extraction ratios for mesh 50 (r-direction)×180 (θ-direction), mesh 50×360 (in this study), and mesh 100×720 are 35.2±0.51%, 35.1±0.47%, and 33.8±0.36%, respectively. The global discretization error [57]–[59] for the gas density as a function of characteristic cell size at the same conditions above is shown in Fig. 4.17. The error is decreased as the grid is refined. The apparent order of convergence is found to be 1.98 which is close to the formal order of convergence of spatial discretization scheme used in the present study. These results indicate that the numerical solutions are in the asymptotic grid-convergence range.

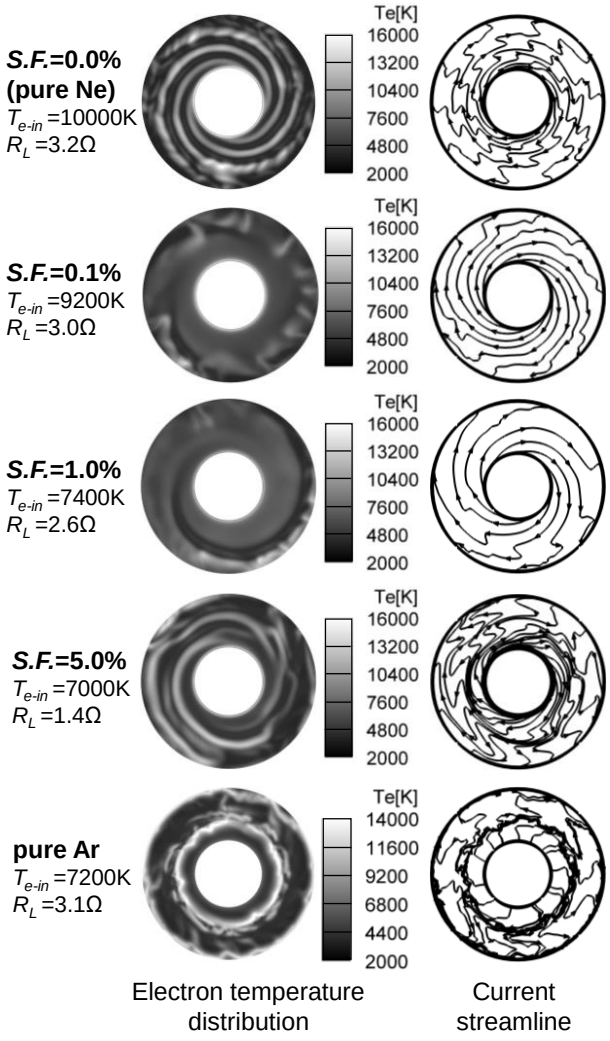

Fig. 4.16 The electron temperature distribution and current streamline for Ne/Xe, pure Ne and pure Ar under optimum conditions.

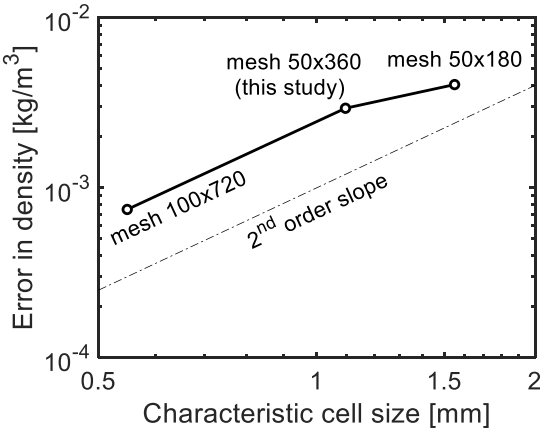

Fig. 4.17 Global discretization error for the gas density as a function of characteristic cell size.

4.4.3 Comparison of numerical and experimental results

As shown in Fig. 4.14, in low inlet electron temperature (low pre-ionization power ratio) region, the enthalpy extraction ratio for a seed fraction of 0.1% is around 1.0–5.0% ($T_{e\text{-}in}$ = 5900 – 6450 K, $\alpha_{in} = 0.25\times10^{-4} – 0.72\times10^{-4}$), for a seed fraction of 1.0% it is 1.0–8.0% ($T_{e\text{-}in}$ = 5400 – 6280 K, $\alpha_{in} = 0.25\times10^{-4} – 1.7\times10^{-4}$), for a seed fraction of 5.0% it is 2.0–6.0% ($T_{e\text{-}in}$ = 5400 – 5950 K, $\alpha_{in} = 0.55\times10^{-4} – 1.97\times10^{-4}$), and for pure Ar it is 3.0–6.0% ($T_{e\text{-}in}$ = 6000 – 6700 K, $\alpha_{in} = 0.36\times10^{-4} – 1.92\times10^{-4}$). These results are close to those obtained by the experiments shown in Fig. 4.13, had an enthalpy extraction ratio around 0.5–2.0% for a seed fraction of 0.1%, and 3.0–5.0% for seed fractions of 1.0% and 5.0% and for pure Ar.

Next, the power generation characteristics obtained from numerical simulations at the low inlet electron temperature region are compared with the results obtained in the experiments. Fig. 4.18 shows the output voltage-current characteristics in the experiment (closed dot) and the simulations (open dot) for Ne/Xe at different seed fractions and for pure Ar. The dash-dotted lines indicate the optimum load resistances in the numerical simulations and experiments. It can be seen that adjusting the inlet electron temperature in the numerical simulations allows us to obtain the numerical results that are similar to those obtained in the experiments. Fig. 4.19 shows the comparison of plasma structure at the closed dot of Fig. 4.18, where the video image observed in the experiment and the electron temperature distribution obtained in the numerical simulation are presented. The load resistance in the numerical simulation is set the same to that in the experiment. The white region in the video image from the experiment is the area in which plasma emission is strong, and the electron temperature is thought to be high (although both do not always have a linear relationship). The nonuniform distribution of the white bright color region in the generator indicates that the electron temperature is not uniformly distributed, saying in other word, the plasma is nonuniform. The plasma structures in a disk MHD generator can be categorized roughly into three types, as shown in Figs. 4.16 and 4.19. The first one is an almost uniform structure for Ne/Xe at seed fractions of 0.1% and 1.0% (Fig. 4.16), the second is the nonuniform plasma with a specific structure that can be in a spiral-shape or ring-shape for pure Ne, Ne/Xe at a seed fraction of 5.0% and pure Ar (Fig. 4.16), and the third is the nonuniform plasma with many fine and messy streak structures changing the distribution in time and space (Fig. 4.19). Based on this classification, the plasma structure obtained in the numerical simulations can be identical to the nonuniform plasma structure observed in the experiment. The nonuniform and unsteady behavior of the plasma is caused by low inlet electron temperature.

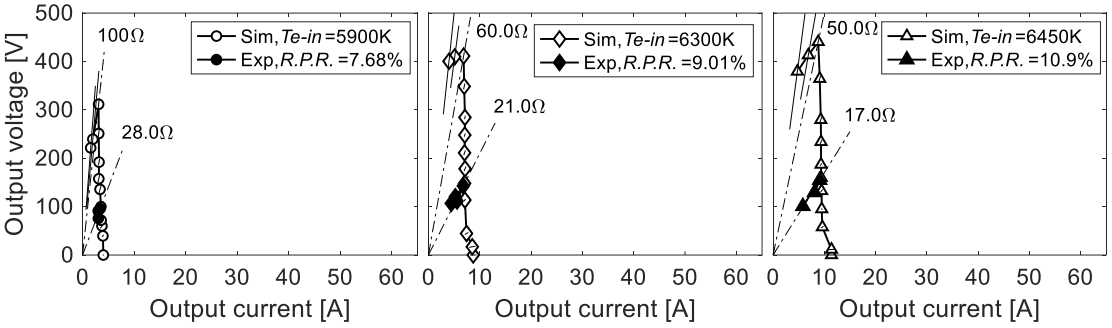

(a) Seed fraction 0.1%

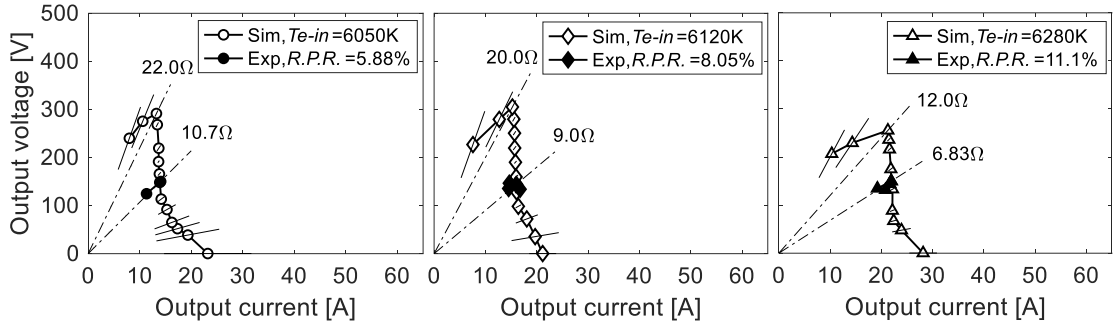

(b) Seed fraction 1.0%

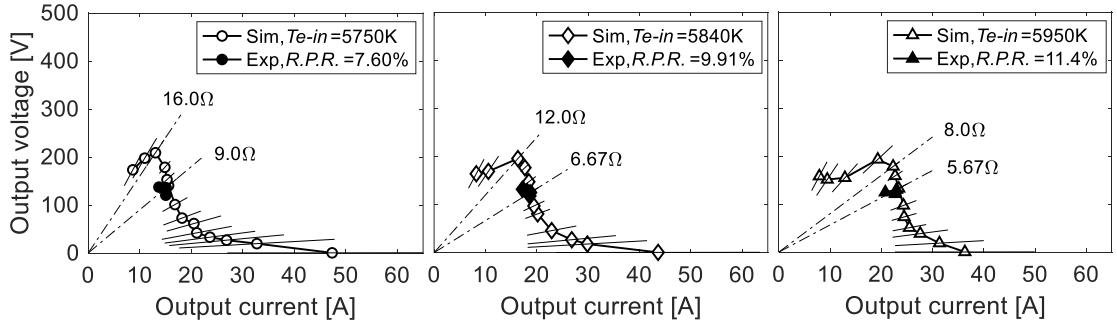

(c) Seed fraction 5.0%

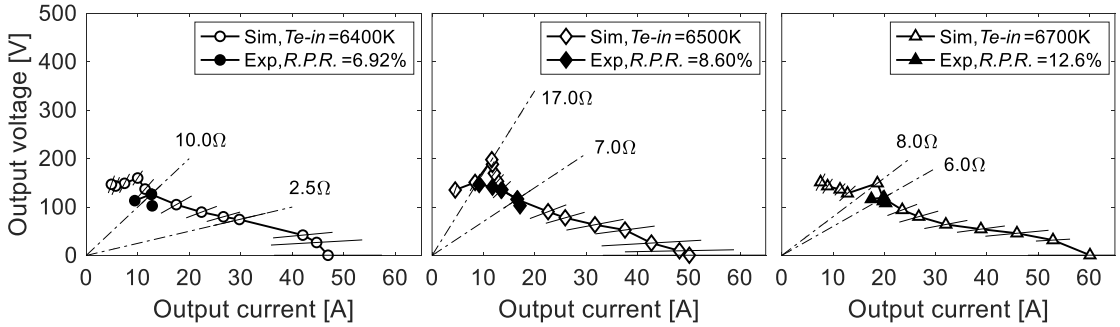

(d) pure Ar

Fig. 4.18 Comparison of output voltage-current characteristics in experiment (filled point) and simulation (unfilled point) for Ne/Xe and for pure Ar.

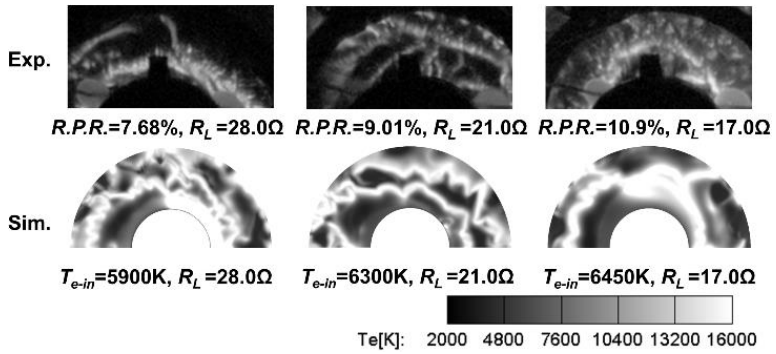

(a) Seed fraction 0.1%

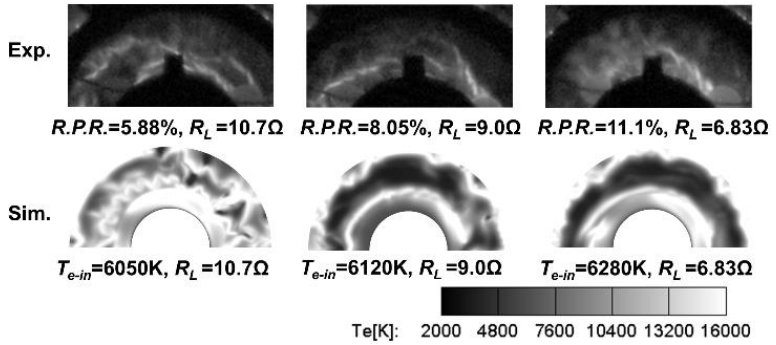

(b) Seed fraction 1.0%

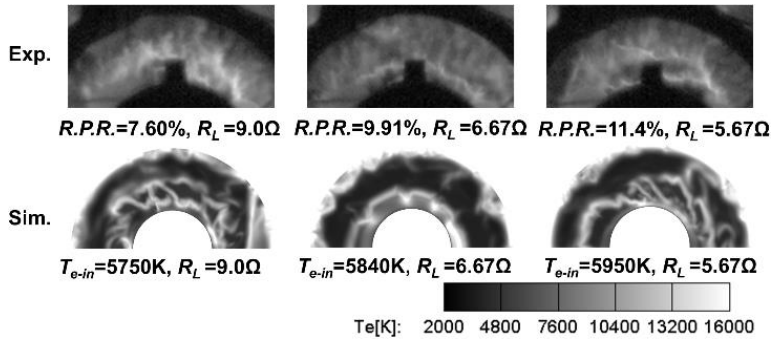

(c) Seed fraction 5.0%

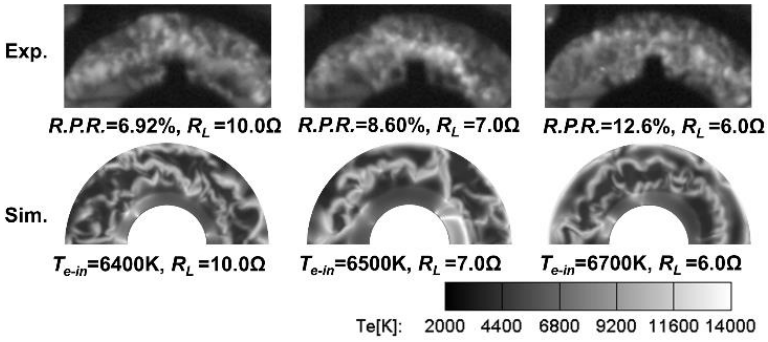

(d) Pure Ar

Fig. 4.19 Comparison of plasma structure in experiment and in numerical simulation for Ne/Xe and for pure Ar.

Table 4.6 provides the plasma production efficiencies for Ne/Xe at different seed fractions and for pure Ar. The plasma production efficiency is defined here as the ratio of the pre-ionization power *P.P.* [Eq. (4.6)] estimated in the simulations to the RF input power in the experiments. The plasma production efficiency was very low, roughly 1–2% for a seed fraction of 0.1% and 4–5% for seed fractions of 1.0% and 5.0% and for pure Ar. Although the plasma production efficiency tends to increase as the seed fraction increases, which can be beneficial due to the low ionization potential of Xe, it is still low. Therefore, the requirement of a large RF input power for the pre-ionization in the experiment is something that must be improved in future work. Thus, it is necessary to increase the plasma production efficiency. In comparison with the previous power generation experiment with pure Ar using two-turn RF induction coil for pre-ionization [18], the four-turn coil used in the present study (including the results of pure Ar in section 4.3) was found to be better, being attributed to more efficient plasma production. Although the flexibility of the coil configuration is quite limited in such a present small scale experimental generator, the turn number and/or the location of the coil are worth examining for more efficient plasma production in future work. Additionally, increasing the plasma production efficiency by optimizing the frequency of the RF power and the arrangement of the RF power transition system, or by utilizing a dielectric barrier discharge or a nano-second pulse discharge as other possible ways for efficient pre-ionization is also necessary.

The numerical simulations strongly suggest that the inlet electron temperature (inlet ionization degree) should be increased to improve the enthalpy extraction ratio. The inlet electron temperature (inlet ionization degree) needs to be higher than 8000 K ($\alpha_{in} = 5\times10^{-4}$) for a seed fraction of 0.1%, 7000 K ($\alpha_{in} = 5.7\times10^{-4}$) for 1.0% to obtain an enthalpy extraction ratio over 20%. And it needs to be higher than 6400 K ($\alpha_{in} = 4.8\times10^{-4}$) for a seed fraction of 5.0% and higher than 6900 K ($\alpha_{in} = 3\times10^{-4}$) for pure Ar to obtain an enthalpy extraction ratio over 10%. Although the enthalpy extraction ratio at seed fractions of 0.1% and 1.0% for Ne/Xe in the experiment is almost the same as that for pure Ar (Fig. 4.13), the simulations indicate that they will surpass it if a higher inlet electron temperature (inlet ionization degree) as mentioned above is achieved. Therefore, Ne/Xe with a few percent of Xe is a promising working gas for the development of high performance MHD generators in the future, and the results we have presented in this study provide basic guidelines for improving experimental generator performance.

Table 4.6 Plasma production efficiency

(a) Seed fraction 0.1%

	Experiment	Simulation
	R.P.R.=7.68%	$T_{e\text{-}in}$=5900K
P.P.(Sim) / RF input power (Exp) [%]	0.045kW / 5.19kW = 0.87	
	R.P.R.=9.01%	$T_{e\text{-}in}$=6300K
P.P.(Sim) / RF input power (Exp) [%]	0.097kW / 6.09kW = 1.59	
	R.P.R.=10.9%	$T_{e\text{-}in}$=6450K
P.P.(Sim) / RF input power (Exp) [%]	0.127kW / 7.37kW = 1.72	

b) Seed fraction 1.0%

	Experiment	Simulation
	R.P.R.=5.88%	$T_{e\text{-}in}$=6050K
P.P.(Sim) / RF input power (Exp) [%]	0.187kW / 3.91kW = 4.78	
	R.P.R.=8.05%	$T_{e\text{-}in}$=6120K
P.P.(Sim) / RF input power (Exp) [%]	0.215kW / 5.36kW = 4.01	
	R.P.R.=11.1%	$T_{e\text{-}in}$=6280K
P.P.(Sim) / RF input power (Exp) [%]	0.294kW / 7.42kW = 3.96	

c) Seed fraction 5.0%

	Experiment	Simulation
	R.P.R.=7.60%	$T_{e\text{-}in}$=5750K
P.P.(Sim) / RF input power (Exp) [%]	0.199kW / 4.54kW = 4.38	
	R.P.R.=9.91%	$T_{e\text{-}in}$=5840K
P.P.(Sim) / RF input power (Exp) [%]	0.243kW / 5.93kW = 4.10	
	RF=11.4%	$T_{e\text{-}in}$=5950K
P.P.(Sim) / RF input power (Exp) [%]	0.309kW / 6.81kW = 4.54	

(d) pure Ar

	Experiment	Simulation
	R.P.R.=6.92%	$T_{e\text{-}in}$=6400K
P.P.(Sim) / RF input power (Exp) [%]	0.157kW / 3.32kW = 4.73	
	R.P.R.=8.60%	$T_{e\text{-}in}$=6500K
P.P.(Sim) / RF input power (Exp) [%]	0.198kW / 4.13kW = 4.79	
	R.P.R.=12.6%	$T_{e\text{-}in}$=6700K
P.P.(Sim) / RF input power (Exp) [%]	0.309kW / 6.11kW = 5.06	

4.5 Summary of chapter 4

The experiments of pure Ar and Xe-seeded Ne plasma MHD electrical power generations were conducted, and the performance and plasma behavior in the experimental generator were examined using time-dependent r-θ two-dimensional numerical simulations. The generator performance and plasma behavior in both the experiments and simulations were discussed and compared in order to develop guidelines for improving the experimental generator performance.

(1) In the experiments, the enthalpy extraction ratio increased with increasing RF input power (ratio).

(2) In the experiment with pure Ar working gas using a Subsonic-Supersonic generator (a generator at which the RF induction coil is placed in the subsonic-supersonic region) with 2-mm-high throat, a maximum enthalpy extraction ratio of 4.01% was obtained at an RF input power of 5.91 kW, a load resistance of 13 Ω. In the simulation based on this experiment, at an assumed inlet electron temperature around 5600 K (inlet ionization degree 0.10×10^{-4}) – 6600 K (1.36×10^{-4}), the plasma structure is identical to the nonuniform plasma observed in the experiment. An enthalpy extraction ratio around 2–5% matches well with that in the experiment. The numerical results suggest that a higher inlet electron temperature of above 7000 K (inlet ionization degree 3.15×10^{-4}) should be realized in the experiment to achieve an enthalpy extraction ratio over 10%.

(3) In the experiment with Ne/Xe working gas using a Supersonic generator (a generator at which the RF induction coil is placed in the supersonic region) with 3-mm-high throat, the enthalpy extraction ratio of about 0.5 – 2.0% was obtained for a seed fraction of 0.1% (RF input power ratio, *R.P.R.*, of 7.68 – 10.9%) and 3.0 – 5.0% for seed fractions of 1.0% (*R.P.R.* = 5.88 – 11.1%) and 5.0% (*R.P.R.* = 7.60 – 11.4%). In the simulation based on this experiment, when an appropriate inlet electron temperature is assumed, $T_{e\text{-}in}$ = 5900–6450 K (inlet ionization degree $\alpha_{in} = 0.25\times10^{-4} - 0.72\times10^{-4}$) for a seed fraction of 0.1%, $T_{e\text{-}in}$ = 6050–6280 K ($\alpha_{in} = 1.08\times10^{-4} - 1.7\times10^{-4}$) for a seed fraction of 1.0% and $T_{e\text{-}in}$ = 5750–5950 K ($\alpha_{in} = 1.27\times10^{-4} - 1.97\times10^{-4}$) for a seed fraction of 5.0%, the plasma structure is almost identical to the nonuniform plasma structure observed in the experiment, and the resulting enthalpy extraction ratio around 1–8% was close to that obtained in the experiment.

(4) The numerical simulations suggest that achieving an inlet ionization degree above $5–6\times10^{-4}$ when using Ne/Xe at a seed fraction of 0.1–1.0% should result in an enthalpy extraction ratio above 20%. Therefore, the enthalpy extraction ratio is expected to surpass that for pure Ar.

Chapter 5 Conclusions and Future Work

5.1 Conclusions of the present study

In the present thesis, the feasibility, power generator performance, challenges, and future prospects of a Xe-seeded noble gas plasma MHD generator that utilizes a noble gas Xe as a seed material instead of alkali metal (Cs, K) were studied. The conclusions of the present study are as follows.

(1) Similar to the conventional alkali metal seeded plasma, in Xe-seeded noble gas plasma, uniform plasma can be produced and maintained, and under the same total ionization degree the same power generator performance can be obtained. However, in alkali metal seeded plasma, stable and uniform plasma is achieved when the critical Hall parameter exceeds the Hall parameter generally based on the linear perturbation theory, whereas in Xe-seeded noble gas plasma, uniform plasma is maintained when the characteristic time of electron number density is longer than the residence time of the working gas even under the electron temperature condition at which the unstable plasma is suggested from the linear perturbation theory.

(2) Adding small amounts of Xe (Xe seed fraction around 0.01–1.0%) to mother gas (noble gas) can reduce the pre-ionization power ratio while maintaining high power generator performance. Particularly, among the mother gases Ar, Ne and He, Ne/Xe provides the highest generator performance, and at seed fractions around 0.05–1.0%, the pre-ionization power ratio decreases to about 60% of that for pure Ne. Adding excessively amounts of Xe, however, deteriorates the performance. These are attributed to a relatively small atomic weight of Ne, a small collision cross section of Ne atom with electron, a low ionization potential of Xe, and a large atomic weight of Xe and a large collision cross section of Xe atom with electron.

(3) In the MHD power generation experiments with Ne/Xe plasma pre-ionized by a radio frequency (RF) electromagnetic field, the enthalpy extraction ratio increased with increasing RF input power ratio. The enthalpy extraction ratio of about 5% was obtained for seed fractions of 1.0% and 5.0%. In the numerical simulations for this experimental generator, when an appropriate inlet electron temperature (inlet ionization degree) is assumed (for instance, at Xe seed fraction of 1.0%, the inlet electron temperature is 6280 K (the corresponding inlet ionization degree is 1.70×10^{-4})), the plasma structure obtained in the

simulations is almost identical to the nonuniform plasma structure observed in the experiments, as too does the enthalpy extraction ratio. Thus, the experimental results can be reproduced by the numerical simulation. Moreover, in the experimental generator, if an inlet ionization degree of over $5–6\times10^{-4}$ is achieved, an enthalpy extraction ratio above 20% can be obtained, which is expected to surpass that for pure Ar.

In alkali metal seeded plasma, the plasma with high electrical conductivity is relatively easy to be produced and maintained; nevertheless, there are concerns about the handling of seed material when operating power generation system. For Xe-seeded noble gas plasma, on the other hand, in addition to reduction of pre-ionization power by adding Xe, the generator performance equivalent to that of alkali metal seeded plasma can be expected, and the issues when operating power generation system can be eliminated. Here, the key is to achieve the appropriate electron temperature (ionization degree) at generator inlet. In other words, if an appropriate inlet electron temperature (inlet ionization degree) can be achieved under a low pre-ionization power due to the addition of Xe, a promising power generation system that eliminates the concern issues in alkali metal seeded plasma can be constructed, that is suggested by the power generation experiment and numerical simulation in the present study.

5.2 Future work

The future challenges as an extension of the present study are presented as follows.

1. Improvement of plasma production efficiency in the experiment

As shown in chapter 4, if sufficient electron temperature or ionization degree can be provided at generator inlet, an enthalpy extraction ratio of over 20% is expected in Ne/Xe plasma MHD generator. In order to increase the inlet electron temperature (inlet ionization degree) in the experiment, it is necessary to increase the plasma production efficiency by optimizing the frequency of the RF power and the arrangement of the RF power transition system. Meanwhile, the study of a dielectric barrier discharge or a nano-second pulse discharge as other possible ways for efficient pre-ionization is also useful. In regards to this point, first the numerical analysis of plasma production using the above techniques should be carried out, and followed by the actual MHD power generation experiment using the above plasma production techniques.

2. Optimization of generator shape of Xe-seeded noble gas plasma

Optimization of MHD generator shape as a way to improve generator performance as well as to control the fluid and plasma condition inside the generator channel has been usually conducted with alkali metal seeded plasma in both a small-scale [60], [61] and a commercial-scale large-size MHD generators [62]–[65]. The numerical simulations have shown that an MHD generator with a high enthalpy extraction ratio of about 30% and an isentropic efficiency of over 80% can be achieved by optimizing the shape of the generator channels [64], [65]. Therefore, in the future it is necessary to design and optimize the MHD generator channel for Xe-seeded noble gas plasma in order to improve the generator performance. The optimal design of experimental scale generator toward improving experimental generator performance and optimal design of 1000-MW class large-scale MHD generator for commercialization are both essential.

3. Study the performance characteristics of a commercial-scale, large-size MHD generator with Xe-seeded noble gas plasma

One of other advantages of MHD power generation is that MHD generator has a quick response for output control compared with the conventional thermal power generation using a turbine generator, owing to its reduced mechanical inertia. The control range of output power by adjusting seed fraction and load voltage has been studied numerically in a commercial scale MHD generator with Cs-seeded Ar plasma [64]. For the development of a commercial-scale MHD generator operating with Xe-seeded Ne working gas, the study of the performance characteristics of Ne/Xe plasma MHD generator such as the control of output power as stated above should be carried out in the future.

References

[1] U.S. Energy Information Administration, “The International Energy Outlook 2019.”

[2] R. J. Rosa, *Magnetohydrodynamic Energy Conversion*. New York, NY, USA: McGraw-Hill, 1968, pp. 1–16, 59–113, 163–195.

[3] B. Karlovitz and D. Halasz, “Process for the conversion of energy and apparatus for carrying out the process,” US Patent 2210918, Aug. 13, 1940 Accessed: Nov. 09, 2023. [Online]. Available: https://patents.google.com/patent/US2210918A/en

[4] B. C. Lindley, “Status report on MHD electrical power generation–IAEA/ENEA International Liaison Group on MHD Electrical power generation,” *Nuclear Fusion*, vol. 7, no. 4, pp. 267–287, Dec. 1967, doi: 10.1088/0029-5515/7/4/010.

[5] E. Levi, “Power: MHD’s target: Payoff by 2000: Efficiencies over 50 percent and generating costs of 32 mills/kWh may make magnetohydrodynamic systems viable by 1995,” *IEEE Spectr*, vol. 15, no. 5, pp. 46–51, May 1978, doi: 10.1109/MSPEC.1978.6367698.

[6] M. Mitchner and C. H. Kruger, *Partially Ionized Gases*. New York, NY, USA: Wiley, 1973, pp. 54–99, 126–130, 163–241, 404–423.

[7] George W. Sutton and Arthur Sherman, *Engineering Magnetohydrodynamics*. New York: McGraw-Hill, 1968, pp. 224–225.

[8] C. R. Bedick, C. R. Woodside, R. Baylor, and M. Paul-Irudayaraj, “Combustion Plasma Electrical Conductivity Model Validation for Oxy-fuel MHD Applications: Spectroscopic and Electrostatic Probe Studies,” *Combust Flame*, vol. 213, pp. 140–155, Mar. 2020, doi: 10.1016/j.combustflame.2019.11.003.

[9] A. Brekis, A. Alemany, O. Alemany, and A. Montisci, “Space Thermoacoustic Radioisotopic Power System, SpaceTRIPS: The Magnetohydrodynamic Generator,” *Sustainability*, vol. 13, no. 23, p. 13498, Dec. 2021, doi: 10.3390/su132313498.

[10] N. Harada, L. C. Kien, and M. Hishikawa, “Basic Studies on Closed Cycle MHD Power Generation System for Space Application,” in *35th AIAA Plasmadynamics and Lasers Conference*, AIAA 2004-2365, Jun. 2004. doi: 10.2514/6.2004-2365.

[11] V. S. Slavin, G. C. Bakos, T. A. Milovidova, and K. A. Finnikov, “Space Power Installation Based on Solar Radiation Collector and MHD Generator,” *IEEE Transactions on Energy Conversion*, vol. 21, no. 2, pp. 491–503, Jun. 2006, doi: 10.1109/TEC.2005.860401.

[12] T. Murakami, Y. Okuno, and H. Yamasaki, “Achievement of the Highest Performance of a CCMHD Generator: An Isentropic Efficiency of 63% and an Enthalpy Extraction Ratio

of 31%," *IEEE Transactions on Plasma Science*, vol. 32, no. 5, pp. 1886–1892, Oct. 2004, doi: 10.1109/TPS.2004.835484.

[13] Y. Okuno, K. Yoshikawa, T. Okamura, H. Yamasaki, S. Kabashima, and S. Shioda, "Proposal of a Highly Efficient CCMHD Single Power Generation System," *IEEJ Transactions on Power and Energy*, vol. 118, no. 12, pp. 1457–1462, 1998, doi: 10.1541/ieejpes1990.118.12_1457.

[14] M. Tanaka, Y. Aoki, L. Zhao, and Y. Okuno, "Experiments on High-Temperature Xenon Plasma Magnetohydrodynamic Power Generation," *IEEE Transactions on Plasma Science*, vol. 44, no. 7, pp. 1241–1246, Jul. 2016, doi: 10.1109/TPS.2016.2565600.

[15] T. Murakami and Y. Okuno, "Simulation and demonstration of magnetohydrodynamic energy conversion in a high-temperature inert gas," *Phys Plasmas*, vol. 16, no. 3, Mar. 2009, doi: 10.1063/1.3083295.

[16] M. Tanaka, T. Murakami, and Y. Okuno, "Plasma Characteristics and Performance of Magnetohydrodynamic Generator With High-Temperature Inert Gas Plasma," *IEEE Transactions on Plasma Science*, vol. 42, no. 12, pp. 4020–4025, Dec. 2014, doi: 10.1109/TPS.2014.2365591.

[17] H. Kobayashi and Y. Okuno, "Feasibility Study on Frozen Inert Gas Plasma MHD Generator," *IEEE Transactions on Plasma Science*, vol. 28, no. 4, pp. 1296–1302, 2000, doi: 10.1109/27.893319.

[18] T. Nakane, K. Uehigashi, T. Iwamoto, and Y. Okuno, "Fundamental Experiments of Radio-Frequency Pre-ionized Inert Gas Plasma MHD Electrical Power Generation," *Electrical Engineering in Japan*, vol. 207, no. 4, pp. 18–24, Jun. 2019, doi: 10.1002/eej.23214.

[19] H. Kobayashi, Y. Satou, and Y. Okuno, "Numerical performance simulation of frozen helium plasma disk MHD generator," *Electrical Engineering in Japan*, vol. 140, no. 3, pp. 26–33, Aug. 2002, doi: 10.1002/eej.10030.

[20] Nob. Harada, N. Sakamoto, and H. Endo, "Closed Cycle MHD System using He/Xe Working Gas," in *28th Plasmadynamics and Lasers Conference*, AIAA 97-2372, Jun. 1997. doi: 10.2514/6.1997-2372.

[21] H. Kobayashi, Y. Okuno, and S. Kabashima, "Three-dimensional structures of MHD flow in a disk generator," *IEEE Transactions on Plasma Science*, vol. 26, no. 5, pp. 1526–1531, 1998, doi: 10.1109/27.736055.

[22] K. Shimizu, H. Kobayashi, Y. Okuno, and S. Kabashima, "Three-dimensional Structures of Plasma and Fluid Flow in a Nonequilibrium Disk MHD Generator with 100MWth," *IEEJ Transactions on Power and Energy*, vol. 119, no. 1, pp. 103–108, 1999, doi: 10.1541/ieejpes1990.119.1_103.

[23] H. Suzuki and Y. Okuno, "Numerical Study of Plasma Structure and Output Power in a Pre-ionized Inert Gas Plasma MHD Generator," *IEEJ Transactions on Power and Energy*, vol. 140, no. 9, pp. 694–699, Sep. 2020, doi: 10.1541/ieejpes.140.694.

[24] E. Hinnov and J. G. Hirschberg, "Electron-Ion Recombination in Dense Plasmas," *Physical Review*, vol. 125, no. 3, pp. 795–801, Feb. 1962, doi: 10.1103/PhysRev.125.795.

[25] N. A. Generalov, V. P. Zimakov, and G. I. Kozlov, "A method for infrared diagnostics of a plasma and its use for the investigation of ionization and recombination of xenon behind the front of a shock wave," *Soviet Physics Jept*, vol. 125, no. 3, pp. 1038–1043, Feb. 1970.

[26] T. G. Owano, C. H. Kruger, and R. A. Beddini, "Electron-ion three-body recombination coefficient of argon," *AIAA Journal*, vol. 31, no. 1, pp. 75–82, Jan. 1993, doi: 10.2514/3.11321.

[27] T. J. Mcintyre, A. F. P. Houwing, R. J. Sandeman, and H. A. Bachor, "Relaxation behind shock waves in ionizing neon," *J Fluid Mech*, vol. 227, pp. 617–640, Jun. 1991, doi: 10.1017/S0022112091000277.

[28] L. M. Biberman, V. S. Vorob'ev, and I. T. Yakubov, "On the theory of Ionization and Recombination in a Low-Temperature Plasma," *Soviet Physics Jetp*, vol. 29, no. 6, pp. 1070–1074, Dec. 1969.

[29] L. Levin, S. Moody, E. Klosterman, R. Center, and J. Ewing, "Kinetic Model for Long-Pulse XeCl Laser Performance," *IEEE J Quantum Electron*, vol. 17, no. 12, pp. 2282–2289, Dec. 1981, doi: 10.1109/JQE.1981.1070708.

[30] N. B. Kolokolov, A. A. Kudrjavtsev, and A. B. Blagoev, "Interaction processes with creation of fast electrons in the low temperature plasma," *Phys Scr*, vol. 50, no. 4, pp. 371–402, Oct. 1994, doi: 10.1088/0031-8949/50/4/010.

[31] S. J. Buckman, J. W. Cooper, M. T. Elford, M. Inokuti, Y. Itikawa, and H. Tawara, *Landolt-Bornstein: Numerical Data and Functional Relationships in Science and Technology*, vol. I/17A, chap. 2.5. Berlin: Springer, 2000, p. 2.35–2.55.

[32] H. C. Yee, "Upwind and Symmetric Shock-Capturing Scheme," NASA, Technical Memorandum 89464, May 1987.

[33] S. Fujino, M. Fujiwara, and M. Yoshida, "BiCGSafe method based on minimization of associate residual," *Transactions of Japan Society for Computational Engineering and Science*, vol. 8, pp. 145–152, Oct. 2005, doi: 10.11421/jsces.2005.20050028.

[34] T. Sekimoto and S. Fujino, "A Proposal of Variants of BiCGSafe Method for Solving Linear Systems in Realistic Problems," in *Proceedings of The World Congress on Engineering 2012*, 2012, pp. 261–264.

[35] T. Nakamura and W. Riedmuller, "Stability of Nonequilibrium MHD Plasma in the Regime of Fully Ionized Seed," *AIAA Journal*, vol. 12, no. 5, pp. 661–668, May 1974, doi: 10.2514/3.49316.

[36] H. Kobayashi, Y. Okuno, and S. Kabashima, "Three-Dimensional Structures of MHD Flow in a Disk Generator," *IEEE Transactions on Plasma Science*, vol. 26, no. 5, pp. 1526–1531, 1998, doi: 10.1109/27.736055.

[37] A. O. Rankine, "On the variation with temperature of the viscosities of the gases of the argon group," *Proceedings of the Royal Society of London. Series A, Containing Papers of a Mathematical and Physical Character*, vol. 84, no. 569, pp. 181–192, Jul. 1910, doi: 10.1098/rspa.1910.0069.

[38] S. Chapman and T. G. Cowling, *The Mathematical Theory of Non-uniform Gases: An Account of The Kinetic Theory of Viscosity, Thermal Conduction and Diffusion in Gases*, 3rd edition. London: Cambridge University Press, 1970, pp. 226–246.

[39] J. Kestin, S. T. Ro, and W. A. Wakeham, "Viscosity of the Noble Gases in the Temperature Range 25–700°C," *J Chem Phys*, vol. 56, no. 8, pp. 4119–4124, Apr. 1972, doi: 10.1063/1.1677824.

[40] B. BALDWIN and H. LOMAX, "Thin-layer approximation and algebraic model for separated turbulentflows," in *16th Aerospace Sciences Meeting*, AIAA-78-257, Jan. 1978. doi: 10.2514/6.1978-257.

[41] M. Visbal and D. Knight, "The Baldwin-Lomax Turbulence Model for Two-Dimensional Shock-Wave/Boundary-Layer Interactions," *AIAA Journal*, vol. 22, no. 7, pp. 921–928, Jul. 1984, doi: 10.2514/3.48528.

[42] A. H. Shapiro, *The Dynamics and Thermodynamics of Compressible Fluid Flow*, vol. 2. New York: John Wiley and Sons, 1953, pp. 1107–1125.

[43] T. Kouchi, T. Mitani, T. Hiraiwa, S. Tomioka, and G. Masuya, "Evaluation of Thrust Performance in Scramjet Engines with Measured Internal Drag," *Journal of the Japan Society for Aeronautical and Space Science*, vol. 51, no. 595, pp. 403–411, 2003, doi: 10.2322/jjsass.51.403.

[44] J. Bons, "A Critical Assessment of Reynolds Analogy for Turbine Flows," *ASME Journal of Heat Transfer*, vol. 127, no. 5, pp. 472–485, May 2005, doi: 10.1115/1.1861919.

[45] R. B. Bird, W. E. Stewart, and E. N. Lightfoot, "Appendix B: The Fluxes and the Equations of Change," in *Transport Phenomena*, Revised Second Edi., New York: John Wiley and Sons, 2006, pp. 843–851.

[46] N. A. Generalov, V. P. Zimakov, and G. I. Kozlov, "A method for infrared diagnostics of a plasma and its use for the investigation of ionization and recombination of xenon behind the front of a shock wave," *Soviet Physics Jept*, vol. 125, no. 3, pp. 1038–1043, Feb. 1970.

[47] M. Baeva, A. Bösel, J. Ehlbeck, and D. Loffhagen, "Modeling of microwave-induced plasma in argon at atmospheric pressure," *Phys Rev E*, vol. 85, no. 5, p. 056404, May 2012, doi: 10.1103/PhysRevE.85.056404.

[48] Heui Seob Jeong, Buhm-Jae Shin, and Ki-Woong Whang, "Two-dimensional Multifluid Modeling of the He-Xe Discharge in an AC Plasma Display Panel," *IEEE Transactions on Plasma Science*, vol. 27, no. 1, pp. 171–181, Feb. 1999, doi: 10.1109/27.763110.

[49] C. H. Kruger, M. Mitchner, and U. Daybelge, "Transport properties of MHD-generator plasmas," *Proceedings of the IEEE*, vol. 56, no. 9, pp. 1458–1471, Sep. 1968, doi: 10.1109/PROC.1968.6633.

[50] R. J. Rosa, C. H. Krueger, and S. Shioda, "Plasmas in MHD power generation," *IEEE Transactions on Plasma Science*, vol. 19, no. 6, pp. 1180–1190, Dec. 1991, doi: 10.1109/27.125040.

[51] T. Takahashi, T. Fujino, and M. Ishikawa, "Performance analysis of experimental-scale scramjet engine driven DCW-MHD generator," *IEEJ Transactions on Electrical and Electronic Engineering*, vol. 8, no. 5, pp. 440–445, Sep. 2013, doi: 10.1002/tee.21878.

[52] H. Kobayashi, Y. Okuno, and S. Kabashima, "Three-dimensional simulation of nonequilibrium seeded plasma in closed cycle disk MHD generator," *IEEE Transactions on Plasma Science*, vol. 25, no. 2, pp. 380–385, Apr. 1997, doi: 10.1109/27.602515.

[53] A. G. Gaydon and I. R. Hurle, *The shock tube in high-temperature chemical physics*. New York: Reinhold Pub. Corp., 1963, pp. 23–28.

[54] K. Akai, M. Hori, N. Ando, and T. Shimogami, "Shock Tube Study on Stress Wave Propagation in Confined Soils," *Proceedings of the Japan Society of Civil Engineers*, vol. 1972, no. 200, pp. 127–141, 1972, doi: 10.2208/jscej1969.1972.200_127.

[55] T. Murakami and Y. Okuno, "High-density energy conversion using compact magnetohydrodynamic electrical power generator," *Appl Phys Lett*, vol. 91, no. 16, Oct. 2007, doi: 10.1063/1.2800785.

[56] T. Murakami and Y. Okuno, "Experiments and numerical simulations on high-density magnetohydrodynamic electrical power generation," *J Appl Phys*, vol. 104, no. 6, Sep. 2008, doi: 10.1063/1.2978190.

[57] A. Bonfiglioli and R. Paciorri, "Convergence Analysis of Shock-Capturing and Shock-Fitting Solutions on Unstructured Grids," *AIAA Journal*, vol. 52, no. 7, pp. 1404–1416, Jul. 2014, doi: 10.2514/1.J052567.

[58] C. J. Roy, "Review of Discretization Error Estimators in Scientific Computing," in *48th AIAA Aerospace Sciences Meeting Including the New Horizons Forum and Aerospace Exposition*, Reston, Virigina: American Institute of Aeronautics and Astronautics, Jan. 2010. doi: 10.2514/6.2010-126.

[59] Ismail B. Celik, Urmila Ghia, Patrick J. Roache, Christopher J. Freitas, Hugh Coleman, and Peter E. Raad, "Procedure for Estimation and Reporting of Uncertainty Due to Discretization in CFD Applications," *J Fluids Eng*, vol. 130, no. 7, p. 078001, 2008, doi: 10.1115/1.2960953.

[60] A. Liberati and Y. Okuno, "Numerical simulation of plasma–fluid flow and performance in a disc MHD generator with contoured walls," *J Phys D Appl Phys*, vol. 43, no. 2, p. 025203, Jan. 2010, doi: 10.1088/0022-3727/43/2/025203.

[61] T. Murakami and Y. Okuno, "Magnetohydrodynamic electrical power generation using convexly divergent channel: II. Numerical simulation," *J Phys D Appl Phys*, vol. 44, no. 18, p. 185202, May 2011, doi: 10.1088/0022-3727/44/18/185202.

[62] R. Mizukoshi, Y. Matsumoto, T. Fujino, and M. Ishikawa, "Design and Performance Analysis of Large Scale Nonequilibrium Disk MHD Generator," in *38th Plasmadynamics and Lasers Conference*, Reston, Virigina: American Institute of Aeronautics and Astronautics, Jun. 2007. doi: 10.2514/6.2007-4241.

[63] T. Fujino, S. Kominami, M. Ishikawa, and Y. Okuno, "Two-dimensional numerical simulation of commercial scale nonequilibrium MHD power generator coupled with radio-frequency electromagnetic field," *IEEJ Transactions on Electrical and Electronic Engineering*, vol. 3, no. 6, pp. 696–702, Nov. 2008, doi: 10.1002/tee.20332.

[64] T. Fujino, R. Nakayasu, R. Sasaki, and Y. Okuno, "Effect of Magnetic Flux Density on Control Range of Output Power of a Commercial-Scale, Nonequilibrium MHD Generator," *IEEJ Transactions on Power and Energy*, vol. 143, no. 12, pp. 652–658, Dec. 2023, doi: 10.1541/ieejpes.143.652.

[65] D. Ichinokiyama, H. Saito, and T. Fujino, "Numerical studies of high performance of commercial scale non-equilibrium disk MHD generator working with Ar/Cs or He/Cs gas," in *Proc. 20th Int. Conf. Electr. Eng.*, Jun. 2014, pp. 1304–1312.

List of Tables

List of Figures

Acknowledgements

First of all, I would like to thank Prof. Yoshihiro Okuno, Prof. Tetsuji Okamura, Prof. Shuichiro Hirai, Prof. Tetsuya Suekane, and Assoc. prof. Takashi Sasabe for helping to review this dissertation regardless of his busy schedule.

Particularly, I would like to express my sincere gratitude to my supervisor Prof. Yoshihiro Okuno for his extraordinary support, continuous advice, invaluable guidance and teaching not only during the course of this dissertation, but since my Master's course. His contributions towards my research are gratefully acknowledged, and all the words cannot describe my sincere gratitude to him.

I would like to thank my juniors in laboratory especially Mr. Masuda, Mr. Sogame, Mr. Tanabe, Mr. Sasada, Mr. Suzuki, and Mr. Fukuhara. They have always been supporting me during my research. I am so grateful for the help and friendship of them.

I would like to thank the Tokio Marine Kagami Memorial Foundation (東京海上各務記念財団) for the scholarship support. This scholarship not only allows me to have enough time for focusing on my research, but also provides me opportunities to join activities relating to culture and sport.

Finally, and most importantly, I would like to thank my parents for their dedication and unlimited love and support. Without them none of this would have been possible. I would like to dedicate this dissertation to my mother who passed away while I was studying Master's degree in Japan. May her soul rest in peace.

December 2023

Tokyo, Japan

Ork Kimsor

List of Publications

Journal Articles (with peer review)

1. **Kimsor Ork** and Yoshihiro Okuno, “Effect of Xenon Seed on Performance of Pre-Ionized Inert Gas Plasma MHD Power Generator,” *IEEJ Transactions on Power and Energy*, Vol.142, No.2, pp.150–156, Feb. 2022. (In Japanese)
   DOI: 10.1541/ieejpes.142.150
   Ork Kimsor・奥野喜裕：「予備電離希ガスプラズマ MHD 発電機性能に与えるキセノンシードの効果」，電気学会論文誌 B，Vol. 142, No. 2, pp. 150–156, 2022.

2. **Kimsor Ork**, Yoshihiro Okuno, “Numerical Study of Plasma Behavior and Power Generation Characteristics in a Disk MHD Generator With Xenon-Seeded Neon Gas,” *IEEE Transactions on Plasma Science*, Vol. 51, No. 6, pp. 1518–1526, June 2023.
   DOI: 10.1109/TPS.2023.3271952

3. **Kimsor Ork**, Yoshinobu Kodera, and Yoshihiro Okuno, “Fundamental Experiment and Numerical Simulation of Pre-ionized Inert Gas Plasma MHD Electrical Power Generation,” *IEEJ Transactions on Power and Energy*, Vol.143, No.8, pp. 513–519, August 2023. (In Japanese)
   DOI: 10.1541/ieejpes.143.513
   Ork Kimsor，小寺義伸，奥野喜裕：「予備電離希ガスプラズマ MHD 発電の実証基礎実験と数値シミュレーションによる検討」，電気学会論文誌 B，Vol. 143，No. 8，pp. 513–519，2023.

4. **Kimsor Ork**, Yoshihiro Okuno, “Numerical Study of Plasma Behavior in a Disk-Shaped Noble Gas MHD Generator,” *IEEJ transactions on Fundamentals and Materials*, Vol. 144, No. 3, 2024 (in Japanese), (accepted for publication)
   Ork Kimsor・奥野喜裕：「ディスク形希ガス MHD 発電機におけるプラズマ挙動に関する数値的検討」，電気学会論文誌 A, Vol. 144, No. 3, 2024（掲載決定）
5. **Kimsor Ork**, Ryu Masuda, Yoshihiro Okuno, “Fundamental Experiment and Numerical Simulation of Ne/Xe Plasma Magnetohydrodynamic Electrical Power Generation,” *Journal of Propulsion and Power*, (accepted for publication on January 2024).

*. **Kimsor Ork** and Yoshihiro Okuno, "Numerical Study on Performance of a Xenon-Seeded Neon Plasma Magnetohydrodynamic Electrical Power Generator," *IEEE Transactions on Plasma Science*, (Submitted on November 2023)

International Conferences

<Oral presentation>

1. **Kimsor Ork,** Yoshihiro Okuno, "Numerical Study of Pre-ionized Inert Gas Plasma MHD Power Generator under Various Working Gases," 17th International Conference on Flow Dynamics, OS5: Advanced Applications of Multifunctional Fluids, OS5-5, pp. 212-213, 2020.
2. **Kimsor Ork,** Yoshihiro Okuno, "Plasma Structure in Pre-ionized Inert Gas Plasma MHD Power Generator under Various Working Gases," Proceedings of The International Council on Electrical Engineering Conference 2021, pp. 268-273, China, July 2021.
3. **Kimsor Ork,** Yoshihiro Okuno, "Pre-ionized Inert Gas Plasma MHD Power Generation with Ne/Xe Working Gas," 18th International Conference on Flow Dynamics, OS5: Advanced Applications of Multifunctional Fluids, OS5-5, pp. 259-260, 2021.
4. **Kimsor Ork,** Yoshihiro Okuno, "Numerical Study of Plasma Behavior and Power Generation Characteristics in an MHD Generator with Ne/Xe Working Gas," Proceedings of The International Council on Electrical Engineering Conference 2022, pp. 650-655, Seoul, Korea, July 2022.
5. T. Sogame, R. Gono, **Kimsor Ork**, and Y. Okuno, "Generation Characteristics in a Pulsed-Laser-Driven MHD Electrical Energy Converter," Proceedings of The International Council on Electrical Engineering Conference 2022, 3-0545, Seoul, Korea, July 2022.
6. R. Masuda, Y. Kodera, **Kimsor Ork**, K. Itokawa, and Y. Okuno, "Experiments of MHD Electrical Power Generation with Xenon seeded Neon Working Gas," Proceedings of The International Council on Electrical Engineering Conference 2022, pp. 656-661, Seoul, Korea, July 2022.
7. **Kimsor Ork**, Y. Okuno, "Plasma Behavior and Power Generation Characteristics in an Experimental Argon Plasma MHD Generator," 19th International Conference on Flow Dynamics, OS5: Advanced Applications of Multifunctional Fluids, OS5-9, pp. 307-312, Sendai, Japan 2022.

<Poster presentation>

1. Tin Ming Samuel Leung, **Kimsor Ork**, and Y. Okuno, "Numerical Study of Plasma Behavior in a Disk MHD Generator with Various Noble Gases," 19th International Conference on Flow Dynamics, OS21: The 18th International Students/Young Birds Seminar on Multi-scale Flow Dynamics, OS21-18, pp. 874-879, Sendai, Japan 2022.

Domestic Conferences

1. **Ork Kimsor**，鈴木甫，奥野喜裕 :「予備電離希ガスプラズマ MHD 発電における作動気体依存性」，令和 2 年電気学会全国大会，7-005，2020.
2. **Ork Kimsor**，奥野喜裕 :「予備電離希ガスプラズマ MHD 発電機性能の作動気体依存性」，電気学会　新エネルギー・環境研究会，FTE-20-010，2020.
3. **Ork Kimsor**，奥野喜裕 :「予備電離希ガスプラズマ MHD 発電機におけるプラズマ構造の作動気体依存性」，令和 3 年電気学会全国大会，7-004，2021.
4. 香取翼，**Ork Kimsor**，奥野喜裕 :「実験規模ディスク形アルゴンプラズマ MHD 発電機特性の数値計算」，電気学会　新エネルギー・環境研究会，FTE-21-033，2021.
5. **Ork Kimsor**，奥野喜裕 :「キセノンをシードした希ガスプラズマ MHD 発電機性能の数値解析」，電気学会　新エネルギー・環境研究会，FTE-21-032，2021.
6. 糸川海斗，**Ork Kimsor**，小寺義伸，増田龍，奥野喜裕 :「Ne/Xe を作動気体とする予備電離希ガスプラズマ MHD 発電実験」，電気学会　新エネルギー・環境研究会，FTE-21-031，2021.
7. **Ork Kimsor**，奥野喜裕 :「Ne/Xe プラズマ MHD 発電機内のプラズマ挙動に関する数値解析」，令和 4 年電気学会全国大会，7-006，2022.
8. 増田龍，糸川海斗，小寺義伸，**Ork Kimsor**，奥野喜裕 :「Xe をシードした希ガスプラズマ MHD 発電の実験的検討」，令和 4 年電気学会全国大会，7-004，2022.
9. **Ork Kimsor**，奥野喜裕 :「希ガスプラズマ MHD 発電実験機におけるプラズマ挙動および発電特性に関する数値シミュレーション」，電気学会　新エネルギー・環境研究会，FTE-22-023，2022.
10. 村上勝也，**Ork Kimsor**，奥野喜裕 :「アルゴンプラズマ MHD 発電機におけるプラズマ構造及び発電性能の数値的検討」，電気学会　新エネルギー・環境研究会，FTE-22-025，2022.
11. 岡田瑛，**Ork Kimsor**，高奈秀匡，奥野喜裕 :「MHD 発電機における予備電離に向けた誘電体バリア放電の数値シミュレーション」，電気学会　新エネルギー・環境研究会，FTE-22-026，2022.

12. **Ork Kimsor**，奥野喜裕 :「Ne/Xe プラズマ MHD 発電実験機の発電特性に関する数値解析」，令和 5 年電気学会全国大会，7-004，2023.
13. **Ork Kimsor**，奥野喜裕 :「希ガス MHD 発電機におけるプラズマ挙動に関する数値的検討」，電気学会　新エネルギー・環境研究会，FTE-23-032，2023.
14. 田邉大登，**Ork Kimsor**，奥野喜裕 :「アルゴンプラズマ MHD 発電実験機の発電特性における入口全圧依存性」，電気学会　新エネルギー・環境研究会，FTE-23-034，2023.

Award

2022 年 9 月　電気学会 新エネルギー・環境研究会 若手優良発表賞（国内研究会 9.）
Translated to……Technical Meeting on Frontier Technology and Engineering, IEE Japan, September 2022: The best presentation award for young researchers (Domestic conference No. 9)